Geosci. Model Dev., 18, 6553–6596, 2025
https://doi.org/10.5194/gmd-18-6553-2025

Geoscientific Model Development
Open Access
EGU

A high-resolution physical-biogeochemical model for marine resource applications in the Northern Indian Ocean (MOM6-COBALT-IND12 v1.0)

Enhui Liao[1], Laure Resplandy[2], Fan Yang[2], Yangyang Zhao[2], Sam Ditkovsky[3], Manon Malsang[4], Jenna Pearson[5], Andrew C. Ross[6], Robert Hallberg[6], and Charles Stock[6]

[1]School of Oceanography, Shanghai Jiao Tong University, Shanghai, China
[2]Department of Geosciences and High Meadows Environmental Institute, Princeton University, Princeton, NJ, USA
[3]Program in Atmospheric and Oceanic Sciences, Sayre Hall, Princeton University, Princeton, NJ, USA
[4]Laboratoire d'Océanographie et du Climat Expérimentations et Approches Numériques (LOCEAN), Institut Pierre-Simon Laplace (IPSL), Sorbonne Université, Paris, France
[5]Climatematch Academy, Neuromatch Inc., Beaverton, OR, USA
[6]NOAA OAR Geophysical Fluid Dynamics Laboratory, Princeton, NJ, USA

Correspondence: Enhui Liao (ehliao@sjtu.edu.cn) and Laure Resplandy (laurer@princeton.edu)

Received: 21 November 2024 – Discussion started: 3 January 2025
Revised: 13 August 2025 – Accepted: 21 August 2025 – Published: 29 September 2025

Abstract. We introduce and evaluate the regional ocean model MOM6-COBALT-IND12 version 1 coupling the MOM6 ocean dynamics model to the Carbon, Ocean Biogeochemistry and Lower Trophics (COBALT) biogeochemical model at a horizontal resolution of 1/12°. The model covers the northern Indian Ocean (from 8.6° S to the northern continental boundaries), central to the livelihoods and economies of countries that comprise about one-third of the world's population. We demonstrate that the model effectively captures the key physical and biogeochemical basin-scale features related to seasonal monsoon reversal, interannual Indian Ocean Dipole and multi-decadal variability, as well as intraseasonal and fine-scale variability (e.g., eddies and planetary waves), which are all essential for accurately simulating patterns of coastal upwelling, primary productivity, temperature, salinity, and oxygen levels. Well represented features include the timing and amplitude of the monsoonal blooms triggered by summer coastal upwelling and winter mixing, the strong contrast between the high evaporation/high salinity Arabian Sea and high precipitation/high runoff/low salinity Bay of Bengal, the seasonality of the Great Whirl gyre and coastal Kelvin upwelling/downwelling waves, as well as the physical and biogeochemical patterns associated with intraseasonal and interannual variability. Quantitatively, the model exhibits relatively small biases, as reflected by root mean square error (RMSE) values in key variables: sea surface temperature (0.25–0.3 °C), mixed layer depth (7–8.09 m), sea level anomaly (0.02 m), sea surface salinity (0.53–0.71 psu), vertical chlorophyll (0.03–0.3 mg m^{-3}), subsurface temperature (0.33 °C), and subsurface salinity (0.07 psu). A major model bias (16 µmol kg^{-1} of oxygen) is the larger oxygen minimum zone simulated in the Bay of Bengal, a common challenge of ocean and Earth system models in this region. This bias was partly mitigated by improving the representation of the export and burial of organic detritus to the deep ocean (e.g., sinking speed, riverine lithogenic material inputs that protect organic material and burial fraction), and water-column denitrification (e.g., nitrate-based respiration at higher oxygen levels) using observational constraints. These results indicate that the regional MOM6-COBALT-IND12 v1.0 model is well suited for physical and biogeochemical studies on timescales ranging from weeks to decades, in addition to supporting marine resource applications and management in the northern Indian Ocean.

Published by Copernicus Publications on behalf of the European Geosciences Union.

1 Introduction

The northern Indian Ocean (from 8.6° S to the northern continental boundaries and 32 to 114° E) is central to the livelihood and economy of about one third of the Earth's population which lives in its littoral countries (e.g., India, Indonesia, Pakistan, Bangladesh, Tanzania, Myanmar, Malaysia, Kenya, and Yemen) and provides valuable resources via the "blue economy", such as fishery, aquaculture, and marine tourism (Roy, 2019). A major challenge to understand and anticipate the response of Indian Ocean ecosystems is to account for the full range of spatio-temporal variability and human-driven changes that control the climatic and environmental conditions defining the habitat, success and survival of these ecosystems (Phillips et al., 2021; Pinsky et al., 2013; Deutsch et al., 2015). On seasonal and interannual time-scales, the Indian monsoon and the Indian Ocean Dipole (IOD) control the ocean circulation and regulate temperature (Schott and McCreary, 2001; Saji et al., 1999; Beal et al., 2013), oxygen levels (Resplandy et al., 2012; Vallivattathillam et al., 2017; Pearson et al., 2022; Al Azhar et al., 2017) and primary productivity (Barber et al., 2001; Gauns et al., 2005; Prakash and Ramesh, 2007; Lévy et al., 2007; Kumar et al., 2010; Wiggert et al., 2009; Resplandy et al., 2011; Currie et al., 2013; Sarma and Dalabehera, 2019), with implications for the spatial and temporal distribution of species that are commercially valuable such as tuna, and key to local food security such as small pelagic fish (e.g., Jebri et al., 2020; Wang et al., 2023).

On decadal and multi-decadal timescales, the Indian Ocean has undergone rapid warming, with an increase in sea surface temperature (SST) by about 1 °C since the 1950s (Roxy et al., 2020), a decline in primary productivity (Sunanda et al., 2023; Sridevi et al., 2023; Gregg and Rousseaux, 2019; Dalpadado et al., 2021), and a significant loss in oxygen in the Arabian Sea and Bay of Bengal (Banse et al., 2014; Piontkovski and Al-Oufi, 2015; Queste et al., 2018; Rixen et al., 2019a; Naqvi, 2019; Löscher, 2021; Lachkar et al., 2023) as well as in the water masses supplying oxygen to the Indian Ocean (Helm et al., 2011; Ito et al., 2017; Naqvi, 2021; Ditkovsky et al., 2023). Warming, decline in primary productivity, and oxygen loss are projected to continue in the Indian Ocean unless greenhouse gas emissions are rapidly curtailed (Bopp et al., 2013; Kwiatkowski et al., 2017, 2020; Roxy et al., 2020; Lachkar et al., 2018, 2019; Lévy et al., 2022; Ditkovsky et al., 2023; Sharma et al., 2023). Warming is also expected to weaken the monsoon despite a potential increase in extreme rainfall events (e.g., Sooraj et al., 2015; Singh et al., 2019; Roxy et al., 2020). This could modify the supply of freshwater and nutrients to coastal waters, and increase the frequency of extreme positive IOD events (Roxy et al., 2020; Cai et al., 2021), which are known to induce weather extremes (Cai et al., 2021), promote primary productivity in the eastern tropical Indian Ocean (e.g., Wiggert et al., 2009; Currie et al., 2013) and lead to low coastal oxygen levels (coastal hypoxia) in the eastern Bay of Bengal (Pearson et al., 2022). Projections from Coupled Model Intercomparison Project (CMIP) models suggest substantial shifts in net primary production and sharp declines in pH in the coming decades, highlighting the northern Indian Ocean's particular vulnerability to climate change (Sunanda et al., 2021, 2023). Observations indicate that these changes have already impacted ecosystems in the Indian Ocean. For instance, do Rosário Gomes et al. (2008) found that the dominant phytoplankton group during the winter bloom in the Arabian Sea shifted from diatom to dinoflagellate in recent decades in response to warming and oxygen loss, with potentially large implications for the functioning of this ecosystem. In coastal areas, the effect of natural variability associated with the seasonal monsoon and interannual IOD combines with global warming and anthropogenic activities (waste waters, urbanization, fertilizers etc.) leading to coastal hypoxic events and in extreme cases to massive mortality events with implications for coastal fisheries and aquaculture (low oxygen levels, Naqvi et al., 2009; Naqvi, 2021, 2022; Pearson et al., 2022).

Models are powerful tools for exploring the Indian Ocean's response to climate variability and anthropogenic changes, identifying the processes at play, and assessing the impacts on biogeochemistry and ecosystems (e.g., Sengupta et al., 2001; Rahaman et al., 2014; Lachkar et al., 2018, 2019; Resplandy et al., 2011, 2012; Schmidt et al., 2021; Ditkovsky et al., 2023; Sunanda et al., 2024). Yet, global ocean and Earth system models are plagued by strong biases in the circulation and biogeochemical dynamics in the Indian Ocean (Séférian et al., 2020; Rixen et al., 2020; Li et al., 2016). In particular, global models tend to misrepresent the circulation that regulates the exchanges between the Indian Ocean and the Pacific Ocean (i.e., the Indonesian throughflow), the overflows from marginal seas (Red Sea and Persian Gulf; Lachkar et al., 2019; Schmidt et al., 2021; Ditkovsky et al., 2023), as well as the mesoscale features (eddies and filaments) key to the ocean circulation, biological production, and the supply of nutrients and oxygen in the Indian Ocean (e.g., Wirth et al., 2002; Resplandy et al., 2011, 2012; Nuncio and Kumar, 2012; Vic et al., 2014; Lachkar et al., 2016; Greaser et al., 2020; Vinayachandran et al., 2021). These shortcomings of global models strongly limit our ability to evaluate the biogeochemical and ecosystem response to climate variability and change. It is with these applications in mind that we configured, customised and validated the regional Indian Ocean simulation based on the Modular Ocean Model 6 (MOM6, Adcroft et al., 2019) coupled with the Carbon, Ocean, Biogeochemistry, and Lower Trophics module version 2.0 (COBALTv2, Stock et al., 2014, 2020). The model configuration, called MOM6-COBALT-IND12 version 1 (or MOM6-COBALT-IND12 v1.0), covers the northern Indian Ocean at a horizontal resolution of $1/12°$ and is designed for physical-biogeochemical studies as well as applications to ecosystems, marine resources and management (Fig. 1).

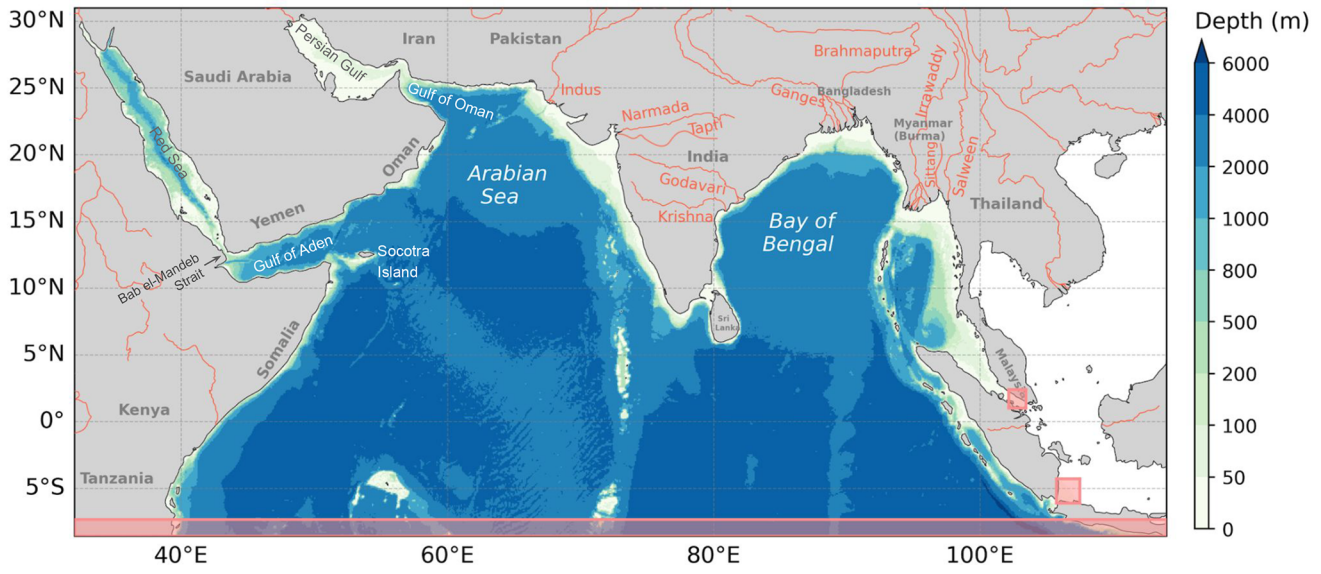

Figure 1. Domain and bathymetry of the regional Indian Ocean MOM6-COBALT-IND12. Pink shading indicates the extent of sponge layers (see Sect. 2.2.2). Major rivers are indicated in red. Socotra Island and the Bab-el-Mandeb Strait are labeled on the map.

In the following sections, we first present the model physical and biogeochemical configuration (Sect. 2) and the data and metrics used to assess the model (Sect. 3). We then evaluate key monsoon-driven seasonal patterns (Sect. 4), ocean interior ventilation and oxygen minimum zones (OMZs) distribution (Sect. 5), as well as intraseasonal and interannual variability (Sects. 6 and 7) simulated in the model. Finally, we discuss the main strengths and limitations of the model configuration (Sect. 8).

2 Regional Indian Ocean configuration

In this section, we describe the regional model configuration MOM6-COBALT-IND12 v1.0 (called MOM6-COBALT-IND12 in the following), which couples an physical ocean model with a biogeochemical module.

2.1 Physical ocean model configuration

The Indian Ocean regional model is based on the Geophysical Fluid Dynamics Laboratory (GFDL) ocean-ice model MOM6 (Adcroft et al., 2019). In the horizontal, the model uses an Arakawa C-grid (Arakawa and Lamb, 1977). The regional configuration MOM6-COBALT-IND12 covers the Arabian Sea and Bay of Bengal and extends to the equatorial Indian Ocean ending south of Java with one open boundary (32 to 114° E and 8.6° S to 30.3° N; Fig. 1). The horizontal resolution is 1/12° (486 × 984 tracer points on the horizontal), with the horizontal grid spacing varying from 9.2 km at the equator to 7.3 km at 30° N. This resolution resolves the first baroclinic radius of deformation with at least 2 grid points and is smaller than the third baroclinic radius of deformation ($R_3 \geq 13$ km) everywhere in the domain except in the Persian Gulf and on the coastal shelf along the eastern Arabian Sea (Chelton et al., 1998; Hallberg, 2013). MOM6-COBALT-IND12 is therefore considered an "eddy resolving" model for the region with a rectilinear and orthogonal grid (32 to 114° E and 8.6° S to 30.3° N).

In the vertical, the model includes a 75-layer hybrid z^*-isopycnal coordinate system with a z^* layers near the surface (about 2 m thick in the upper 20 m in the tropical Indian Ocean) and modified potential density layers below (identical to the hybrid z^*-isopycnal coordinate developed in Adcroft et al., 2019, see Fig. 2). The model bathymetry was generated using the General Bathymetric Chart of the Oceans version 2020 (GEBCO; Weatherall et al., 2015) by averaging the GEBCO bathymetry (provided at a resolution of 15 arcsec) over each grid cell. The depths of the channel connecting the Red Sea bottom waters and the Arabian Sea (region in 12.5–14.2° N, 42.375–43.375° E) are set to 220 m to allow the outflow. The shallowest bathymetry in the model is 4 m. The model is integrated in time using a split explicit method (Runge–Kutta second-order scheme; Hallberg and Adcroft, 2009). The baroclinic time-step is 600 s and the thermodynamic and biogeochemical time-step are 1800 s (Table 1). Using an 18-node setup with 40 cores per node, which distributes the 486 × 984 model grid across available processing units, the model can run one year of simulation in about 16 h of wall clock time (this includes the output of extensive diagnostics).

The configuration of subgrid-scale parameterizations used in MOM6-COBALT-IND12 are based on that of the GFDL Ocean Model version 4 (OM4; Adcroft et al., 2019). We use a background kinematic viscosity and a background diapy-

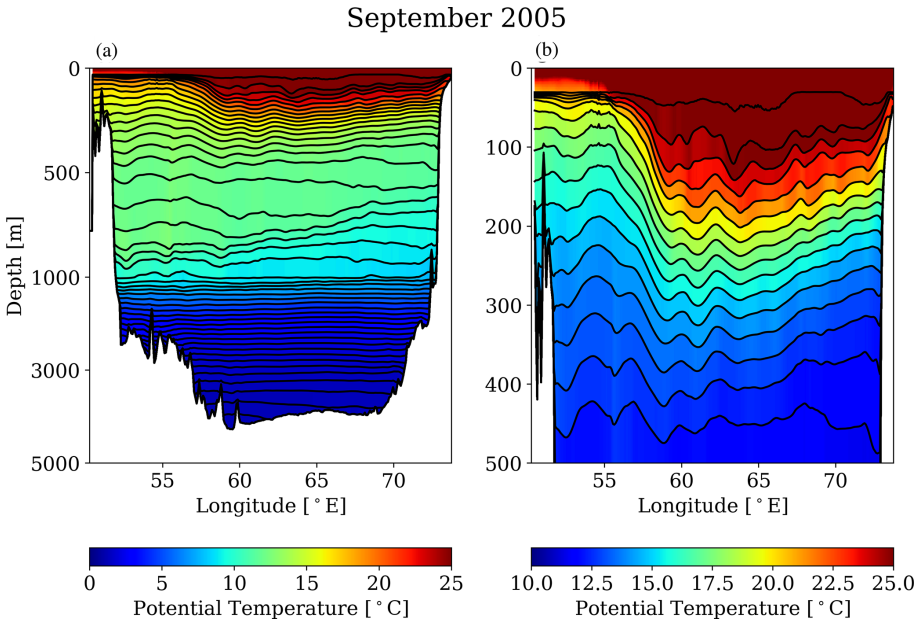

Figure 2. West-east cross-section of the Arabian Sea at 15° N showing the structure of the isopycnal vertical coordinate (contours) overlain with potential temperature (colors) in September 2005 **(a)** over the full column and **(b)** over the top 500 m. The z^* layers in the upper ocean are not shown. The coordinate follows the pattern of the wind-driven upwelling along the coast of Yemen in the west, and the coastal Kelvin wave-driven upwelling along the Indian coast in the east.

cnal diffusivity of 1.5×10^{-5} m^2 s^{-1} (Table 1). As in OM4, viscosity beyond background levels is evaluated as the maximum of a Smagorinsky and resolution-dependent biharmonic viscosity (Griffies and Hallberg, 2000). Additional mixing is represented by planetary boundary layer mixing (Reichl and Hallberg, 2018; Reichl and Li, 2019), shear mixing (Jackson et al., 2008), and mixed-layer restratification due to submesoscale processes (Fox-Kemper et al., 2011). MOM6-COBALT-IND12 also includes bottom boundary layer mixing as in OM4, but the mixing efficiency parameter of this scheme is lowered from 0.2 in OM4 to 0.01 following Ross et al. (2023). The model explicitly resolves barotropic tidal forcing (see next section) and low-mode internal tides are well resolved at $1/12°$ resolution; however, we parameterize the local dissipation of high-mode internal tides according to topographic roughness data (St. Laurent et al., 2002; Polzin, 2009). See Table 1 for a list of configuration parameters.

2.2 Physical ocean model forcing

2.2.1 Initial state, spin-up and atmospheric forcing

The ocean model was initialized using temperature and salinity from annual mean fields from the World Ocean Atlas version 2013 (WOA13; Locarnini et al., 2014; Zweng et al., 2014). Our simulations were run using the atmospheric forcing from the 1/4° horizontal resolution European Center for Medium-range Weather Forecasts reanalysis 5th generation (ERA5) at 1 h frequency (Hersbach et al., 2020). In the ocean model, air–sea heat fluxes were computed using the bulk algorithm of Large and Yeager (2004), which requires atmospheric input variables referenced at 10 m. As the ERA5 forcing provides near-surface temperature and humidity at 2 m, these variables were vertically adjusted to 10 m following the procedure recommended by Large and Yeager (2004), ensuring consistency with the algorithm's assumptions. The sea surface salinity (SSS) was restored to the polar science center hydrographic climatology (PHC2.1), which is based on the World Ocean Atlas 98 with data replenishment in the Arctic Ocean (Steele et al., 2001), with a piston velocity of 0.1667 m d^{-1}. We conducted a 32-year spin-up, consisting of four consecutive 8-year loops of the 1980 to 1987 forcing field, and reached a well-equilibrated state with minimal linear trends of physical and biogeochemical variables (e.g., drift in SST, SSS, oxygen, nitrate, primary production and ocean surface partial pressure of carbon dioxide $pCO_2 < \sim 0.1$ % for spin-up years 17–32). Using outputs from the end of the spinup simulation as initial conditions, the hindcast simulation was started on 1 January 1980 and was run from 1980 to 2020 for our analysis in this study.

2.2.2 Open boundary conditions and tidal forcing

Open boundary conditions (OBC) are set using the Flather formulation for the tidal and sub-tidal sea level and barotropic velocity and the Orlanski formulation for the baroclinic velocity (Flather, 1976; Orlanski, 1976). In addition, we nudge the boundary values towards external forcing with

Table 1. Major parameters and associated values used in the physical ocean (MOM6) component of the model.

Parameter	Value	Reference
Vertical coordinate	75 layer hybrid z^*-isopycnal	Adcroft et al. (2019)
Baroclinic time step	600 s	
Thermodynamic and BGC time step	1800 s	
Planetary boundary layer parameterization	ePBL	Reichl and Hallberg (2018)
Submesoscale eddy front length	500 m	Fox-Kemper et al. (2011)
Biharmonic viscosity	Maximum of Smagorinsky and resolution-dependent viscosities	Griffies and Hallberg (2000)
Smagorinsky coefficient	0.06	
Resolution-dependent	$0.01\Delta_x^3$ m^4 s^{-1}	Adcroft et al. (2019)
Bottom boundary layer mixing efficiency	0.01	Legg et al. (2006)
Background kinematic viscosity	1.5×10^{-5} m^2 s^{-1}	
Background diapycnal diffusivity	1.5×10^{-5} m^2 s^{-1}	
Boundary Conditions		
Sea level and barotropic velocities	Flather scheme	Flather (1976)
Baroclinic velocities	Radiation scheme and nudging (3 d inflow and 360 d outflow)	Orlanski (1976) and Marchesiello et al. (2001)
Temperature and salinity	Reservoirs with 9 km length scale	Ross et al. (2023)
Biogeochemical tracers	Reservoirs with 9 km outflow length scale and 300 km inflow length scale	
Tidal SAL coefficient	0.094	Irazoqui Apecechea et al. (2017) Stepanov and Hughes (2004), Barton et al. (2022)
Opacity Scheme	3-band with chlorophyll	Manizza (2005)
Piston velocity for SSS relaxation	0.1667 m d^{-1}	Adcroft et al. (2019)

a strong 3 d time-scale for baroclinic normal and tangential velocities entering the model and a weak 360 d time-scale for outgoing velocities (Marchesiello et al., 2001). The boundary value for temperature and salinity are set using a reservoir in which the properties are evolving based on contributions from an inflow (properties outside of the domain set by an boundary forcing file) and outflow (properties simulated inside the model domain) fluxes. Similarly to Ross et al. (2023), the inflow and outflow length scales are set to 9 km (about 1–10 d time-scale for velocities of 10^{-1} cm s^{-1}) for temperature and salinity (i.e., inflow and outflow have an equal contribution to the boundary reservoir). The model includes a sponge layer over 15 grid points at the southern open boundary, nudging the model to time-varying Ocean Reanalysis System 5 (ORAS5) temperature and salinity with a time-scale increasing from 12 d at the boundary to 174 d at the 15th grid point. The model also includes two sponge layers at the closed boundaries of the Malacca and Sunda Straits with a nudging to the climatological WOA18 data. For the Malacca Strait, temperature and salinity are nudged over 15 grid points with a time-scale increasing from 12 d at the strait outlet to 174 d toward the Indian Ocean. In the Sunda Strait, the nudging is over 21 grid points and the time-scale increases from 12 d at the outlet to 336 d toward the Indian Ocean.

Ten tidal components (i.e., M2, S2, N2, K2, K1, O1, P1, Q1, Mm, and Mf) interpolated from the inversion of TOPEX/POSEIDON crossover data TPX09 (Egbert and Erofeeva, 2002) are used to generate surface elevation and velocity forcing at the open boundary. Tidal potential forcing from the same ten components is included in the barotropic momentum equations throughout the domain, and the effects of self-attraction and loading are represented using the scalar approximation (Accad and Pekeris, 1978) with a coefficient of 0.094. Sub-tidal velocities, temperature and salinity at the southern open boundary are from the monthly ORAS5 (Zuo et al., 2019).

2.2.3 River freshwater discharge

Freshwater discharge from rivers was prescribed using the gridded daily Global Flood Awareness System (GloFAS) reanalysis version 4.0, as described by Grimaldi et al. (2022) and Harrigan et al. (2023). To map the river discharge data onto the MOM6-COBALT-IND12 grid, we used the GloFAS local drainage direction map to identify outlet points adjacent to the coast, as well as any chains of outlet points connected to these coastal outlets, see details in Burek et al. (2013). The streamflow at these outlet points was introduced at the surface of the nearest model coastal ocean grid cell. To ensure the riverine freshwater flux is mixed into the water column, an extra input of turbulent kinetic energy extending down to a depth of 10 m was included at the discharge points (Tseng et al., 2016). By comparing GloFAS to published discharge observations (Jian et al., 2009; Siswanto et al., 2023), we found that GloFAS overestimated discharge in the Ganges-Brahmaputra river system, and therefore scaled down the freshwater discharge by 25 % to match observations in these two rivers (see Fig. A1; Jian et al., 2009; Siswanto et al., 2023). Additionally, we found that GloFAS underestimated runoff in the Irrawaddy-Sittang river system. To correct for this bias, we applied a linear regression-based correction (see Fig. A1) between the original GloFAS discharge and discharge data from the Global Runoff Data Centre (GRDC; Recknagel et al., 2023) for the Irrawaddy-Sittang regions. Finally, we manually removed discharge in the model sponge layers of the Sunda Strait and Malacca Strait.

2.3 Biogeochemical model configuration and changes specific to Indian Ocean

The physical ocean model is coupled to the COBALT v2 (Stock et al., 2014, 2020). COBALTv2 represents 33 tracers including nutrients (nitrate, phosphate, silicate, and iron), three phytoplankton groups (small, large, diazotrophs), three zooplankton groups (small, medium, large), three dissolved organic carbon pools (labile, semi-refractory and refractory), one particulate detritus pool, oxygen, and carbonate system.

Several parameters of the standard COBALTv2 model from Stock et al. (2020) were modified to match observational constraints and characteristics of the Indian Ocean and improve model biases, including a bias in the extent and volume of the OMZ in the Bay of Bengal.

- Detritus sinking velocity was increased from 100 to $120\,\mathrm{m\,d^{-1}}$, based on *in-situ* sediment trap observations indicating sinking speeds up to 160–$280\,\mathrm{m\,d^{-1}}$ in the Indian Ocean (Rixen et al., 2019b).

- The burial fraction was increased (the equivalent half-saturation in the denominator of Eq. 3 from Dunne et al., 2007, was reduced from 7 to $1\,\mathrm{mmol\,C\,m^{-2}\,d^{-1}}$) . This increased the burial of particulate organic carbon from 0.013 to $0.026\,\mathrm{Pg\,C\,yr^{-1}}$ in the tropical Indian Ocean, in better agreement with the burial of $0.028\,\mathrm{Pg\,C\,yr^{-1}}$ found in the observation-based reconstruction of LaRowe et al. (2020).

- The oxygen half-saturation for nitrification ($k_{\mathrm{nit,O_2}}$ in Stock et al., 2020) was reduced from 3.9 to $2.0\,\mu\mathrm{mol\,O_2\,kg^{-1}}$, based on recent observations indicating a lower oxygen threshold for ammonium oxidation in the OMZs (Bristow et al., 2016; Peng et al., 2016; Frey et al., 2023).

- The oxygen constraint on water column denitrification was modified from $O_{2,\min}/(k_{\mathrm{O_2}} + O_{2,\min})$ when $\mathrm{O_2} < 0.8\,\mu\mathrm{mol\,kg^{-1}}$ (see Appendix A3 in Stock et al., 2020) to $\mathrm{O_2}/(k_{\mathrm{O_2}}+\mathrm{O_2})$ when $\mathrm{O_2} < 4.0\,\mu\mathrm{mol\,kg^{-1}}$, in line with findings that the oxygen threshold below which denitrification starts is typically between 4 and $5\,\mu\mathrm{mol\,kg^{-1}}$ (Paulmier and Ruiz-Pino, 2009).

2.4 Biogeochemical model forcing

2.4.1 Initial state, open boundary conditions and model drift

For the model spin-up, nutrients (nitrate, phosphate, and silicate) and oxygen were initialized using annual means from the World Ocean Atlas 2018 (WOA18; Garcia et al., 2019). Dissolved inorganic carbon (DIC) and alkalinity were initialized using annual means from the Global Ocean Data Analysis Project version 2 (GLODAPv2), which are representative of year 2002 (Olsen et al., 2016). Other biogeochemical tracers were initialized with very low seed values of $10^{-10}\,\mathrm{mol\,kg^{-1}}$. This initial value has a negligible impact on the solution as most of these remaining tracers have turnover time-scales much shorter than the 32-year spin-up duration (e.g., typically of a few days for phytoplankton), except semi-refractory dissolved organic matter (decay time-scale of 10 years). Atmospheric CO_2 forcing was taken from the global carbon budget project (Friedlingstein et al., 2022). Biogeochemical boundary values are prescribed from WOA18 monthly climatologies for nitrate, phosphate, silicate, and oxygen. For DIC and alkalinity boundary values, annual mean fields were estimated using the Empirical Seawater Property Estimation Routines (ESPER) MATLAB code (Carter et al., 2021), based on annual mean temperature and salinity from ORAS5. The OBC for biogeochemical tracers is set using the reservoir scheme (see Sect. 2.2), with an outflow length scale of 9 km but an increased inflow length scale of 300 km, giving more weight to the solution within the model domain. This decoupling between contributions from the inflow and outflow limits the influence of the boundary external forcing on the model domain, specifically when the fields at the boundaries are poorly constrained such as for biogeochemical tracers. Model drift after the 32-year spin-up and over the 41 years of a hindcast simulation with constant forcing is small, with linear trends < 0.05 %

for oxygen, nitrate, DIC, alkalinity, semi-refractory dissolved organic nitrogen pools and integrated primary productivity (Fig. A2). The slight drift indicates that the hindcast simulation starts from a well-equilibrated initial state provided by the spin-up simulation.

2.4.2 Atmospheric deposition

The model is forced with monthly atmospheric deposition of nitrogen (wet and dry deposition of nitrate and ammonium), iron, phosphorus, and lithogenic dust derived from the archived GFDL Earth system model version 4.1 (ESM4.1) historical simulation (https://www.wdc-climate.de/ui/cmip6?input=CMIP6.CMIP.NOAA-GFDL.GFDL-ESM4.historical, last access: 15 July 2023) (1980–2014) and Shared So (https://www.wdc-climate.de/ui/cmip6?input=CMIP6.ScenarioMIP.NOAA-GFDL.GFDL-ESM4.ssp585, last access: 15 July 2023) (2014–2020; Stock et al., 2020; Horowitz et al., 2020; Paulot et al., 2020). ESM4.1 includes interactive modules for anthropogenic and natural (e.g., biomass burning, lightning) reactive nitrogen emissions, photochemical reactions, removal of nitrogen by wet and dry deposition, as well as a land-atmosphere-ocean cycling of dust and ocean ammonia outgassing (Paulot et al., 2020; Horowitz et al., 2020). Interannual variability in ESM4.1 is not in phase with observed variability (as for any coupled Earth system model). For dry and wet deposition of oxidized and reduced nitrogen, we therefore used a 15-year moving by month average (e.g., January 2000 is an average of all Januaries between years 1993 and 2007) that retain the seasonality and the decadal anthropogenic increase in deposition but removed the interannual variability (see Fig. A3). For iron, phosphorus and lithogenic material deposition, we used monthly mean climatologies over the 1950–2022 period (ESM4.1 does not include the effects of fossil fuel burning etc. that would yield a significant long term trend in these fields, although it would include the smaller impact of long-term wetting/drying, wind and/or precipitation trends that we ignore here). Iron and dry lithogenic dust depositions are from ESM4.1 outputs. Phosphorus deposition was evaluated using the ESM4.1 climatology in dry lithogenic dust deposition, assuming a phosphorus content of 563 ppm in dust, of which 22 % is bioavailable (see Herbert et al., 2018; Ross et al., 2023). See details about the influence of atmospheric deposition in this model in Malsang et al. (2024).

2.4.3 River biogeochemical inputs

The riverine fluxes of dissolved and particulate nutrients (nitrogen and phosphorus) are derived from the annual mean loads of inorganic and organic nitrogen and phosphorus from the Global Nutrient Export from WaterSheds2 (GlobalNEWS2), referenced to the year 2000 (Mayorga et al., 2010). We include riverine inputs of dissolved inorganic nitrogen (DIN), dissolved inorganic phosphorus (DIP), dissolved organic nitrogen (DON), dissolved organic phosphorus (DOP), and bio-available particulate organic nitrogen (PON). We do not include bio-available particulate organic phosphorus (POP) as the river input of DIP is already likely too high in GlobalNEWS2 (Jiao et al., 2023). DON and DOP are distributed among different dissolved organic pools, with 30 % allocated to the labile pool, 35 % to the semi-labile pool, and 35 % to the semi-refractory pool (Wiegner et al., 2006). The riverine PON is assumed 100 % bio-available.

The riverine input of iron is set at a value of 70 nmol kg^{-1} based on Raiswell and Canfield (2012). In the Bay of Bengal (78–103° E) region, the riverine DIN concentration is reduced by 80 % based on coastal nitrate data collected by Krishna et al. (2016). This adjustment is supported by Zhou et al. (2022) and Jiao et al. (2023), which compared several global nutrient transport models highlighting that GlobalNEWS2 tended to overestimate total nitrogen riverine inputs. The riverine flux of DIN in the Arabian Sea and the flux of other nutrients in both the Arabian Sea and Bay of Bengal are kept equal to the original values from GlobalNEWS2. The riverine inputs of DIC (0.32 mol m^{-3}) and alkalinity (0.42 mol equivalents of alkalinity m^{-3}) are assigned constant concentrations, consistent with those used in the GFDL-ESM4.1 Earth system model (Stock et al., 2020).

To reflect spatial differences in sediment supply, we specify riverine lithogenic concentrations based on observational data from Milliman and Farnsworth (2011). The lithogenic input from rivers was adjusted to 200 g m^{-3} for major rivers (i.e., rivers with sediment loads exceeding 10 Mt yr^{-1}, e.g., Godavari, Krishna, Ganges, Brahmaputra, Irrawaddy, Sittang, Salween, Indus, Tapti and Narmada rivers; see Fig. 1 for rivers location) and 20 g m^{-3} for all other rivers, rather than applying a global constant of 13 g m^{-3} used for all rivers as in Stock et al. (2020). These adjustments account for the significantly higher total suspended sediment loads in these rivers (Milliman and Farnsworth, 2011; Rixen et al., 2019b), and are supported by river observations from Milliman and Farnsworth (2011) showing a broad range from 10 g m^{-3} (Muvattupuzha River) to 1061 g m^{-3} (Ganges River). In the model, this higher lithogenic flux protects more particulate organic matter from remineralization, thereby increasing organic carbon export to the deep ocean and reducing oxygen consumption in the subsurface. This is in line with observations that underscore the significant role of lithogenic matter in reducing organic matter remineralization and accelerating carbon export in the northern Indian Ocean (Rixen et al., 2019b).

These concentrations of nutrients, DIC, alkalinity, lithogenic and organic material (constant in time) are incorporated using the GloFAS freshwater inputs and by assigning them to the nearest neighboring river mouths, with larger rivers given priority over smaller ones. Nutrient loads vary in accordance with changes in river discharges, and the baseline

configuration presented in this study does not account for the fluctuations and trends in observed nutrient concentrations during the 1980-2020 model simulation period.

3 Methods for assessing model spatial and temporal variability

3.1 Physical and biogeochemical datasets

We used satellite and *in-situ* observations to assess modeled physical and biogeochemical basin-scale patterns as well as seasonal, interannual and intraseasonal variability. See Table 2 for a list of all datasets and their references.

For the basin-scale evaluation of physical fields, we used Argo gridded temperature (Roemmich and Gilson, 2009), temperature and salinity from the WOA18 (Garcia et al., 2019), satellite-based SST from the Optimum Interpolation SST (OISST) version 2.1 (Banzon et al., 2016), sea surface height (SSH) and sea level anomaly from AVISO and distributed by the Copernicus Marine and Environment Monitoring Service (CMEMS; http://www.marine.copernicus.eu, last access: 10 August 2023), the mixed layer depth (MLD) climatology from De Boyer Montéut et al. (2004) (updated in November 2008; https://mld.ifremer.fr/Surface_Mixed_Layer_Depth.php, last access: 10 June 2023) and ocean surface currents from the OSCAR drifter database (ESR, 2009). In addition, we used data from the Research Moored Array for African-Asian-Australian Monsoon Analysis and Prediction (RAMA), specifically from two moorings capturing the east-west contrast in the basin at 57° E, 4° S and 95° E, 5° S (data downloaded from the Pacific Marine Environmental Laboratory NOAA website; McPhaden et al., 2009), and observations from water mass properties at the Red Sea outflow from Sofianos et al. (2002).

For the basin-scale biogeochemical model evaluation, we used oxygen concentrations from WOA18 (Garcia et al., 2019) and from Bianchi et al. (2012), surface chlorophyll data from the European Space Agency ocean color climate change initiative (OC-CCI version 5.0; Sathyendranath et al., 2019), vertical chlorophyll data from bio-Argo (Wong et al., 2020), and integrated primary productivity from the satellite-based Carbon-based Production Model (CbPM) algorithm, the Carbon, Absorption, and Fluorescence Euphotic-resolving (CAFE) algorithm, the Vertically Generalized Production Model (Standard-VGPM) algorithm and its alternative formulation (Eppley-VGPM), all accessed via the Ocean Productivity website (http://sites.science.oregonstate.edu/ocean.productivity/index.php, last access: 10 December 2023). In addition, we used *in-situ* observations compiled from a literature review including 24 studies and 351 stations (see Table 2 for references). River inputs and particulate organic and lithogenic matter in the model were evaluated using river discharge from the Global Runoff Data Center (GRDC; Recknagel et al., 2023).

3.2 Analysis and evaluation metrics

We evaluated the amplitude of intraseasonal variability (ISV) using SSH temporal variability as a proxy for mesoscale eddies and planetary waves (Rossby and Kelvin waves; e.g., Cheng et al., 2013). Observed and simulated SSH were detrended using a linear regression and filtered using a 14–120 d band pass filter to remove the seasonal cycle, interannual variability and long-term trend, and only retain the intraseasonal timescales. The Dipole Mode Index (DMI) used to evaluate IOD phases was calculated as the SST anomalous gradient between the western equatorial Indian Ocean (50–70° E and 10° S–10° N) and the southeastern equatorial Indian Ocean (90–110° E and 10° S–0° N, Saji et al., 1999). Finally, we used three metrics throughout the study to compare model results and observations: the Pearson correlation coefficient (r) which measures the correlation between observations and model in time (for time-series) or in space (for maps), the root mean square error (RMSE, i.e., quadratic mean of model minus observations) which measures the model accuracy compared to observations, and the bias (i.e., model minus observations) which indicates if the model underestimates or overestimates the observed fields. For the validation of climatological annual and seasonal means, model outputs are averaged over the period 1980–2020. Observation-based data products are treated based on their availability: if the dataset provides climatological means (annual or seasonal), we use the provided values directly. If not, we compute climatological means over the available time span of the observational dataset (see time span in Table 2).

4 Monsoon-driven seasonality

4.1 Sea surface temperature as an indicator of seasonal dynamics

Patterns of SST in the northern Indian Ocean follow the well described basin-scale features associated with the monsoon reversal (e.g., Schott and McCreary, 2001). MOM6-COBALT-IND12 captures seasonal SST patterns well, notably the contrast between the vast warm pool (SST > 28 °C) that extends over most of the basin and the regions with colder SSTs that develop in response to seasonal variations in atmospheric and oceanic circulation (Fig. 3). During the winter monsoon, the model simulates the relatively cold water (SST < 26 °C) associated with evaporative cooling in the northern Bay of Bengal, and a combination of evaporative cooling and convective mixing (MLD of 40–60 m) in the northern Arabian Sea (Figs. 3a–c and 4a–c). During the summer monsoon, the model simulates the colder summer SSTs observed in wind-driven upwelling regions along the western

Table 2. Observational products used to evaluate MOM6-COBALT-IND12.

Parameter	Sampling frequency	Reference dataset
Sea surface temperature	monthly optimum interpolation (1982–2020)	OISSTv2.1 includes satellites, ships, buoys, Argo floats (Banzon et al., 2016)
Mixed-layer depth	monthly climatology	De Boyer Montéut et al. (2004) – updated November 2008
Surface currents	5 d averaged monthly	OSCAR drifter database (ESR, 2009)
Sea level anomaly	daily satellite-based	Copernicus (Lopez, 2018)
Ocean temperature and salinity	monthly climatologies in-situ profiles in-situ profiles	World Ocean Atlas 2018 (WOA18, Garcia et al., 2019) World Ocean Database 2018 (WOD18, Boyer et al., 2018) RAMA moorings (McPhaden et al., 2009)
Wind speed	monthly satellite in-situ	CCMP (Mears et al., 2022) RAMA moorings (McPhaden et al., 2009)
Red Sea Outflow properties	in-situ sampling (1995–1996)	Sofianos et al. (2002)
Oxygen concentration	monthly climatologies	WOA18 (Garcia et al., 2019; Bianchi et al., 2012)
Surface chlorophyll	monthly climatology	OC-CCI v5.0 (Sathyendranath et al., 2019)
River Discharge	daily/annual mean	Global Runoff Data Center (GRDC, Recknagel et al., 2023 Jian et al., 2009; Krishna et al., 2016)
Riverine lithogenic flux	in-situ sampling	Milliman and Farnsworth (2011)
Marine lithogenic/organic flux	in-situ sampling	Rixen et al. (2019b)
Net primary productivity	monthly satellite-based in-situ sampling (351 stations)	CbPM (Westberry et al., 2008), CAFE (Silsbe et al., 2016), standard-VGPM, Eppley-VGPM (Behrenfeld and Falkowski, 1997) Saxena et al. (2023), Marra et al. (2021), Sarma et al. (2020) Löscher et al. (2020), Sarma and Dalabehera (2019) (Ahmed et al., 2017), Gandhi et al. (2010, 2011) Kumar et al. (2010), Naqvi et al. (2010), Prakash et al. (2008) Prasanna Kumar et al. (2007a, b), Naqvi et al. (2006) Gauns et al. (2005), Kumar et al. (2004) Barber et al. (2001), Watts and Owens (1999), Watts et al. (1999) Savidge and Gilpin (1999), McCarthy et al. (1999) Veldhuis et al. (1997), Devassy et al. (1983) Bhattathiri et al. (1980), Radhakrishna (1978)

boundary coasts (e.g., Oman, Yemen, Somalia, Kenya and Tanzania where SST $< 26\,^{\circ}C$), and in the weaker upwelling controlled by Kelvin wave propagation along the southwestern Indian coast (SST $\sim 27\,^{\circ}C$; Fig. 3d–f; see details on wave propagation in Sect. 4.3). At the basin scale, modeled SST patterns shows strong agreement with observed patterns, characterized by a high correlation coefficient ($r>0.97$), low RMSE (0.25–0.3 °C), and small biases (regional mean SST bias of $-0.06\,^{\circ}C$ in winter and $-0.01\,^{\circ}C$ in summer for the 1980–2020 period). We note that the good agreement between observed and modeled SST is in part attributable to the strong influence of the prescribed observation-driven atmospheric surface boundary forcing that controls air-sea heat fluxes in the model (e.g., temperature, wind; see Sect. 2). In addition, a comparison between ERA5 and Cross-Calibrated Multi-Platform (CCMP) wind products demonstrates that ERA5 wind forcing effectively captures the seasonal cycle and spatial distribution of the summer and winter monsoons (Fig. A4).

The model captures the seasonal contrast in MLD between the Arabian Sea and the Bay of Bengal, with deeper mixed layers in the Arabian Sea and shallower layers in the Bay of Bengal during both winter and summer (Fig. 4). The MLD is generally deeper in summer than in winter. The spatial patterns, including the locations of local MLD maxima, are broadly consistent with observational data. Quantitatively, the basin-wide correlation values are similar between the two seasons, although the RMSE is larger in summer (8.09 m) than in winter (7.00 m). One possible contributor to the larger summer bias is the enhanced wind forcing during the mon-

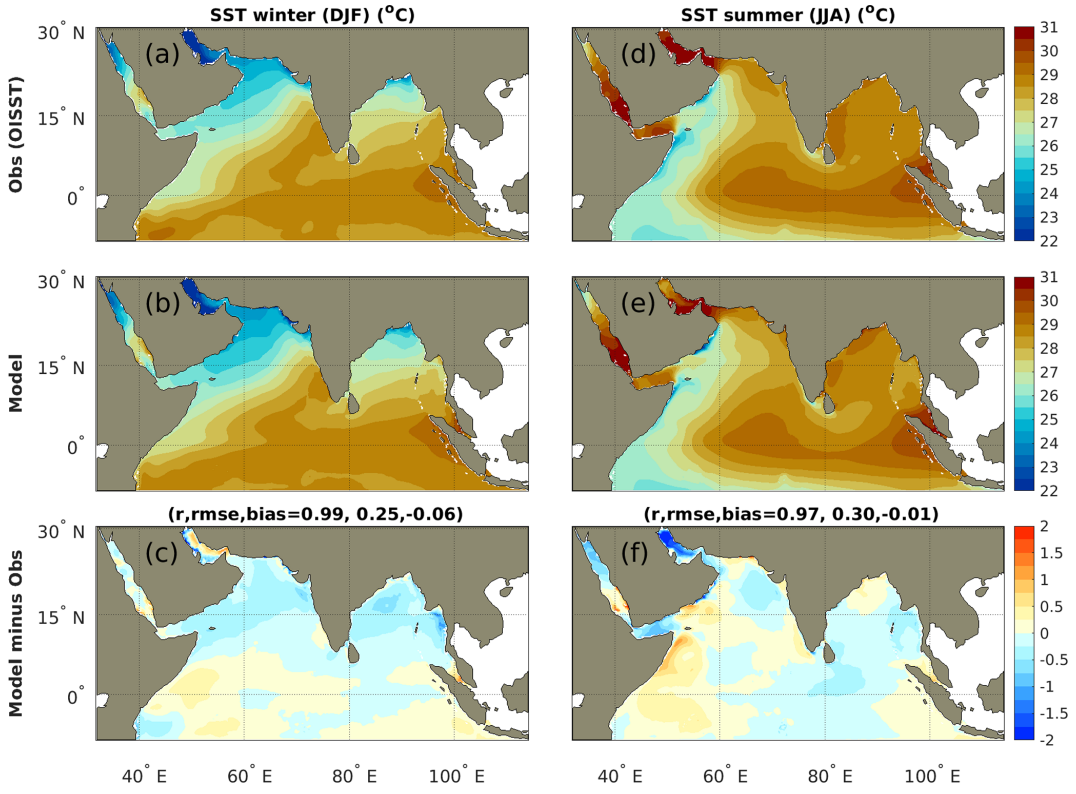

Figure 3. Sea surface temperature (SST) during **(a–c)** winter (December–February) and **(d–f)** summer (June–August) monsoons. Panels **(a, d)** show OISST observations, **(b, e)** show MOM6-COBALT-IND12 model and **(c, f)** show differences between model and observations. Correlation coefficients r, RMSE and bias between the observed and model seasonal means are indicated. See details on observations in Table 2. Model results are averaged over the 1980–2020 period.

soon season (see Fig. A4), which intensifies turbulent mixing and deepens the mixed layer. At the same time, the MOM6 model includes the mixed layer eddy (MLE) parameterization of Fox-Kemper et al. (2011), which represents restratification driven by baroclinic eddies within the mixed layer. This restratification process may also be more active in summer, potentially leading to an overcorrection that offsets vertical mixing too strongly. The interaction between intensified wind-driven mixing and enhanced restratification may thus contribute to the larger MLD bias observed in summer compared to winter.

4.2 Seasonal reversal of upper ocean circulation

MOM6-COBALT-IND12 reproduces the observed seasonal reversal of the main current systems, as confirmed by comparison with the updated OSCAR drifters database (arrows on Fig. 4). In the Equatorial band, these seasonal changes include the shift from an eastward transport by the Northeast Monsoon Current (Equator to 10° N) and westward transport by the South Equatorial Countercurrent (5° S to Equator) in winter, to a mostly westward transport by the the Southwest Monsoon Current in summer (Equator to 10° N, Fig. 4). MOM6-COBALT-IND12 also simulates the summer strengthening and reversal of the western boundary Somali Current system and its extension northward along the Arabian Peninsula (Fig. 4). In the following, we compare the simulated and observed seasonal evolution of this western boundary system, with a focus on the characteristics that are most relevant to the biogeochemical response, and refer the reader to prior work for a more in-depth description of its dynamics (e.g., Schott and McCreary, 2001; Wirth et al., 2002; Brandt et al., 2003; Sengupta et al., 2001; Beal and Donohue, 2013; Beal et al., 2013; Vic et al., 2014; Wang et al., 2018).

Figure 5 compares the simulated and observed seasonal evolution of the western boundary system. MOM6-COBALT-IND12 simulates relatively well the observed climatological evolution of the Somali Current. Before the summer monsoon (April), the Somali Current is relatively weak and flows northward along the western boundary, crossing the Equator in both observations and model. At the onset of the summer monsoon (June), the Somali Current intensifies, and separates at around 4° N into a northward alongshore current and an eastward flow that loops back across the equator and feeds the South Equatorial Countercurrent, a feature also known as the Southern Gyre (Beal et al., 2013). Simultaneously, a quasi-stationary anticyclonic mesoscale gyre called the Great Whirl develops at about 10° N (Fig. 5). As

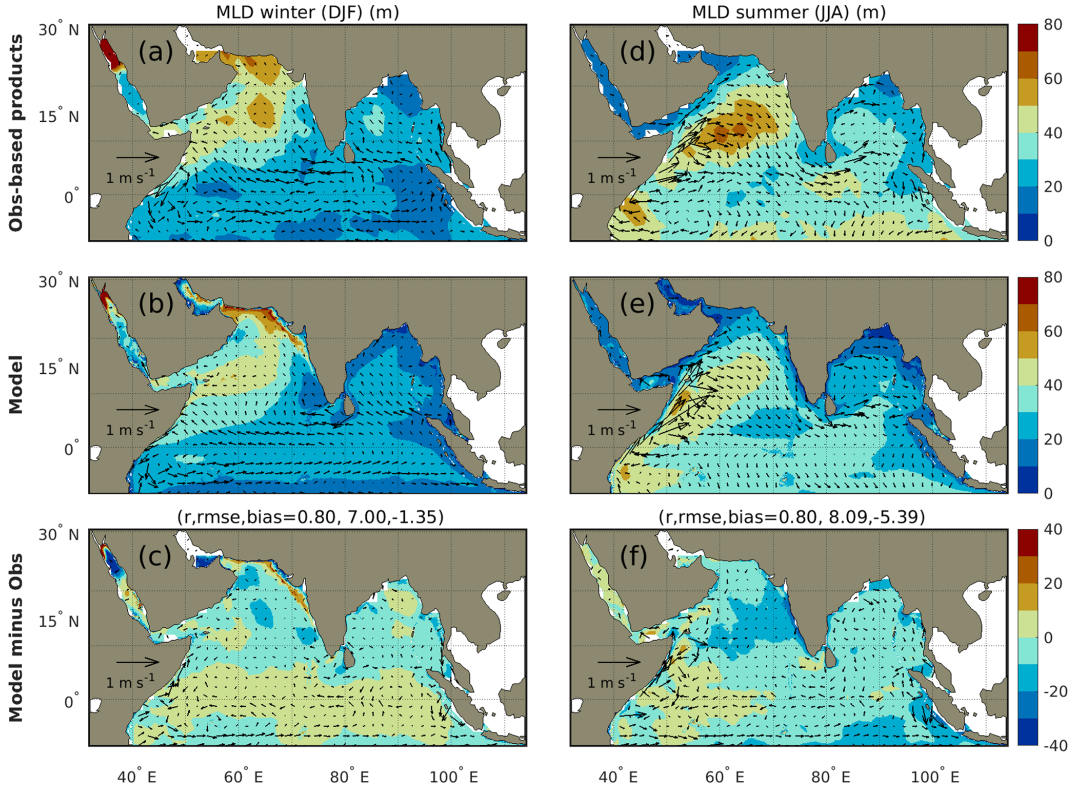

Figure 4. Seasonal mean mixed layer depth (MLD) and surface currents during **(a–c)** winter (December–February) and **(d–f)** summer (June–August) monsoons. Panels **(a, d)** show observations, **(b, e)** show MOM6-COBALT-IND12 model and **(c, f)** show differences between model and observations. Correlation coefficients r, RMSE and bias between the observed and model seasonal MLD means are indicated. Observations are an update of De Boyer Montéut et al. (2004) for MLD and the OSCAR drifters database for surface currents (see Table 2). Model results are averaged over the 1980–2020 period.

the southwest monsoon progresses (August), the Great Whirl intensifies, becoming one of the largest and most energetic coherent vortices in the world ocean. A smaller anticyclonic mesoscale eddy, the Socotra Eddy, also develops east of Socotra Island at this time (Fig. 5). The structure of the Great Whirl at its peak is relatively similar in the model and shipboard and mooring observations, with an horizontal footprint of ~ 500 km, a vertical extent of ~ 1000 m, meridional currents of about 1 m s^{-1} at the surface and 0.1 m s^{-1} at 1000 m depth (Figs. 5 and 6 and observations reported in Schott and McCreary, 2001; Beal and Donohue, 2013). Finally, during the fall intermonsoon (October), the gyre system decays, and by the winter monsoon (December), the surface signature of the Great Whirl and Socotra Eddy are not visible (Fig. 5).

4.3 Coastal upwelling and downwelling

Patterns in sea level anomaly can be used as a proxy for coastal seasonal upwelling (negative anomalies) and downwelling (positive anomalies) motions (Fig. 7a–d). In summer, the model reproduces the amplitude and patterns of wind-driven upwelling along the western Arabian Sea (e.g., Oman, Yemen and Somalia), and western Bay of Bengal (eastern India) coasts (Fig. 7b and d; correlation coefficient $r = 0.91$; RMSE = 0.02 m). We note that the latter upwelling has little influence on SST in both observations and models (Fig. 3) due to the strong near-surface stratification imposed by high freshwater inputs in the Bay of Bengal, and hence the strong atmospheric control on SST in this region (e.g., Shetye et al., 1991; Shenoi et al., 2002). In winter, SLA patterns largely mirror summertime patterns due to the reversal of the winds and ocean circulation, with downwelling motions (positive SLA) that develop along the western Arabian Sea coasts and the western Bay of Bengal (Fig. 7a–d). This pattern is also well captured by the model (Fig. 7a and c; correlation coefficient $r = 0.93$; RMSE = 0.02 m).

Wind-driven upwelling and downwelling are strongly modulated by the seasonal propagation of coastal Kelvin waves around the rim of the northern Indian Ocean (e.g., McCreary et al., 1993; Yang et al., 1998; Nienhaus et al., 2012; Vinayachandran et al., 2021). We examine the evolution of these coastal waves following changes in SLA along the Equatorial and coastal wave guides using the review and description provided in Pearson et al. (2022). Modeled coastal SLA patterns remarkably capture the timing and amplitude of the observed patterns, starting with the equatorial up-

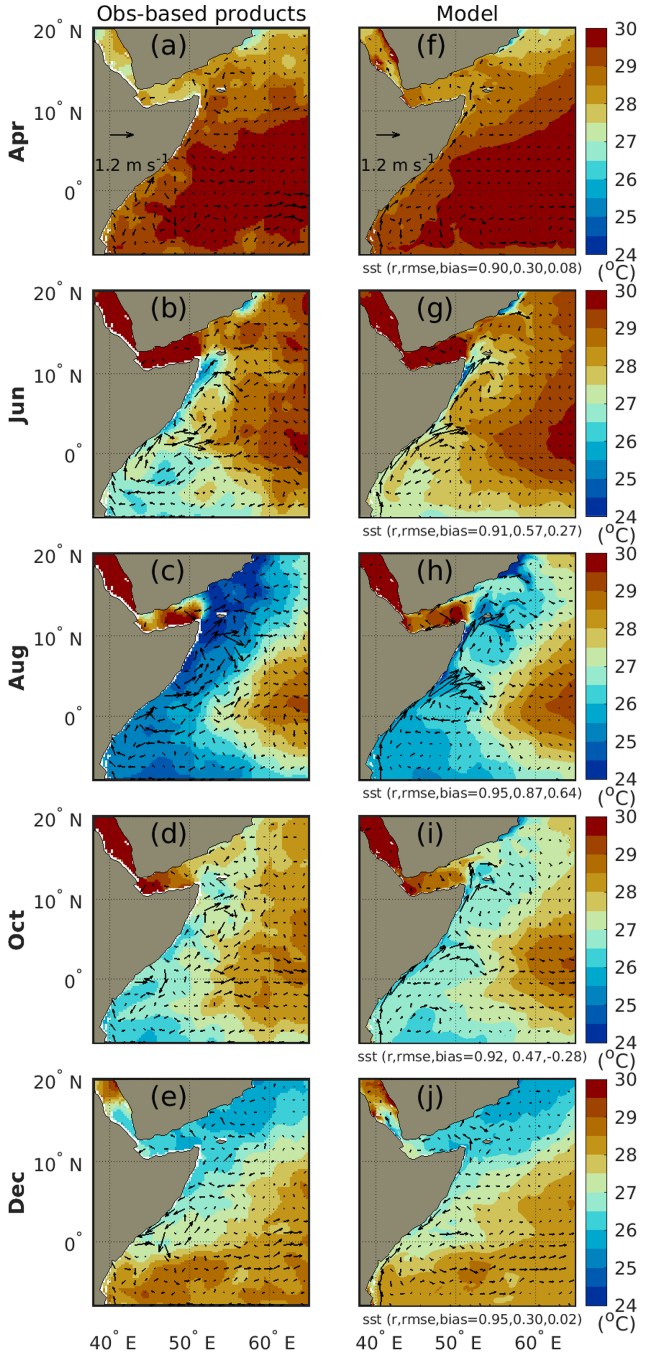

Figure 5. Climatological evolution of the western boundary Somali Current system showing SST (colors) and surface currents (vectors) in observation-based products **(a–e)** and MOM6-COBALT-IND12 **(f–j)**. Observation-based products are from OISSTv2.1 satellite for SST and the OSCAR drifters database for surface currents (see Table 2). Correlation coefficients r, RMSE and bias between the observed and modeled SST means are indicated.

welling Kelvin waves triggered by wind changes in the summer and winter monsoons (arrows for waves I and II), and the equatorial downwelling Kelvin waves triggered during the spring and fall intermonsoons (arrows for waves III and IV on Fig. 7e and f). These successive wave trains travel east and then counter-clockwise around the Bay of Bengal and the Arabian Sea. The model also captures the summer upwelling and winter downwelling waves excited in the northwestern Bay of Bengal (arrow for waves V and VI) and at the tip of India (arrows for waves VII and VIII), reinforcing the wind-driven summer upwelling and winter downwelling (dashed circles) that develop in the western Bay of Bengal and eastern Arabian Sea (Fig. 7e and f). See further details in Pearson et al. (2022) and references herein.

4.4 Sea surface salinity and river plumes

The model reproduces the main observed patterns of SSS (Fig. 8a–f), including the high SSS (SSS $>$ 34 psu) in the Arabian Sea where evaporation exceeds precipitation and riverine runoff, and the much fresher (SSS $<$ 34 psu) Bay of Bengal where precipitation and runoff exceed evaporation. Performance metrics indicate that the simulation achieves a strong spatial correlation (0.95–0.96) and a small regional RMSE (0.53–0.71). It also reproduces the seasonality of SSS associated with the monsoon, in particular the extent of the surface freshwater plumes (SSS $<$ 31 psu) associated with the river discharge in the Bay of Bengal. Riverine runoff in the Bay of Bengal is lowest during the dry winter monsoon and spring intermonsoon, and peaks during the summer monsoon and early fall intermonsoon, with discharges up to 1.5×10^5 m^3 s^{-1} in the Ganges-Brahmaputra river system and 0.4×10^5 m^3 s^{-1} in the Irrawaddy-Sittang river systems for which we have observed time-series (Fig. 8g and h). The runoff product used to force the model reproduces the seasonality of the Ganges-Brahmaputra and the Irrawaddy-Sittang river systems (GloFAS was modified based on runoff observations in this system; see Sect. 2.2.3). As a result, the observed and simulated freshwater plumes are confined to the river mouths in late spring when runoff is lowest (April), and extend 200 to 500 km offshore in summer when runoff peaks (August), before being stretched out alongshore in the northern and western Bay of Bengal by horizontal transport in fall and winter (December; Fig. 8c). The seasonality of SSS and the impact of river discharge are more limited in the Arabian Sea. The GloFAS runoff product captures the discharge of one of the main river systems for which we have direct observations, i.e., the Narmada-Tapti rivers, with simulated values of 86.95 km^3 yr^{-1} compared to 75.31 km^3 yr^{-1} reported by Krishna et al. (2016), and MOM6-COBALT-IND12 reproduces the range of salinity observed on the shelf at the river mouth (Fig. 8a–f).

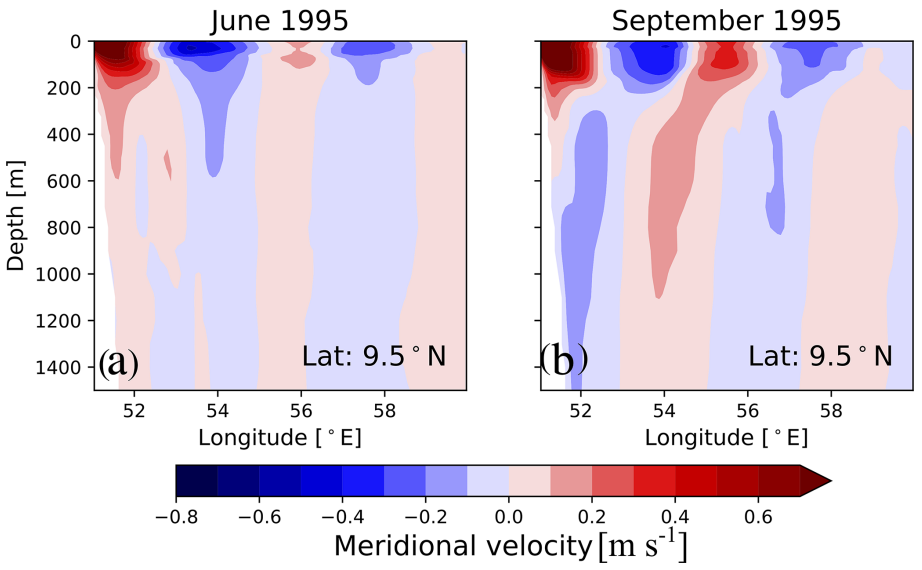

Figure 6. West-east depth section of meridional velocities across the Great Whirl in **(a)** June and **(b)** September 1995 in the MOM6-COBALT-IND12. These sections are comparable to observations from Beal and Donohue (2013) (see their Fig. 2). Positive velocities are northward.

4.5 Seasonal plankton bloom dynamics

The northern Indian Ocean is characterized by two blooming seasons associated with the summer and winter monsoons that can be identified from surface chlorophyll (Chl $> 0.5\,\mathrm{mg\,m^{-3}}$; Fig. 9a–e; e.g., Lévy et al., 2007). In the Arabian Sea, MOM6-COBALT-IND12 simulates the winter bloom (Fig. 9a–c), which develops in response to nutrient supply by convective mixing (MLD of 40–80 m; Fig. 4) and eddy vertical turbulent transport (Resplandy et al., 2011); it also simulates the summer bloom (Fig. 9d–f) associated with the western and eastern Arabian Sea coastal upwelling systems (Oman, Yemen, Somalia, southwest India; see Sect. 4.3) and a combination of horizontal and vertical eddy turbulent transport that supply nutrients to the central Arabian Sea (Resplandy et al., 2011). In the Bay of Bengal, the persistently low surface chlorophyll and its weak seasonality primarily result from strong salinity-driven stratification, which suppresses vertical nutrient supply to the mixed layer year-round (Sarma and Aswanikumar, 1991). Additionally, the presence of a subsurface chlorophyll maximum confines most primary production below the mixed layer, further reducing surface chlorophyll levels and attenuating their seasonal variability (Sarma and Aswanikumar, 1991). The model also simulates the subsurface chlorophyll maximum captured by Argo floats in both the Arabian Sea and Bay of Bengal, with RMSE values over the vertical ranging from 0.03 to $0.3\,\mathrm{mg\,m^{-3}}$ (Fig. A5). This suggests that the model effectively represents the vertical distribution of plankton and associated subsurface biological dynamics. Overall, comparison of our model's mean bias and RMSE with values reported in previous studies suggests that our chlorophyll simulation performance falls within the median range relative to other regional biogeochemical models (Chakraborty et al., 2023; Gutknecht et al., 2016; Sunanda et al., 2024).

The model overestimates surface chlorophyll concentrations by $+0.25$ to $+0.75\,\mathrm{mg\,m^{-3}}$ offshore of the western boundary currents (along Somalia, Kenya, Tanzania, and Oman) and in the southern Bay of Bengal (Fig. 9c–f). Such discrepancies might be partly attributable to uncertainties in model chlorophyll estimates arising from photoacclimation, which modulates cellular pigment content under varying light conditions (Stock et al., 2025) and/or biases in satellite-derived chlorophyll, which can differ from in-situ measurements by up to a factor of two and exhibit regional biases, especially in coastal areas (Dierssen, 2010; Sathyendranath et al., 2019; Schofield et al., 2004). Importantly, we find here that this model-satellite discrepancy has limited impact on biogeochemical fluxes. Specifically, the model captures relatively well the observed integrated primary productivity and seasonality obtained from both available *in-situ* sampling (351 stations) and satellite-based products in all regions, in particular those of the CbPM satellite primary productivity product, which is in better agreement with *in-situ* observations than the other satellite products (see Fig. 10 and Kalita and Lotliker, 2023, for an evaluation of the different products). The model captures the magnitude of the double bloom productivity in the central and western Arabian Sea (about 1000–1500 $\mathrm{mg\,C\,m^{-2}\,d^{-1}}$ in Fig. 10a, b and e), as well as the lower productivity observed in the Bay of Bengal ($< 1000\,\mathrm{mg\,C\,m^{-2}\,d^{-1}}$; Fig. 10f). The model also captures the timing of the summer bloom peak in productivity in the eastern Arabian Sea (EAS) and Somali upwelling (SOM), although the magnitude of modeled pri-

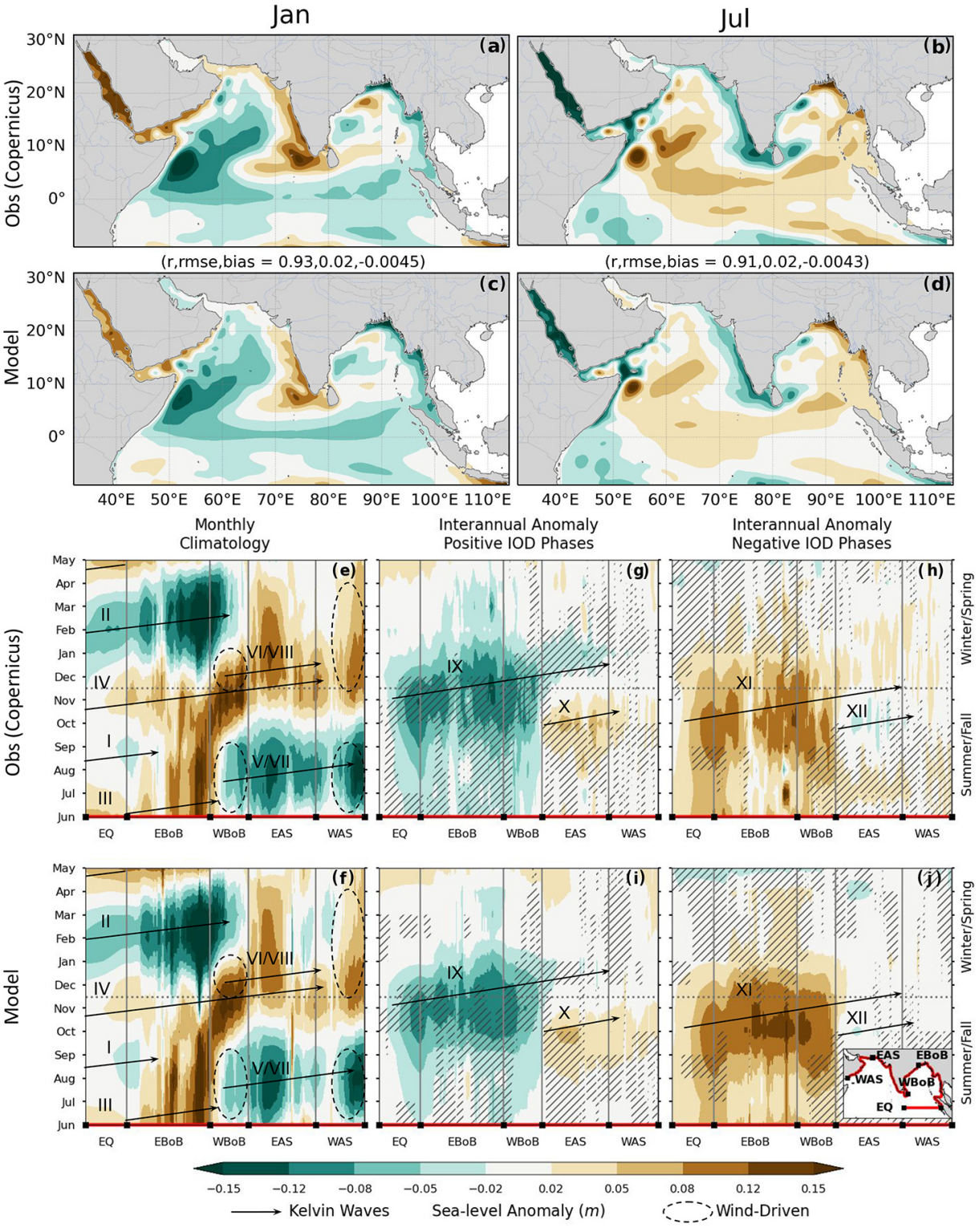

Figure 7. Coastal upwelling/downwelling inferred from sea level anomalies (SLA, in m) from satellite observations and MOM6-COBALT-IND12: **(a–d)** January and July climatological maps (1993–2020 data and model average), **(e, f)** Hovmüller of seasonal SLA (1993–2020 data and model average), and Hovmüller interannual SLA (seasonal cycle removed) for positive IOD **(g, i)** and negative IOD **(h, j)** composites. In panels **(e)**–**(j)**, the x-axis follows the equatorial and coastal wave guides (red line in inset) starting at the equator (EQ), counterclockwise around the eastern and western Bay of Bengal (EBoB/WBoB) and around the eastern and western Arabian Sea (EAS/WAS). Upwelling (negative SLA) and downwelling (positive SLA) are indicated by circles when wind-driven and by arrows when wave-driven (approximate wave speed of 2.4 m s^{-1} consistent with theoretical first baroclinic mode Kelvin waves; roman numerals used in text). Unhatched/hatched regions indicate where the IOD anomaly reinforces/opposes the seasonal signal. Satellite SLA is from Copernicus (see Table 2).

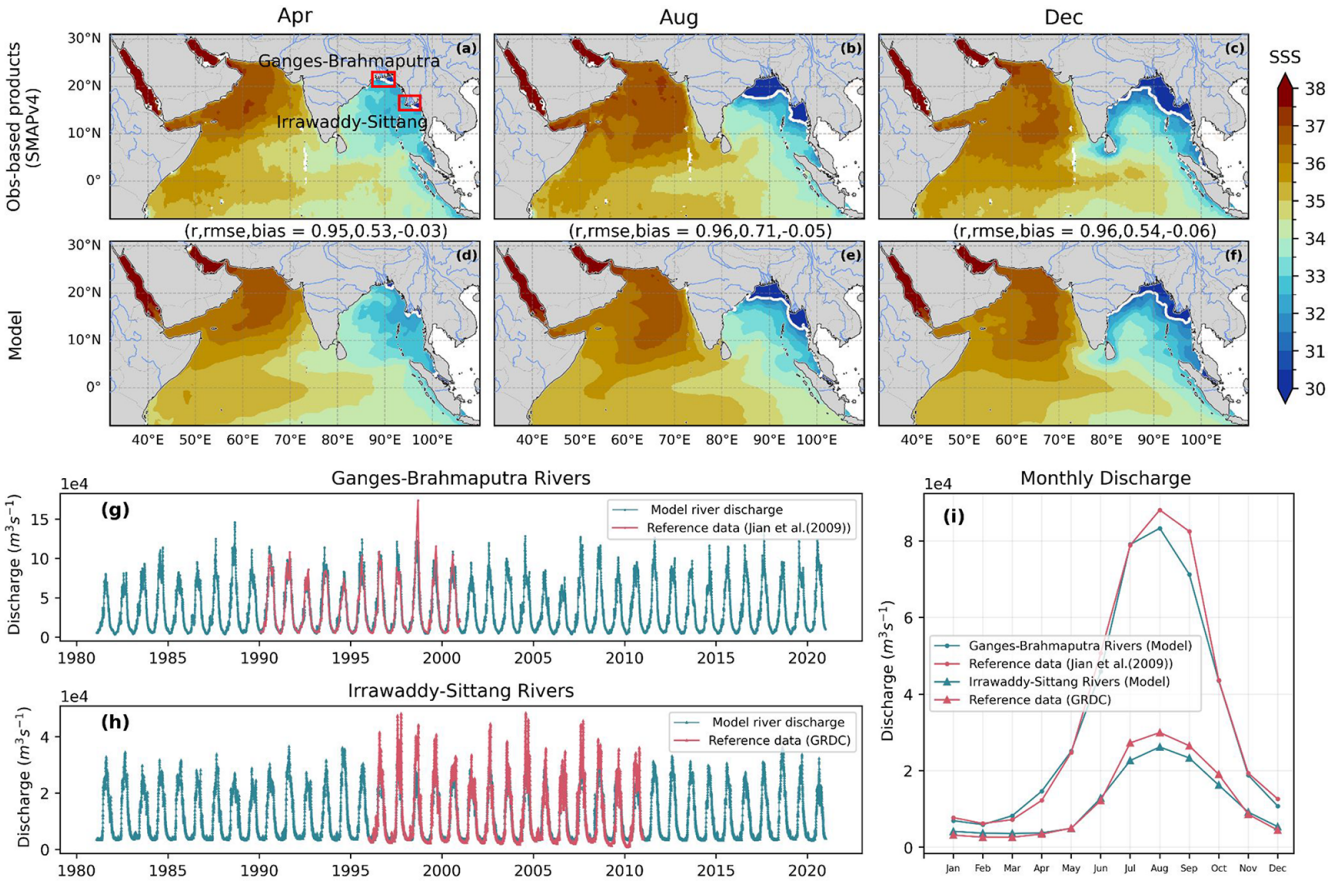

Figure 8. Seasonality in sea surface salinity (SSS) and river discharge: **(a–f)** climatological SSS in April, August and December in the satellite SMAPv4 product and MOM6-COBALT-IND12 (2015–2019 period for both). White contour delimits waters with SSS < 31 psu. **(g–i)** Water discharge from observations and the modified GloFAS runoff product used to force MOM6-COBALT-IND12: **(g)** time-series of the Ganges-Brahmaputra river system, **(h)** time-series of the Irrawaddy-Sittang river system and **(i)** seasonal climatology for both systems over the period. See Table 2 for data source. A comparison of modified GloFAS to the raw GloFAS product is presented in Fig. A1.

mary productivity might be underestimated in these regions (Fig. 10a, c and d). The fact that the model simulates the magnitude of observed primary productivity (in carbon units) but overestimates the surface chlorophyll content suggests that it might overestimate the contribution of large phytoplankton, which is characterized by a higher chlorophyll-to-carbon ratio, compared to small phytoplankton, characterized by a lower chlorophyll-to-carbon ratio. This overestimation of the contribution of large phytoplankton to the assemblage would explain the good match in primary productivity and bias in chlorophyll.

In MOM6-COBALT-IND12, the phytoplankton limitation factors vary spatially and seasonally for the three phytoplankton groups included in the model (small, large and diazotroph; Fig. 11). In the western Indian Ocean, the model simulates a strong seasonality: nitrogen and phosphorus are the most limiting nutrients in spring and early summer (March to May), but iron limitation becomes more prevalent towards the end of the summer bloom (September) and even persists in certain regions of the northern Arabian Sea until early winter (December) before it gets replenished by winter mixing (Fig. 11). This shift to iron limitation at the end of the summer monsoon is consistent with *in-situ* observations revealing a high-nutrient, low chlorophyll regime where phytoplankton growth is limited by iron in the Arabian Sea (Measures and Vink, 1999; Naqvi et al., 2010; Moffett et al., 2015; Moffett and Landry, 2020). We note, however, that during these periods of iron limitation, growth is weakly limited by nutrients (see total nutrient limitation values > 0.5 in western and nothern Arabian Sea in September and December in Fig. A6). In the eastern Indian Ocean, the seasonality is weaker and phytoplankton are generally limited by macronutrients (nitrogen and/or phosphorus), except in the northern Bay of Bengal where iron limitation becomes more important near river mouths that supply macronutrients in excess compared to iron (Fig. 11). We note that the strong iron limitation near river mouths might be partly attributed to the way iron limitation is formulated in COBALTv2. Indeed, iron limitation depends on a cell quota (rather than the ambient nutrient concentration used for macro-nutrient limita-

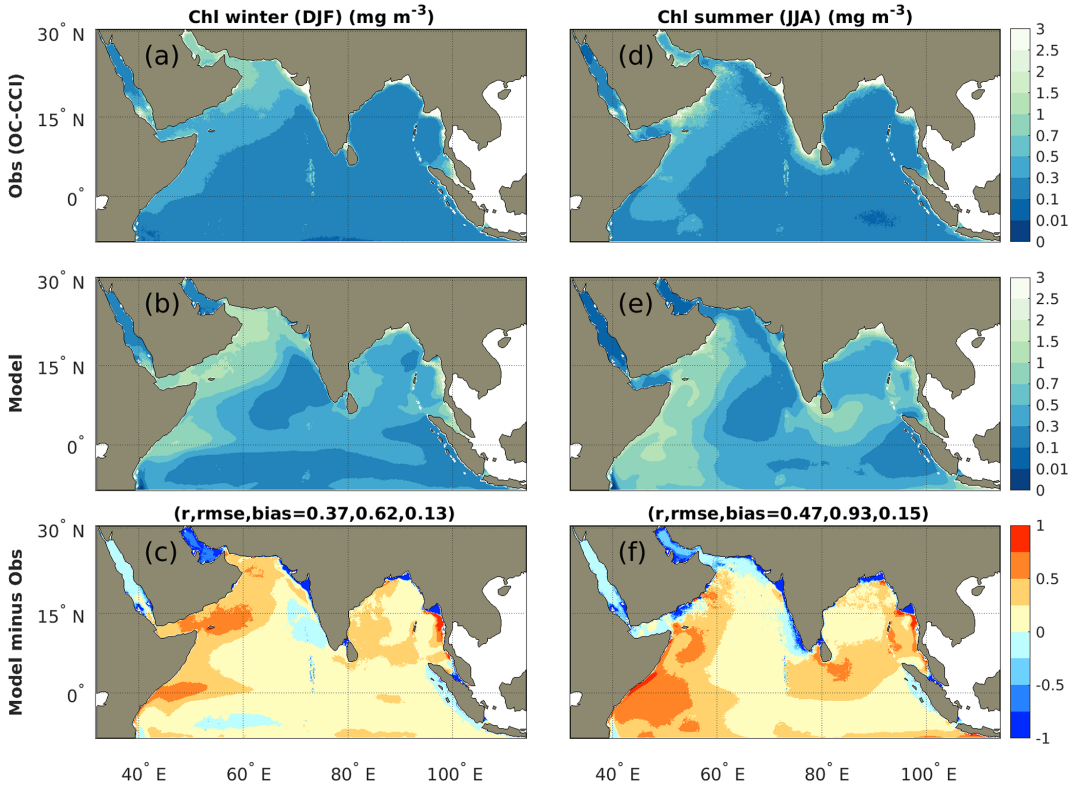

Figure 9. Sea surface chlorophyll during **(a–c)** winter (December–February) and **(d–f)** summer (June–August) monsoons. Panels **(a, d)** show satellite observations, **(b, e)** show MOM6-COBALT-IND12 model and **(c, f)** show differences between model results and observations. Correlation coefficients r, RMSE and bias between the observed and model annual means are indicated. Chlorophyll observations are from OC-CCI satellite (see details in Table 2). Model results are averaged over the 1980–2020 period.

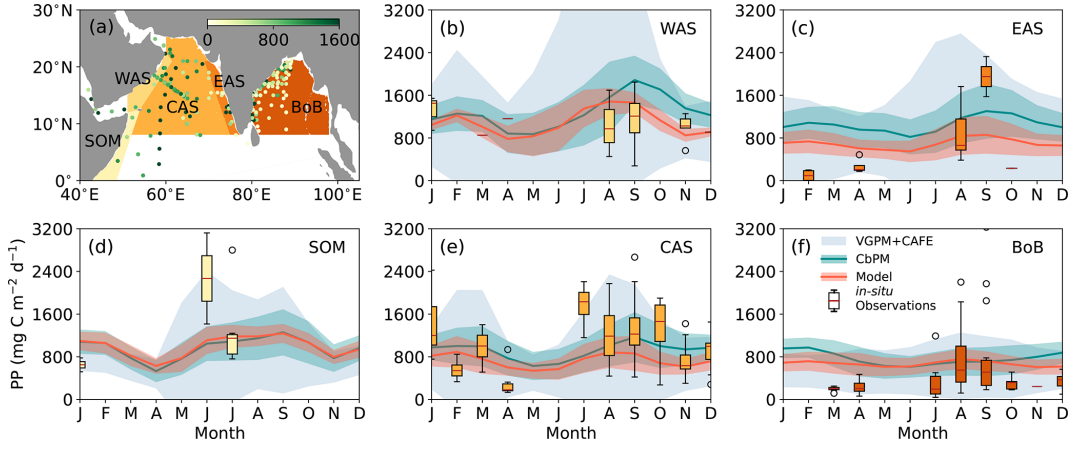

Figure 10. Seasonality in integrated primary productivity (PP). **(a)** Maps of regions used to compare observation-based and modeled PP, showing *in-situ* observation sites with PP values in green (in mg C m^{-2} d^{-1}), **(b–f)** monthly climatology of PP in MOM6-COBALT-IND12 model (regional mean $\pm 1\sigma$ in dark orange), from available in-situ observations in each region (boxplots showing median, interquartile, range and outliers defined as outside of 1.5 times the interquartile range), in the CbPM satellite product (regional mean $\pm 1\sigma$ in cyan) which performs best in this region (Kalita and Lotliker, 2023), and three additional satellite products ($\pm 1\sigma$ range of Standard-VGPM, Eppley-VGPM and CAFE in light blue). Regions are the western Arabian Sea (WAS), eastern Arabian Sea (EAS), Somalia coast (SOM), central Arabian Sea (CAS) and Bay of Bengal (BoB). Satellite and *in-situ* sampling observations are detailed in Table 2. Model and satellite-based climatologies are for the available observation period of 2003–2020.

tions), which requires time to establish near the river mouths. Yet, we note that the overall pattern of limitation simulated in the Bay of Bengal is consistent with incubation experiments showing a strong limitation by macronutrients in the southeastern Indian Ocean and co-limitations between macronutrients and iron in the Bay of Bengal (Twining et al., 2019).

5 Ocean interior, ventilation pathways and oxygen minimum zones

5.1 Ocean vertical structure and thermocline ventilation pathways

Observed subsurface temperature and salinity (300 to 700 m average) reveal the signature of the main water masses that ventilate the thermocline in the Indian Ocean (Fig. 12a and d). The Red Sea and Persian Gulf overflows contribute warm and salty waters ($> 13\,^{\circ}$C and > 35.6 psu) to the Gulf of Aden and Gulf of Oman in the Arabian Sea, respectively (You and Tomczak, 1993). In contrast, the Indonesian Throughflow (ITF) and the water masses formed in the southern subtropical and subpolar regions (e.g., mode waters and central waters) contribute relatively cold and fresh subsurface waters ($< 8\,^{\circ}$C and < 35 psu) in the south of the domain, before being mixed and transported westward by the Southern Equatorial Current system and flowing northward and crossing the Equator along the African continent (You, 1997; Schott et al., 2004; Sprintall et al., 2009; McCreary et al., 2013; Nagura and McPhaden, 2018). Finally, intermediate temperature and salinity in the Bay of Bengal (about 10°C and 35 psu) arise from the relatively weak thermocline ventilation, mostly maintained by the eastward transport from the Arabian Sea and Equatorial region.

MOM6-COBALT-IND12 reproduces the observed patterns in subsurface temperature and salinity in most of the basin (correlation coefficient $r > 0.99$ and RMSE of 0.33 °C and 0.07 psu). Specifically, the model simulates the contrast between the warm and salty waters in the northeastern Arabian Sea, the cold and freshwaters along the model southern boundary, and the waters with intermediate temperature and salinity in the Bay of Bengal (Fig. 12). The largest departures are found in the northern Arabian Sea where the model is biased cold and fresh (local bias between -0.8 and $-0.3\,^{\circ}$C and -0.4 to -0.1 psu; Fig. 12), suggesting that the Persian Gulf overflow is not as well simulated as other pathways.

We further examine ventilation pathways using vertical sections in the eastern Indian Ocean, the Gulf of Oman and the Arabian Sea (Figs. 13 and 14). In the eastern Indian Ocean (at 90° E), the model reproduces the observed vertical structure, including the intermediate salinity found in the subsurface Bay of Bengal and the influence of fresher ITF waters in the southern part of the domain (at ~ 1000 m depth and latitudes $< 5°$ S; Fig. 13). We note that the model only extends to 8° S, and therefore does not fully resolve the ITF centered at 5–10°S nor the Southern Equatorial Current at 10–20° S, but receives contributions from ITF waters and southern waters through the open boundary. The model presents, a slight bias in the vertical structure of the Bay of Bengal, with slightly colder and fresher near-surface waters and slightly warmer and saltier subsurface waters with a small influence on the stratification in the region (Fig. 13c and f).

In the Gulf of Oman, observations show the plume of salty and warm Red Sea overflow waters (RSOW) that flow into the Gulf of Aden at a depth of 400–1000 m ($> 12\,^{\circ}$C and > 36 psu; Fig. 14a and d). The model simulates the depth range of the plume but the lower part of the plume is biased salty and warm (local bias of 1 to 2 °C and 0.2 to 0.8 psu; Fig. 14). This bias in the RSOW plume could come from biases in the source waters that overflow at the Bab-El-Mandeb Strait upstream, or from the misrepresentation of the plume mixing along the pathway. At the Bab-El-Mandeb Strait, we find that the model simulates remarkably well the volume transport of the three water masses flowing in and out of the Red Sea (Fig. 15a). Specifically, the model simulates the observed outflow of RSOW that peaks in winter and drastically slows down in summer, the reversal of surface waters flowing into the Red Sea in winter and out of the Red Sea in summer, as well as the inflow of Gulf of Aden intermediate waters (GAIW) that only takes place in summer. The model, however, shows a bias in the density of these water masses, particularly in summer when simulated RSOW are lighter and surface waters (and to some extent GAIW, although observations are sparse) are denser than observed (Fig. 15b). This suggests there is insufficient mixing between the RSOW plume waters and the lighter (colder/fresher) waters above. This hypothesis is also supported by the structure of the temperature and salinity biases along the depth section showing a dipole of too salty/too warm waters in the lower part of the plume (800–1000 m depth) and slightly too fresh/too cold waters in the upper part of the plume (400–800 m depth; Fig. 14c and f). This bias is, however, confined to the plume in the Gulf of Aden, and seems to have a relatively small influence on the vertical structure further downstream, explaining the good agreement in subsurface temperature and salinity in the southwestern Arabian Sea (Fig. 12).

In the northern Arabian Sea, observations show that Persian Gulf waters (PGW) flow into the Arabian Sea at about 200–400 m depth (Fig. 14). In MOM6-COBALT-IND12, however, PGW are too warm, too light and therefore enter the northern Arabian Sea at a too shallow depths of 100–200 m, leading to a cold/fresh bias at 200–400 m depth where PGW are located in observations and a warm-salty bias above (Fig. 14). This trapping of the PGW close to the surface significantly changes the vertical structure of the northern Arabian Sea by reducing the stratification in the upper 200 m in the northern Arabian Sea.

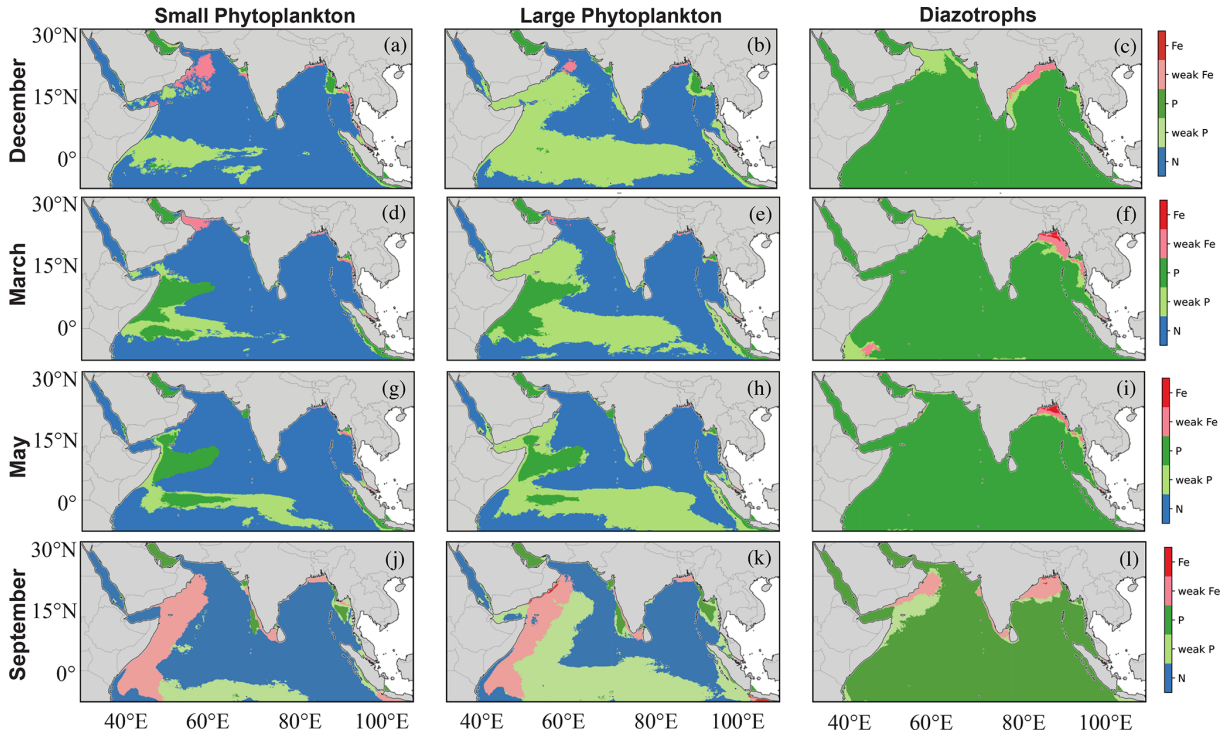

Figure 11. Climatological surface nutrient limitation (nitrogen N, phosphorus P and iron Fe) in MOM6-COBALT-IND12 for small phytoplankton, large phytoplankton and diazotrophs in December, March, May and September. Weak P (weak Fe) limitations indicate where P (Fe) is limiting but by a small amount relative to N or Fe (P) are near co-limiting (i.e., near co-limitation with difference between limitation factors < 0.25). Model climatology is based on the 1980–2020 period.

5.2 Subsurface oxygen and oxygen minimum zones

Observed subsurface oxygen concentrations show the extent of the two OMZs located in the Arabian Sea and Bay of Bengal (Fig. 16). In the Arabian Sea, averaged subsurface oxygen concentrations (300–700 m) are lower than 10 µmol kg^{-1} in most of the region and reach suboxic values (< 5 µmol kg^{-1}) around 15–20° N. In the Bay of Bengal, the OMZ is less intense with averaged subsurface concentrations of 10–20 µmol kg^{-1} and no suboxia. The equatorial subsurface is better oxygenated, but still characterized by relatively low averaged oxygen subsurface concentrations of 50–100 µmol kg^{-1} (Fig. 16). Highest concentrations are found in the southwestern part, where the western boundary current supplies oxygen originating from the Southern Gyre and ITF (transported via the South Equatorial Current).

The MOM6-COBALT-IND12 model reproduces the observed large scale patterns of subsurface oxygen (basin-scale correlation coefficient $r = 0.94$ and RMSE $= 16$ µmol kg^{-1}; Fig. 16a–c). The largest biases are found in the eastern (down to -30 µmol kg^{-1}) and western (up to $+40$ µmol kg^{-1}) north equatorial band where the gradients in oxygen are strong. In this region, the model shows a high oxygen bias near the base of the thermocline (500–1000 m), coinciding with a low nitrate bias (not shown). This pattern points to either a misrepresentation of biological remineralization at depth or an inaccurate representation of the relative contribution of the water masses forming the Central Waters supplying oxygen to this region. These waters originate from a blend of the ITF waters and southern-sourced Mode Waters. Previous studies have demonstrated that oxygen distribution in this region is highly sensitive to the relative contribution between these two sources (Ditkovsky et al., 2023). However, the scarcity of direct observations in this region limits our ability to conclusively attribute the model bias to either mechanism.

Yet, the most biogeochemically relevant bias is probably the overestimation of the extent and intensity of suboxic conditions in the northern Bay of Bengal, where the local difference in modeled versus observed oxygen concentration ranges from -20 to -10 µmol kg^{-1}, reflecting a much larger extent of suboxia in the model than in observations (Fig. 16a–c). We evaluate the model ability to reproduce the volume of the OMZ as a function of the oxygen threshold chosen to define its boundary (i.e., volume bounded by oxygen concentrations from 5 to 150 µmol kg^{-1}, Fig. 16d–f). At the basin scale, MOM6-COBALT-IND12 reproduces relatively well the observed OMZ volumes defined by thresholds above 30 µmol kg^{-1}, in particular the volume of hypoxic waters delimited by 60 µmol kg^{-1} (approximately 1×10^{16} m^3) and the volume of low oxygenated wa-

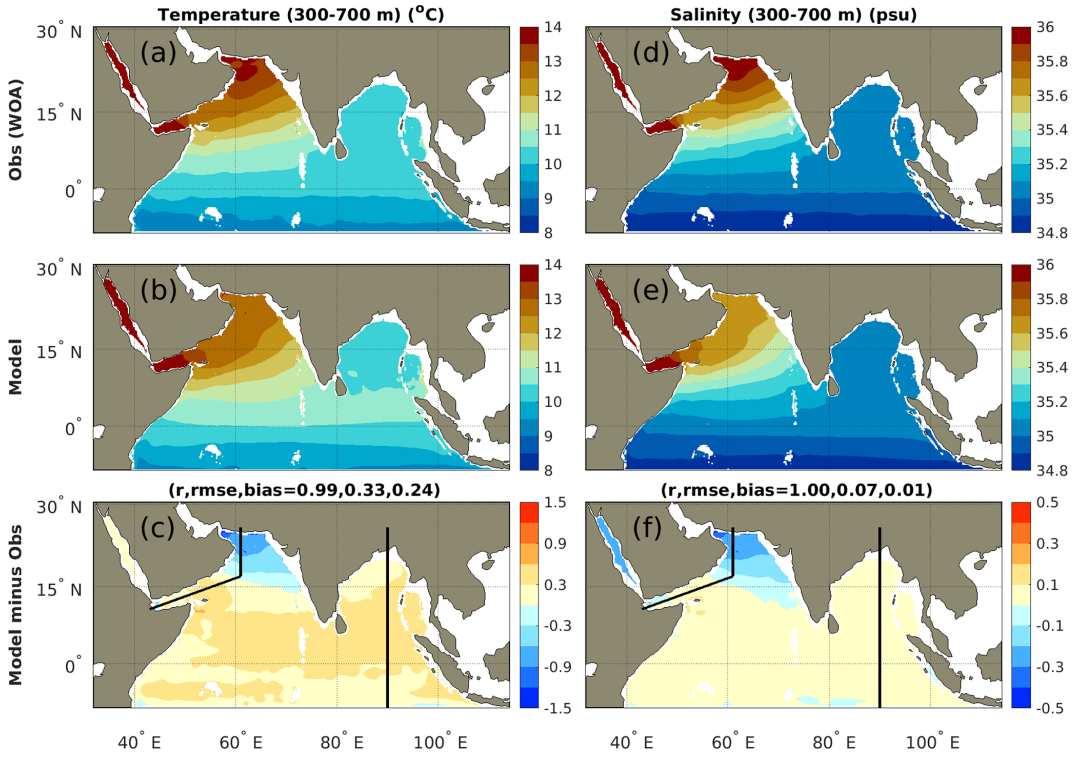

Figure 12. Annual mean subsurface (300–700 m depth) temperature and salinity in **(a, d)** observations, **(b, e)** MOM6-COBALT-IND12 model and **(c, f)** differences between model results and observations. Correlation coefficients r, RMSE and bias between the observed and model annual means are indicated. Temperature and salinity observations are from WOA18. Model results are averaged over the 1980–2020 period. Black lines indicate depth sections shown in Figs. 13 and 14.

ters delimited by 100 µmol kg^{-1} (approximately 2×10^{16} m^3; Fig. 16d). In contrast, the model overestimates the volume of suboxic waters delimited by 5 µmol kg^{-1} (0.17×10^{16} m^3 vs. 0.06×10^{16} m^3 in Bianchi et al. (2012) observations), mostly because of the large suboxic volume simulated in the Bay of Bengal (0.10×10^{16} m^3 vs. 0.00×10^{16} m^3 in observations; Fig. 16f). Meanwhile, the volume of suboxic waters in the Arabian Sea is well represented (0.07×10^{16} m^3 vs. 0.06×10^{16} m^3). Finally, we note that the good match between observed and modeled hypoxic volumes is favored by the partial compensation of small biases in the Arabian Sea (model volume about 0.14×10^{16} m^3 lower than in observations) and the Bay of Bengal (model volume about 0.06×10^{16} m^3 higher than in observations; Fig. 16e–f).

6 Intraseasonal variability

We quantify the intraseasonal variability (ISV) in the surface ocean circulation using the intraseasonal standard deviation of the sea level anomaly (see Sect. 3.2). This diagnostic captures variability linked to all dynamical processes varying on intraseasonal time-scales, which includes mesoscale eddies and filaments, as well as meandering jets and planetary waves (Rossby and Kelvin waves). These intraseasonally varying features are key to the transport and mixing of physical and biogeochemical tracers, such as nutrients and oxygen, and to the onset and spatial extent of the seasonal phytoplankton blooms in the Indian Ocean (e.g., Resplandy et al., 2011, 2012; Lachkar et al., 2016; Rixen et al., 2020; Pearson et al., 2022; Vinayachandran et al., 2021)

Satellite observations show two hotspots where the intraseasonal variability in SLA exceeds 5 cm and can reach values higher than 10 cm (Fig. 17a). The first hotspot is in the western Arabian Sea offshore Somalia and the Arabian Peninsula, where the high energy dynamics of the western boundary current and the presence of upwelling systems and complex coastal topography (capes/headland) promote the formation of large mesoscale eddies such as the Great Whirl and Socotra Eddy (see Sect. 4.2), and filaments extending from the Arabian Peninsula into the central Arabian Sea (e.g., Beal and Donohue, 2013; Resplandy et al., 2011; Brandt et al., 2003; Wang et al., 2018). The second hotspot covers the central and western Bay of Bengal and extends south of Sri Lanka, and has been attributed to mesoscale eddies and Rossby waves generated in the coastal eastern Bay of Bengal that propagate westward into the central and western Bay of Bengal (Sengupta et al., 2001, 2007; Cheng et al., 2013). MOM6-COBALT-IND12 simulates the locations of the two hotspots of highest ISV in the western Arabian Sea and west-

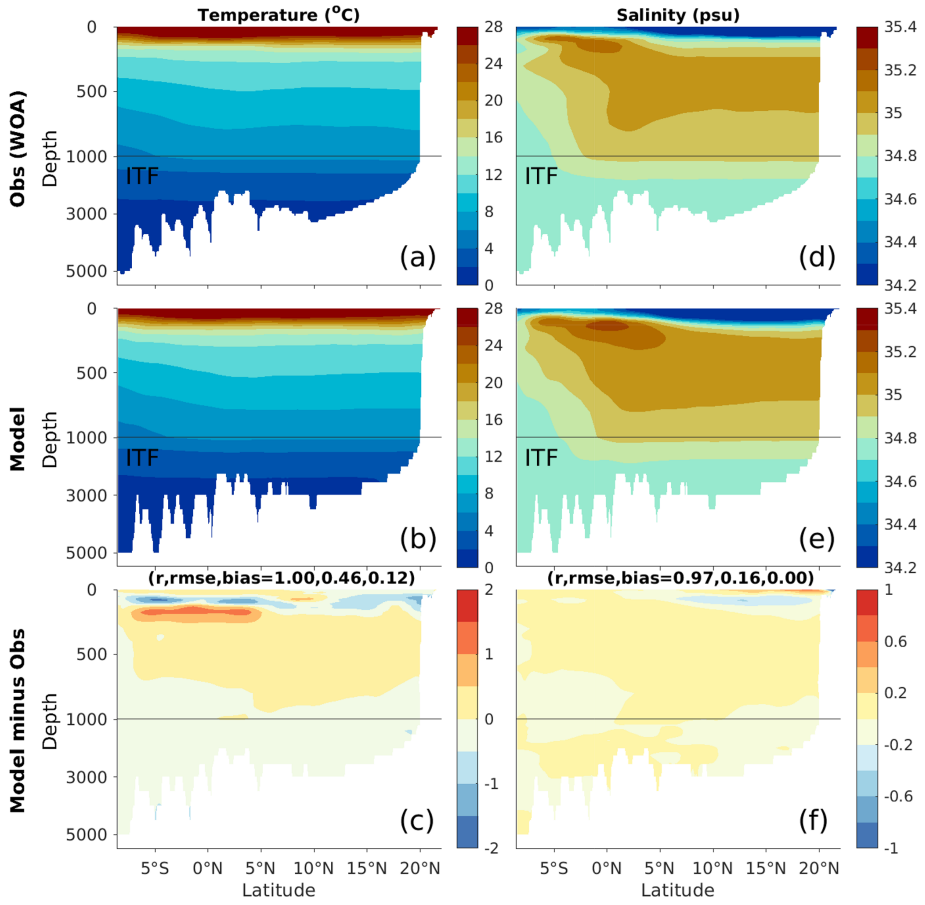

Figure 13. Depth section of annual mean temperature and salinity at 90° E in **(a, d)** observations, **(b, e)** MOM6-COBALT-IND12 model and **(c, f)** differences between model results and observations. Correlation coefficients r, RMSE and bias between the observed and model annual means are indicated. See location of section on Fig. 12. Temperature and salinity observations are from the WOA18 (Table 2). Model results are averaged over the 1980–2020 period. Indonesian Througflow waters (ITF) are indicated.

ern Bay of Bengal, but the amplitude tends to be weaker than observed, with typical values of 3–8 cm in the model versus 4–12 cm in the observations (Fig. 17).

Other regions of relatively high observed ISV (> 3 cm) include the mouths of major rivers, such as the Ganges-Brahmaputra, Irrawaddy-Sittang and Narmada-Tapti river systems (see Figure 1 for rivers location), coastal ocean waters along the eastern Bay of Bengal and eastern Arabian Sea, and the 5–10° N band in both the Arabian Sea and Bay of Bengal (Fig. 17). ISV at the river mouths and the coastal ocean can largely be attributed to the ISV in river freshwater discharge (up to 50 % of seasonal variability amplitude for the Ganges, for instance; Jian et al., 2009), tidal forcing and the propagation of coastal Kelvin waves (e.g., Nienhaus et al., 2012). MOM6-COBALT-IND12 reproduces relatively well the observed ISV in the coastal ocean and part of the ISV at river mouths.

Finally, the intraseasonal variability in the 5–10° N band, which reaches 3 to 5 cm in the satellite-based estimate in response to the westward propagation of Rossby waves (Bruce et al., 1994; Shankar and Shetye, 1997; Vialard et al., 2009; Cheng et al., 2017), is also underestimated in the model (1–3 cm; Fig. 17). These underestimations might indicate the current spatial resolution of the model (1/12°) may still be insufficient for resolving these processes.

Figure 18 illustrates the influence of eddies and filaments on surface chlorophyll and phytoplankton production and their seasonality in the Arabian Sea, specifically in the first hotspot of ISV described above (western Arabian Sea and central Arabian Sea). The model reproduces the fine-scale features structuring the winter and summer blooms. During the winter monsoon, fine-scale eddies (∼ 20–50 km in diameter) shape the bloom occurring in the northern and central Arabian Sea (Fig. 18a, b, e and f). This is consistent with the results of Resplandy et al. (2011), which showed that these fine-scale eddies sustain the bloom by vertically transporting nutrients to the euphotic zone during early winter and by locally re-stratifying and alleviating light limitation during late winter when convection occurs (see Sect. 4.2 and Fig. 4 for mixed layer seasonality). During the summer mon-

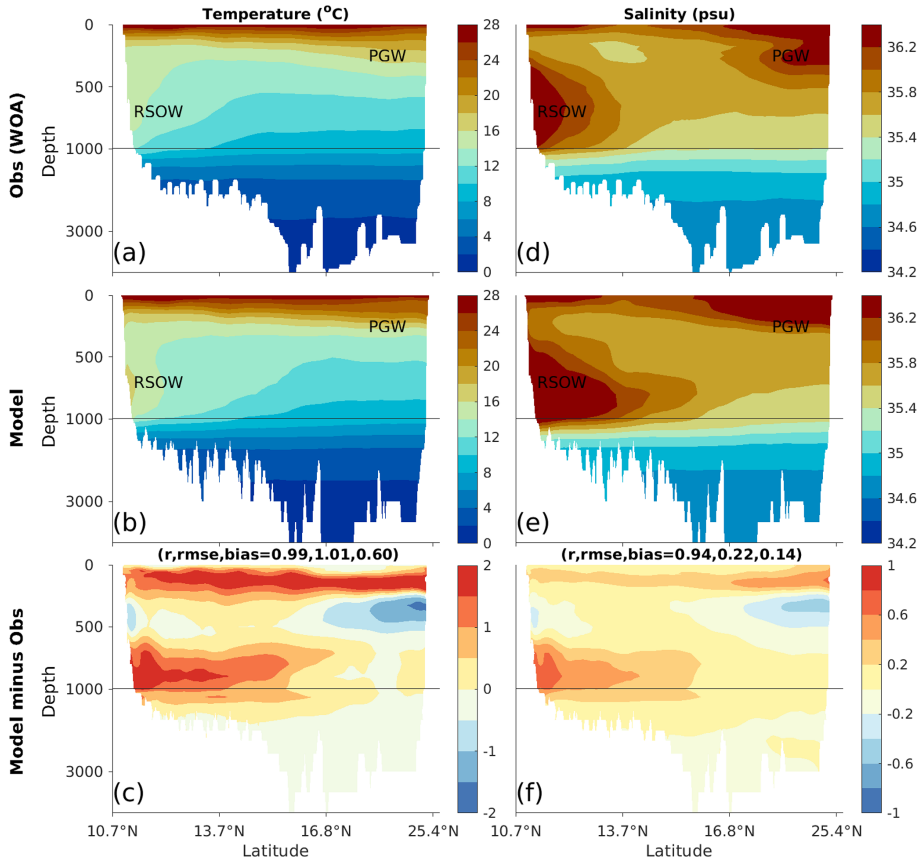

Figure 14. Depth section of annual mean temperature and salinity in the Gulf of Oman (southwest to northeast) and the Arabian Sea (south-north at 61° E) in **(a, d)** observations, **(b, e)** MOM6-COBALT-IND12 model and **(c, f)** differences between model results and observations. See location of section on Fig. 12. Correlation coefficients r, RMSE and bias between the observed and model annual means are indicated. Temperature and salinity observations are from the WOA18 (Table 2). Model results are averaged over the 1980–2020 period. Persian Gulf Waters (PGW) and Red Sea Overflow Waters (RSOW) are indicated.

soon, surface chlorophyll is highest in the coastal upwelling regions of Oman and Somalia in the early phase of the bloom (Fig. 18c and g) and then extends offshore in long filaments wrapped around mesoscale eddies in the central Arabian Sea and around the Great Whirl in the late phase of the bloom (Fig. 18d and h). The structure of the bloom here is also consistent with the findings of Resplandy et al. (2011), which showed that eddy-induced vertical transport supplied most of the nutrients in coastal waters during the early stage of the summer upwelling, while horizontal transport by filaments supplied nutrients to the central Arabian Sea. We note that the shape of the winter and summer eddies and filaments is well captured by the model, although their exact location might not be the same. Indeed, we expect the model to reproduce the statistics of mesoscale structures (e.g., eddies and filaments) for a given season and region, but not necessarily their exact position. We also note that simulated surface chlorophyll concentrations are biased high in the model, in particular during the late summer monsoon (Fig. 18d and h). This is in line with the finding that chlorophyll is overestimated in the model, although primary productivity appears to be well simulated, likely due to the high contribution of large phytoplankton with high chlorophyll-to-carbon ratio (see Sect. 4.5 and Figs. 9 and 10).

7 Interannual Indian Ocean dipole

The model reproduces the amplitude and zonal pattern of SST changes expected in response to the Interannual IOD ($r > 0.9$; Fig. 19b–e; see Fig. 19a for timing of positive and negative IOD phases). This includes the strong SST response in the eastern equatorial Indian Ocean, offshore Java and Sumatra, where the surface cools by -0.5 to -1 °C during positive IODs and warms by $+0.5$ to $+1$ °C during negative IODs, as well as the weaker response in the eastern and central equatorial Indian Ocean, where the ocean surface warms by $+0.2$ to $+0.5$ °C during positive IODs and cools by -0.2 to -0.5 °C during negative IODs. This SST signature of IODs is associated with anomalous winds and changes in thermocline depth along the equator (Saji et al., 1999; Web-

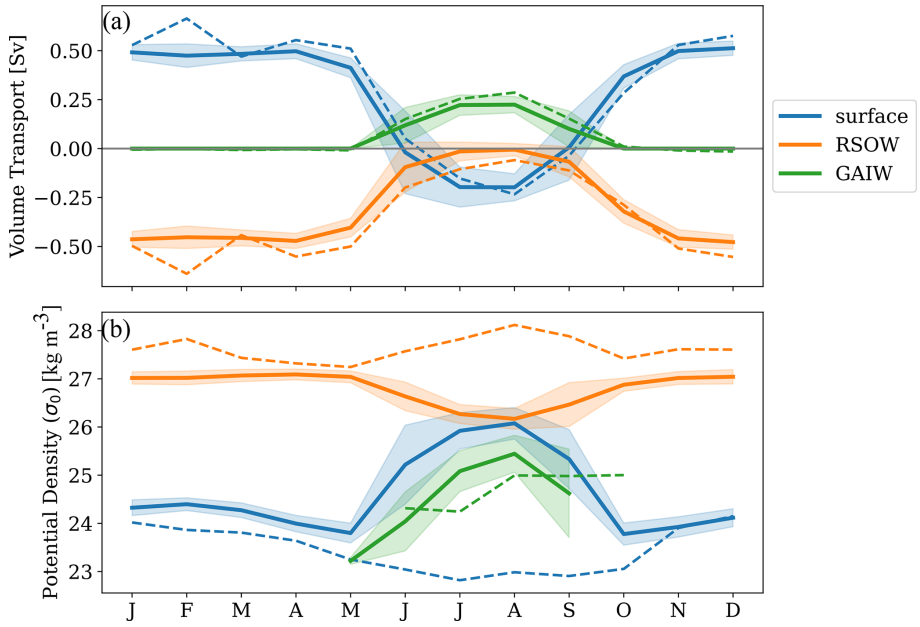

Figure 15. Seasonal evolution of the **(a)** volume transport and **(b)** potential density at the Bab-El-Mandeb Strait (between the Red Sea and the Gulf of Aden) in observations (dashed) and the model (solid). The three water masses are surface waters, Gulf of Aden Intermediate Waters (GAIW) and Red Sea Outflow Waters (RSOW). Observations and water mass detection method using flow direction are from Sofianos et al. (2002, see Table 2). Positive transport is into the Red Sea, negative transport into the Gulf of Aden. Model is averaged over 1980–2020. See details on water masses in Sect. 3.1.

ster et al., 1999; Currie et al., 2013). During positive IODs, easterly wind anomalies in the central Indian Ocean shallow the thermocline in the east and generate anomalously cold eastern SSTs. In the west these wind anomalies, in conjunction with Rossby waves, deepen the thermocline and produce anomalously warm western SSTs. During negative IODs, anomalous westerly winds lead to the opposite east/west pattern in SST and thermocline depth. These SST signatures develop in boreal summer, peak in fall, and decay through winter.

Figure 20 focuses on this zonal contrast introduced by the IOD, through a comparison of observed and modeled interannual anomalies in SST and thermocline depth at two equatorial Indian Ocean sites: one eastern mooring offshore Sumatra (95° E, 5° S) and one western mooring in the Seychelles-Chagos thermocline ridge (57° E, 4° S). We use observations from the *in-situ* RAMA that we complement with OISST data and Argo float-based thermocline depth (see Table 2). MOM6-COBALT-IND12 reproduces particularly well the timing and amplitude of interannual variations in SST (r of 0.78–0.90 with RAMA and 0.75–0.79 with OISST) and in thermocline depth (r of 0.75–0.82 with RAMA and 0.73–0.84 with Argo) at both RAMA stations (Fig. 20), including the asymmetry in the response between IOD phases (Hong et al., 2008b, a; Cai et al., 2013; Nakazato et al., 2021). At the eastern station, the thermocline deepens by 20–30 m and SSTs increase by +0.5 to +1 °C during negative IODs. In contrast, the thermocline only shallows by 10–20 m and SSTs generally decrease by less than −0.5 °C during positive IODs, except during the strong positive IOD of 2019 during which SSTs cooled by more than 1.5 °C in both observations and models. The model also captures interannual variations observed at the western station (Fig. 20). While IOD-driven variability is present at the western mooring, its influence is likely weaker compared to other sources of variability. Nevertheless, the model reproduces the associated variabilities, including a deeper thermocline and cooler SSTs during negative IODs, and shallower thermocline and warmer SSTs during positive IODs (Fig. 20).

The wind anomalies associated with the IOD also produce equatorially trapped Kelvin waves that travel east towards Sumatra and Java, impinge on their coasts and continue traveling counterclockwise around the rim of the northern Indian Ocean, thereby modulating the seasonal upwelling/downwelling motions described in Sect. 4.3 above (see details on coastal Kelvin wave modulation by IOD in Aparna et al., 2012; Suresh et al., 2018; Pearson et al., 2022). As shown in Fig. 7, the model reproduces the coastal SLA interannual anomalies associated with IOD phases. In particular, it simulates the upwelling anomaly observed between September and January during positive IOD phases along the coasts of the Bay of Bengal (arrows for waves IX and X; SLA internanual anomalies of −12 to −5 cm), and the downwelling anomaly observed during negative IOD phases (arrows for waves XI and XII, same months; SLA internanual anomalies of +5 to +12 cm; Fig. 7). The model also simulates the

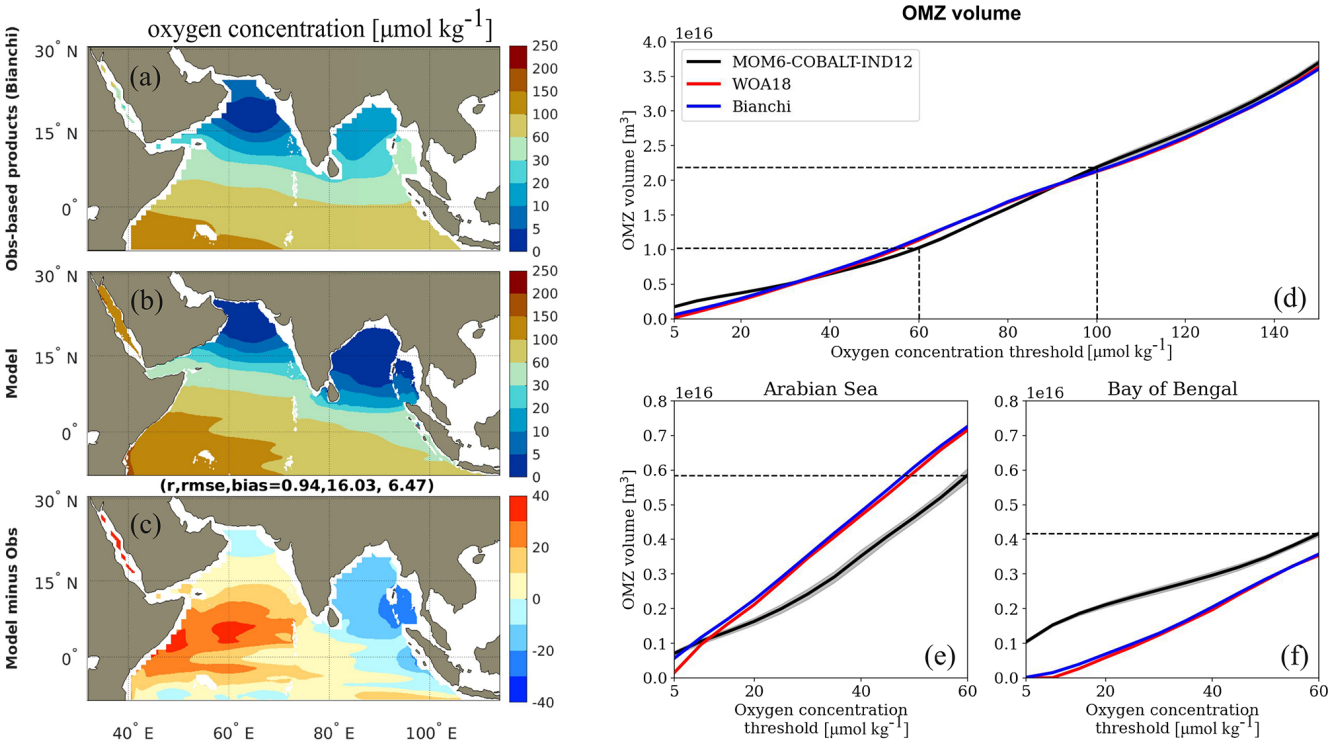

Figure 16. **(a–c)** Annual mean subsurface (300–700 m depth) oxygen concentrations in observations (a, Bianchi et al., 2012), MOM6-COBALT-IND12 **(b)** and differences between model results and observations **(c)**. Correlation coefficients r, RMSE and bias between the observed and model annual means are indicated. **(d–f)** Observed and simulated ocean volume within a certain oxygen concentration threshold in the model domain **(d)**, the Arabian Sea and the Bay of Bengal **(e–f)**. Observations from Bianchi et al. (2012, in blue) and WOA18 (in red) differ mostly on the volume at low oxygen values. Grey shading indicates the 1σ model interannual variability. Model results are for the 1980–2020 period.

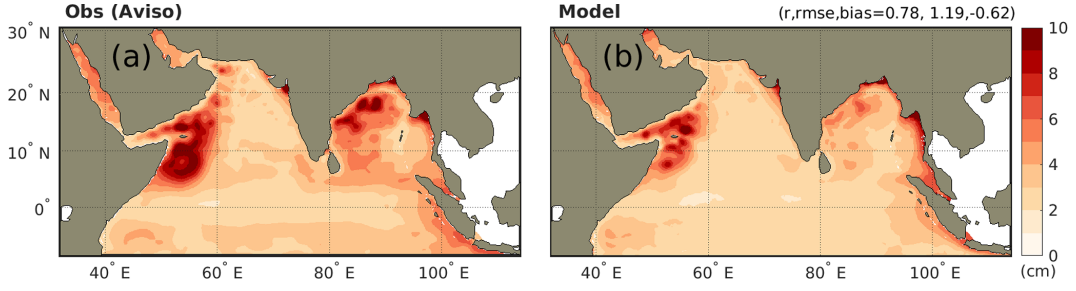

Figure 17. Intraseasonal variability (includes mesoscale eddy activity and wave-driven variability) quantified by the intraseasonal standard deviation of the sea level anomaly (SLA) in **(a)** AVISO satellite observations and **(b)** MOM6-COBALT-IND12. SLA over the 1994–2017 period was detrended using a linear regression and filtered using a 14–120 d band-pass filter.

weaker SLA anomalies of opposite sign (compared to the Bay of Bengal) observed along the coasts of the Arabian Sea (SLA interannual downwelling anomaly of +2 to +5 cm during positive IODs, and upwelling anomaly of −2 to 0 cm during negative IODs; Fig. 7).

IOD phases are associated with biogeochemical signatures visible at the basin scale in satellite ocean color observations (Murtugudde and Busalacchi, 1999; Wiggert et al., 2009; Currie et al., 2013). Figure 21 compares composites of integrated primary productivity anomalies from the CbPM satellite and MOM6-COBALT-IND12 in boreal fall (September–November). Negative IOD phases are characterized by negative primary productivity anomalies in the eastern equatorial Indian Ocean (−150 to −300 mg C m^{-2} d^{-1} offshore Sumatra; Fig. 21a) due to the depressed thermocline and associated nutricline and weaker upwelling-favorable wind (Fig. 20), and positive primary productivity anomalies in the western equatorial Indian Ocean (+50 to +150 mg C m^{-2} d^{-1} off-

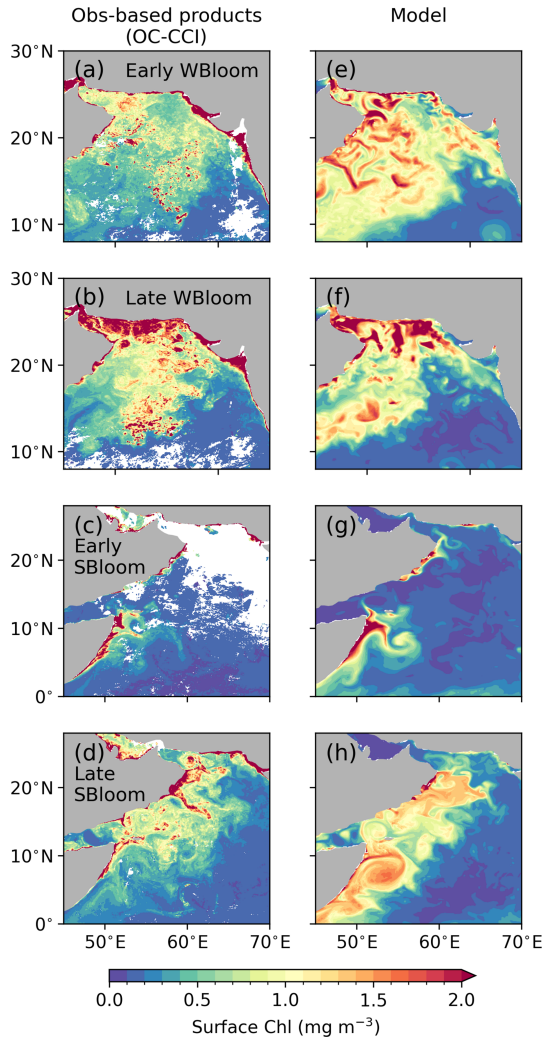

Figure 18. Fine-scale structures (eddies, filaments) revealed by surface chlorophyll in the OC-CCI satellite product **(a–d)** and the MOM6-COBALT-IND12 model **(e–h)**. Snapshots are for **(a, e)** early winter bloom (WBloom, 29 January 2014), **(b, f)** late WBloom (10 March 2014), **(c, g)** early summer bloom (SBloom, 6 June 2011) and **(d, h)** late SBloom (4 October 2011). OC-CCI images are 8 d composites and model images are 7 d averages.

shore Somalia) due to the shallower thermocline and nutricline (Fig. 20). Negative IODs are also associated with strong positive primary productivity anomalies around the tip of India ($> +200\,\mathrm{mg\,C\,m^{-2}\,d^{-1}}$) associated with the wave-driven shoaling of the thermocline and nutricline (Fig. 7) and positive anomalies in most of the Arabian Sea (Fig. 21a). The response to positive IODs mirrors the response of negative IODs in the equatorial Indian Ocean, with positive anomalies observed in the eastern equatorial Indian Ocean and negative anomalies in the western equatorial Indian Ocean and around the tip of India (Fig. 21b). We note, however, that the primary productivity anomalies in the northern and central Arabian Sea are positive during both negative and positive IOD phases. The model captures remarkably well the pattern and sign of the observed primary productivity anomalies during both negative and positive IODs (correlation coefficient $r > 0.7$), although the amplitude of the anomaly is slightly lower in the model than in the CbPM satellite product (RMSE of 60 to $80\,\mathrm{mg\,C\,m^{-2}\,d^{-1}}$, bias of -1.5 to $-10.5\,\mathrm{mg\,C\,m^{-2}\,d^{-1}}$; Fig. 21c and d). On the one hand, the model–observation discrepancy in primary productivity anomaly amplitude may stem from weak nutrient variability associated with the shallow MLD. On the other hand, the amplitude of the primary productivity anomalies obtained from satellite products remains uncertain. For instance, the primary productivity anomaly composites obtained from another satellite product (CAFE) show similar patterns but with an amplitude that is about half of the CbPM satellite product (Figs. 21a, c and A7a, c). The amplitude of the anomaly in the model sits between the two satellite products (RMSE of 60–$80\,\mathrm{mg\,C\,m^{-2}\,d^{-1}}$ in both cases and absolute bias between -10.5 and $+24\,\mathrm{mg\,C\,m^{-2}\,d^{-1}}$; see Figs. 21 and A7). Given the discrepancies among observational datasets, the model likely provides a reasonable estimate of primary productivity variability. Nevertheless, additional in situ observations are needed to more accurately constrain the true primary productivity response to the IOD.

8 Discussion and conclusions

In this study, we configured, customized, and validated a high-resolution (1/12°) regional ocean biogeochemical model (MOM6-COBALT-IND12 v1.0) for the northern Indian Ocean. Specifically, we adjusted river discharge rates and nutrient loadings in the Bay of Bengal according to observational constraints, significantly improving simulations of river plume dynamics and surface salinity. Additionally, we enhanced lithogenic particle fluxes from rivers, adjusted detritus sinking rate, and refined the parameterization of the nitrogen cycle, resulting in better representations of subsurface oxygen distributions and suboxic conditions. These improvements collectively allow the model to capture most key aspects of biogeochemical and physical processes in the northern Indian Ocean

At the basin scale, the MOM6-COBALT-IND12 model simulates the contrast between the Arabian Sea – characterized by high evaporation, inflow from the saline marginal seas (Red Sea and Persian Gulf) and high upper ocean salinity – and the Bay of Bengal – characterized by high precipitation, high river runoffs and low upper ocean salinity. On seasonal time-scales, the model captures the monsoonal reversal in ocean circulation, including the development of the Great Whirl and wind-driven summer coastal upwelling systems along the western boundary, the winter convective mixing in the northern Arabian Sea, as well as the propagation of upwelling and downwelling coastal Kelvin waves along the equatorial waveguide and the rim of the northern Indian

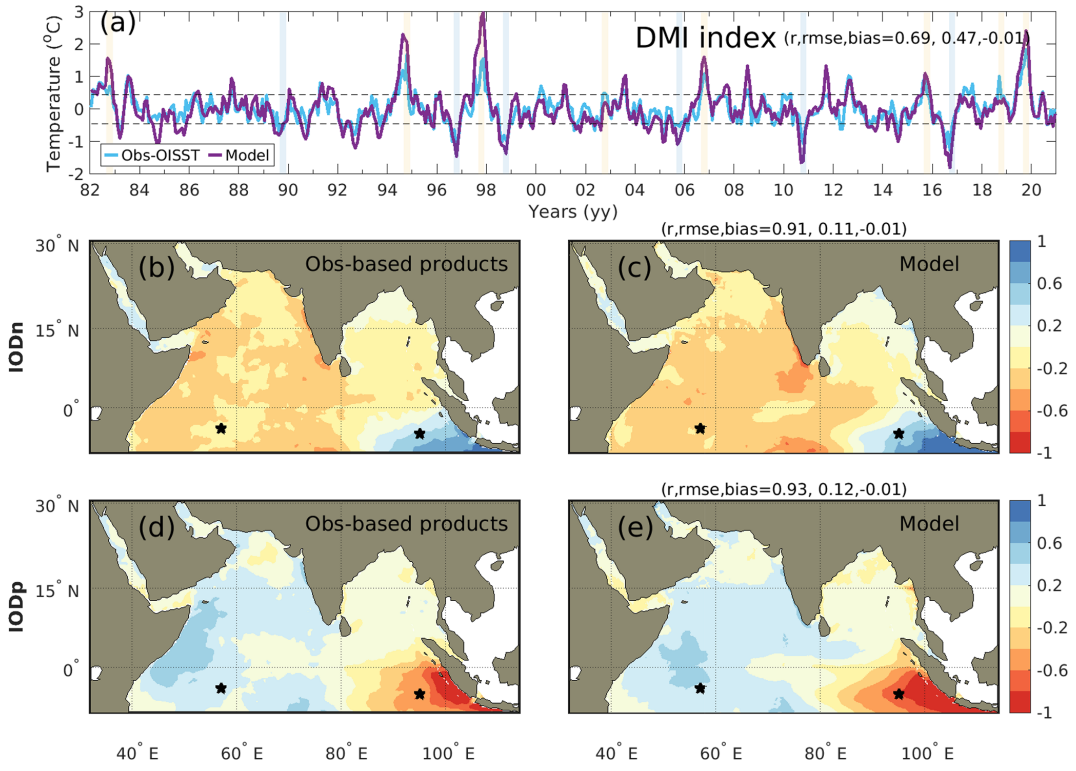

Figure 19. Interannual variability associated with the Indian Ocean Dipole (IOD). **(a)** Dipole mode index (DMI) which quantifies the intensity of the IOD phases; **(b, c)** SST composites during IOD negative phases (IODn) in observations and MOM6-COBALT-IND12 model; **(d, e)** SST composite during IOD positive phases (IODp) in observations and MOM6-COBALT-IND12 model. Composites are for September-to-November months of positive (1982, 1994, 1997, 2002, 2006, 2015, 2018, 2019) and negative (1989, 1996, 1998, 2005, 2010, 2016) IODs. SST observations are from OISSTv2.1 (see Table 2). Black stars indicate the positions of two Research Moored Array for African–Asian–Australian Monsoon Analysis and Prediction (RAMA) moorings used in Fig. 20.

Ocean. On intraseasonal time-scales, the model also reproduces the hotspots of variability associated with eddies, filaments and planetary waves, and on interannual time-scales the east-west variability in the thermocline introduced by the IOD. This strong physical performance likely stems from the effective parameterizations of surface heat and momentum fluxes, combined with well-constrained surface forcing fields derived from ERA5 reanalysis.

The good agreement between observed and modeled physical features provides a foundation for accurately simulating the ocean biogeochemical and biological response. This includes the intensity and timing of the seasonal blooms triggered by monsoonal circulation changes and modulated by intraseasonal features such as eddies and filaments, and interannual IOD phases. Specifically, the model reproduces the summer bloom associated with coastal upwelling systems and their extension offshore in mesoscale filaments, as well as the winter bloom associated with convective mixing and modulated by fine-scale eddies (Lévy et al., 2007; Resplandy et al., 2011, 2012; Mahadevan, 2016; Lachkar et al., 2016; Rixen et al., 2019a; Vinayachandran et al., 2021; Anjaneyan et al., 2023). These biogeochemical improvements reflect the targeted model development efforts outlined above. The model also captures the patterns and amplitude of the phytoplankton changes expected in response to the IOD positive and negative phases. This includes the modulation of the production in the equatorial region, the Arabian Sea and around the tip of India, although we note these patterns are difficult to generalize to all IOD events. As illustrated by Wiggert et al. (2009), the chlorophyll responses vary with IOD intensity-for instance, concentrations in the Arabian Sea decreased during the 1997 event but increased during the 2006 event.

The comparison (Fig. A8) between MOM6-COBALT-IND12 and the global model of Liao et al. (2020) demonstrates that the regional model more realistically captures high-frequency variability in SSH, mesoscale dynamics, meandering jets, and planetary waves (Rossby and Kelvin waves). These features significantly influence nutrient and oxygen transport and mixing, as well as the timing and spatial patterns of seasonal phytoplankton blooms across the Indian Ocean. Our regional configuration also notably improves the representation of marginal sea outflows, particularly from the Red Sea, where global models typically over-

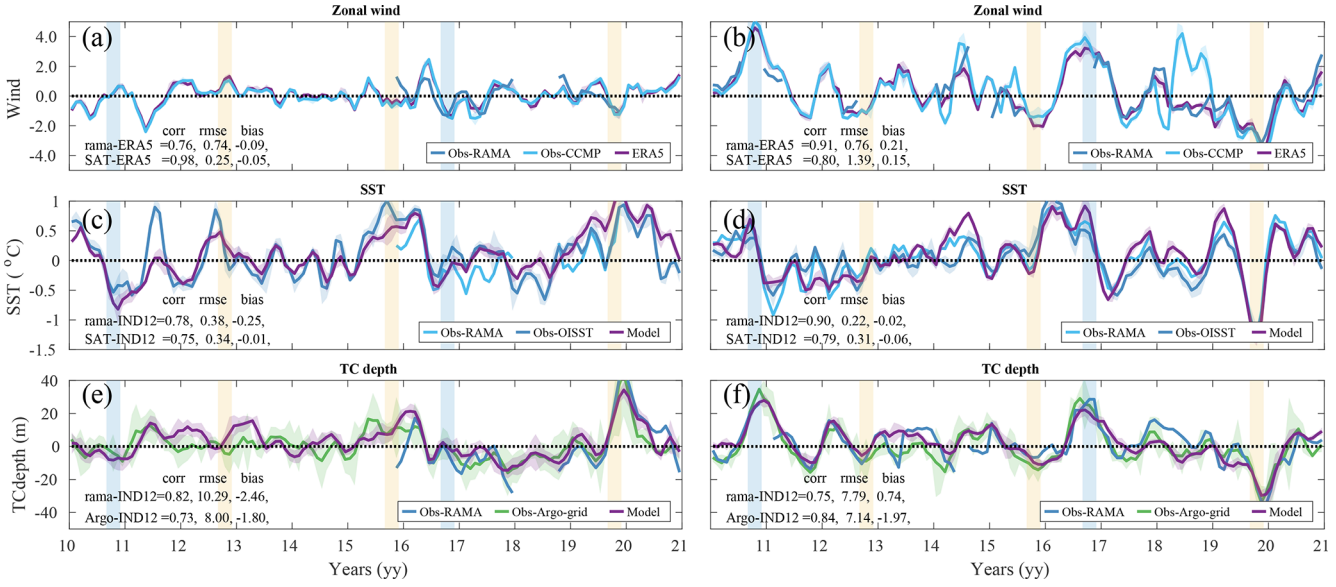

Figure 20. Interannual variability associated with the Indian Ocean Dipole (IOD) at two RAMA moorings in western (**a, c, e**: 57° E, 4° S) and eastern (**b, d, f**: 90° E, 5° S) equatorial Indian Ocean. **(a, b)** Zonal wind ($m\,s^{-1}$) from observations (RAMA mooring and CCMP satellite) and the ERA5 reanalysis used to force MOM6-COBALT-IND12; **(c, d)** SST in observations (RAMA moorings and OISSTv2.1) and in MOM6-COBALT-IND12; **(e, f)** thermocline depth (TCdepth) is calculated as the depth of the 20 °C isotherm. Positive and negative IODs are indicated by orange and blue shading. Correlation coefficients r, RMSE and bias between the observed and reanalysis or model time-series are indicated in each panel. Positions of the two RAMA moorings are shown by black stars in Fig. 19.

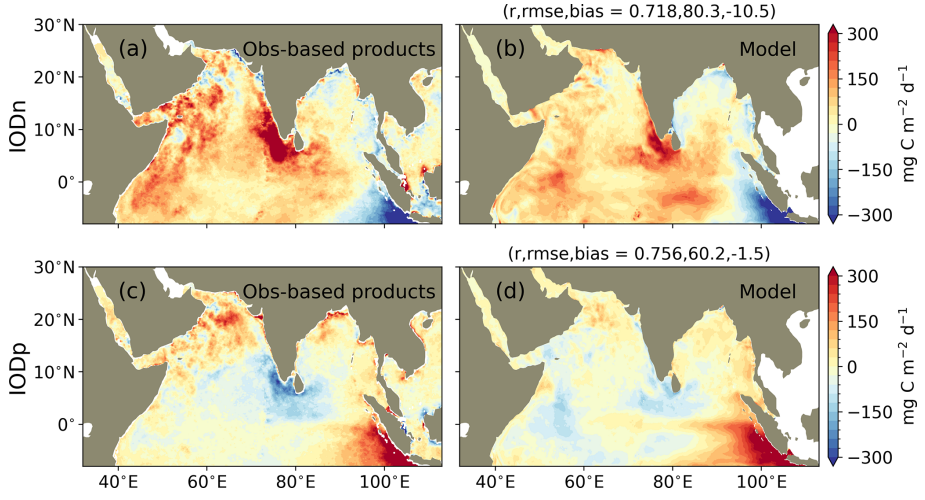

Figure 21. Integrated net primary productivity (PP) anomaly associated with the Indian Ocean Dipole (IOD). September-to-November PP composites during **(a, b)** IOD negative phases (IODn) and **(c, d)** IOD positive phases (IODp) in observation-based product and MOM6-COBALT-IND12. Composites are for September to November months available in CbPM satellite product for positive (2002, 2006, 2015, 2018, 2019) and negative (2005, 2010, 2016) IODs (see Table 2 for details on data).

estimate overflow strength. Furthermore, targeted parameter adjustments – including river discharge, nutrient load, detritus sinking rate, and nitrogen cycle parameterization – improve dissolved oxygen simulations in both the Arabian Sea and the Bay of Bengal. Collectively, these refinements, substantially improve the accuracy and reliability of physical and biogeochemical processes simulated by our regional model.

During the setup and customization of the MOM6-COBALT-IND12 v1.0 model, we identified a series of physical and biogeochemical parameters and forcings that influenced the model simulation and led to a significant improvement of the results (see details in Sect. 2). One of the factors

that influenced our results were river discharge and nutrient loadings, especially in the Bay of Bengal which hosts major river systems such as the Ganges, Brahmaputra, Irrawaddy and Sittang rivers. A first version of the model used the river inputs from the Japanese 55-year Reanalysis (JRA55-do, Kobayashi et al., 2015) instead of the modified GloFAS product presented in this study. However, we found systematic biases in the timing, amplitude and variability of the riverine discharge in JRA55-do. These biases include a systematic delay of 1–2 months in the annual maximum discharge and a lower intraseasonal variability (Fig. A1), which led to biases in river plume dynamics and SSS in the northern Bay of Bengal and the eastern Arabian Sea, in line with observations showing that riverine discharge timing and variability are critical to salinity patterns and plume dynamics (Li et al., 2021). In addition to river discharge, we modified nutrient loadings to match available observational constraints which was important to reproduce productivity patterns in the coastal Bay of Bengal. We note that the influence of riverine inputs could be further improved by accounting for the anthropogenic increase in riverine nutrient supply (MOM6-COBALT-IND12 v1.0 includes nutrient inputs equivalent to year 2000 from Mayorga et al., 2010), which would likely introduce a long-term trend in coastal primary productivity and oxygen concentrations in the vicinity of large river systems.

While the MOM6-COBALT-IND12 v1.0 configuration is remarkably successful at capturing many of the features and observed variability of the northern Indian Ocean, there are still some areas where there is potential for improvement. The main model bias is the larger horizontal extent and volume of suboxia (oxygen concentrations $< 5\,\mu mol\,kg^{-1}$) simulated in the Bay of Bengal. This bias is a well known limitation of ocean and Earth system models in this region (e.g., Bopp et al., 2013; Schmidt and Eggert, 2016; Ditkovsky et al., 2023). The advective supply of oxygen to the thermocline in the Bay of Bengal is weak, but we expect low oxygen demand to prevent the formation of suboxic waters. However, the subsurface oxygen biological demand is likely too high in the model. Notably, this bias in oxygen in the Bay of Bengal was larger in a prior version of the model, and was mitigated by adjusting some of the model parameters. A first set of changes focused on riverine lithogenic fluxes. The increased influx of riverine lithogenic material by an order of magnitude for major rivers and about 50 % for small rivers protects more particulate organic matter from remineralization due to the ballasting effect, significantly reducing oxygen consumption in the water column. A higher total river input of lithogenic material in the Bay of Bengal resulted in a greater reduction in oxygen consumption compared to the Arabian Sea. A second set of changes focused on detritus sinking velocities and burial. The detritus sinking velocity was increased by 20 % to match sediment trap observations in the region (Rixen et al., 2019b) and the fraction of material that reach the ocean floor and is buried was also increased to match the observation-based reconstruction of LaRowe et al. (2020). These modifications reduced remineralization and oxygen consumption in the subsurface and at depth, further reducing the bias in the size and volume of the Bay of Bengal OMZ, while having a relatively small impact on the Arabian Sea OMZ core where oxygen is entirely depleted. The impact of these modifications are consistent with findings from Luo et al. (2024) and Al Azhar et al. (2017), who showed that fast-sinking detritus reduced oxygen consumption and shrank OMZs, expanding oxygenated regions at the OMZ boundaries. A third set of modifications focused on the representation of nitrogen cycling in low oxygen environments. These changes allowed denitrification at oxygen concentrations up to $4\,\mu mol\,kg^{-1}$ (instead of $0.8\,\mu mol\,kg^{-1}$; Paulmier and Ruiz-Pino, 2009), which would promote the use of nitrate for oxidation instead of oxygen and therefore reduce oxygen consumption in suboxic environments.

The three sets of changes described above did not entirely remove the model low oxygen bias in the Bay of Bengal. One limitation of the COBALTv2 biogeochemical model is that it only includes one sinking detritus, which limits our ability to reproduce spatial contrasts in detritus sinking speed. Rixen et al. (2019b) showed that detritus sinking velocities are indeed higher in the Bay of Bengal due to the ballasting effect of riverine mineral particles. In addition, Al Azhar et al. (2017) showed that simulating this contrast between the Arabian Sea where detritus are sinking relatively slowly and the Bay of Bengal where detritus are sinking faster improved the representation of the OMZs in an ocean model. Looking ahead, adding multiple detritus pools with different sinking velocity might be a way to improve the OMZ in the Bay of Bengal. Despite these model limitations, it is important to note that uncertainties remain regarding the strength of suboxia in the Bay of Bengal. Recent observations from Argo floats and ship-based in situ measurements have reported lower oxygen concentrations in the Bay of Bengal than those presented in the WOA dataset, including nanomolar-level oxygen conditions (Bristow et al., 2017; Udaya Bhaskar et al., 2021). These findings suggest that the true extent and intensity of hypoxia in the Bay of Bengal remain uncertain, making it difficult to definitively assess the magnitude of the model bias in this region.

In addition to the OMZs, another area that we are considering for future work is the high bias in surface chlorophyll concentration simulated in the model compared to satellite products, in particular near and offshore summer upwelling systems. An extensive compilation of *in-situ* primary productivity measurements shows that the model successfully captures the seasonality in productivity. This strongly suggests that the bias is limited to the phytoplankton chlorophyll content without influencing its carbon content. This bias in chlorophyll is likely due to an overestimation of the contribution of large phytoplankton (higher chlorophyll to carbon ratio) compared to small phytoplankton (lower chlorophyll to carbon ratio), and is therefore expected to have a relatively small impact on nutrient uptake by phytoplankton

and oxygen consumption associated with the remineralization of the organic matter in the water column. This bias in chlorophyll content might be mitigated in the future when using the COBALT version 3 biogeochemical module which incorporates four phytoplankton groups instead of three, including a medium size class that allows for a smoother transition from small to large, and accounts for photoacclimation and photoadaptation which is critical in simulating chlorophyll (Stock et al., 2025). While this bias complicates comparisons between model and satellite chlorophyll data, it is primarily confined to chlorophyll and has a limited impact on the model's ability to represent regional nutrient, carbon, and oxygen dynamics key to marine ecosystems.

With these results, we are confident that MOM6-COBALT-IND12 is an effective and versatile model to tackle applications in physical and biogeochemical oceanography, as well as applications to marine resources and management on timescales of weeks to decades in northern Indian Ocean. This configuration is particularly well-suited for evaluating the impacts of natural variability and anthropogenic activities on key environmental variables that influence marine resources. One key application is evaluating the risk of coastal hypoxia – an increasingly pressing issue for local populations and the blue economy, including fisheries, in the region (Naqvi et al., 2009; Vallivattathillam et al., 2017; Pearson et al., 2022; Naqvi, 2021, 2022). Despite its importance, coastal hypoxia is often only marginally addressed in global studies, which focus primarily on hypoxia events in Europe and North America (Breitburg et al., 2018; Deutsch et al., 2024). MOM6-COBALT-IND12 is ideally suited to investigate the physical and biological drivers of coastal hypoxia in the northern Indian Ocean, as well as their spatio-temporal variability. This capability is essential for predicting hypoxic events and informing effective management strategies to safeguard marine ecosystems and coastal economies.

Appendix A: Additional figures

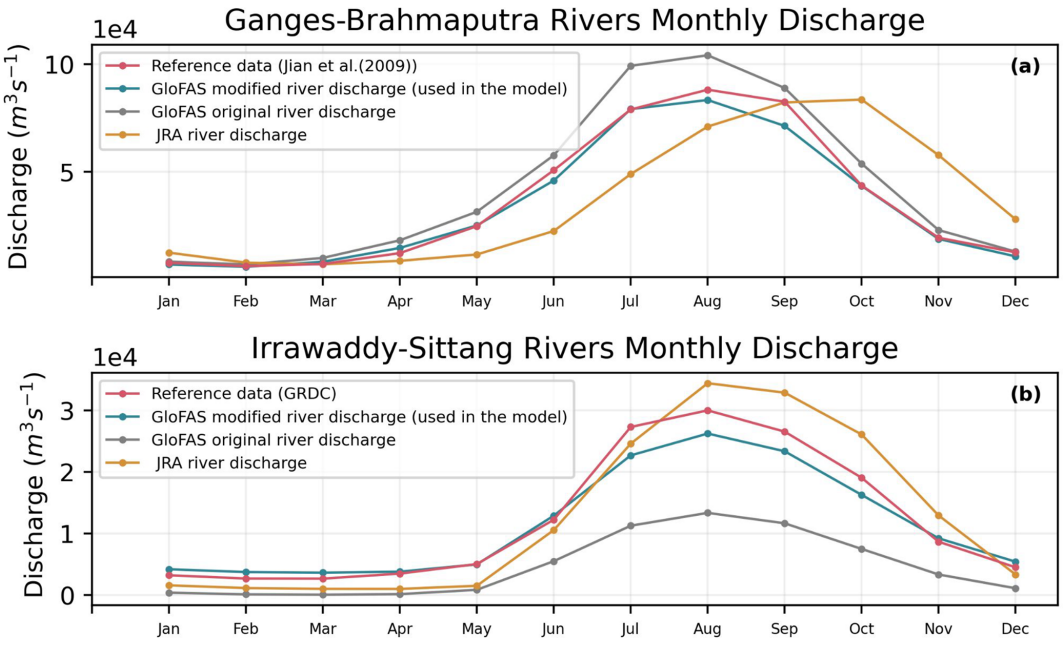

Figure A1. Water discharge in the **(a)** Ganges-Brahmaputra and **(b)** Irrawaddy-Sittang river systems from observations (red), the raw GloFAS-ERA5 runoff product (grey, Harrigan et al., 2023, 2020), the modified GloFAS-ERA5 runoff product used to force MOM6-COBALT-IND12 (teal, $0.75 \times$ GloFAS-ERA5 $\mathrm{m^3\,s^{-1}}$ for Ganges-Brahmaputra and $1.7 \times$ GloFAS-ERA5 $+ 3564\,\mathrm{m^3\,s^{-1}}$ for Irrawaddy-Sittang), and in the JRA55-do reanalysis (orange, Tsujino et al., 2018). Observations are from Jian et al. (2009) for Ganges-Brahmaputra and Recknagel et al. (GRDC, 2023) for Irrawaddy-Sittang. We note that the raw GloFAS-ERA5 can overestimates or underestimate the discharge compared to observations, while JRA55-do presents a systematic 1–2 months delay in the timing of the seasonal peak runoff.

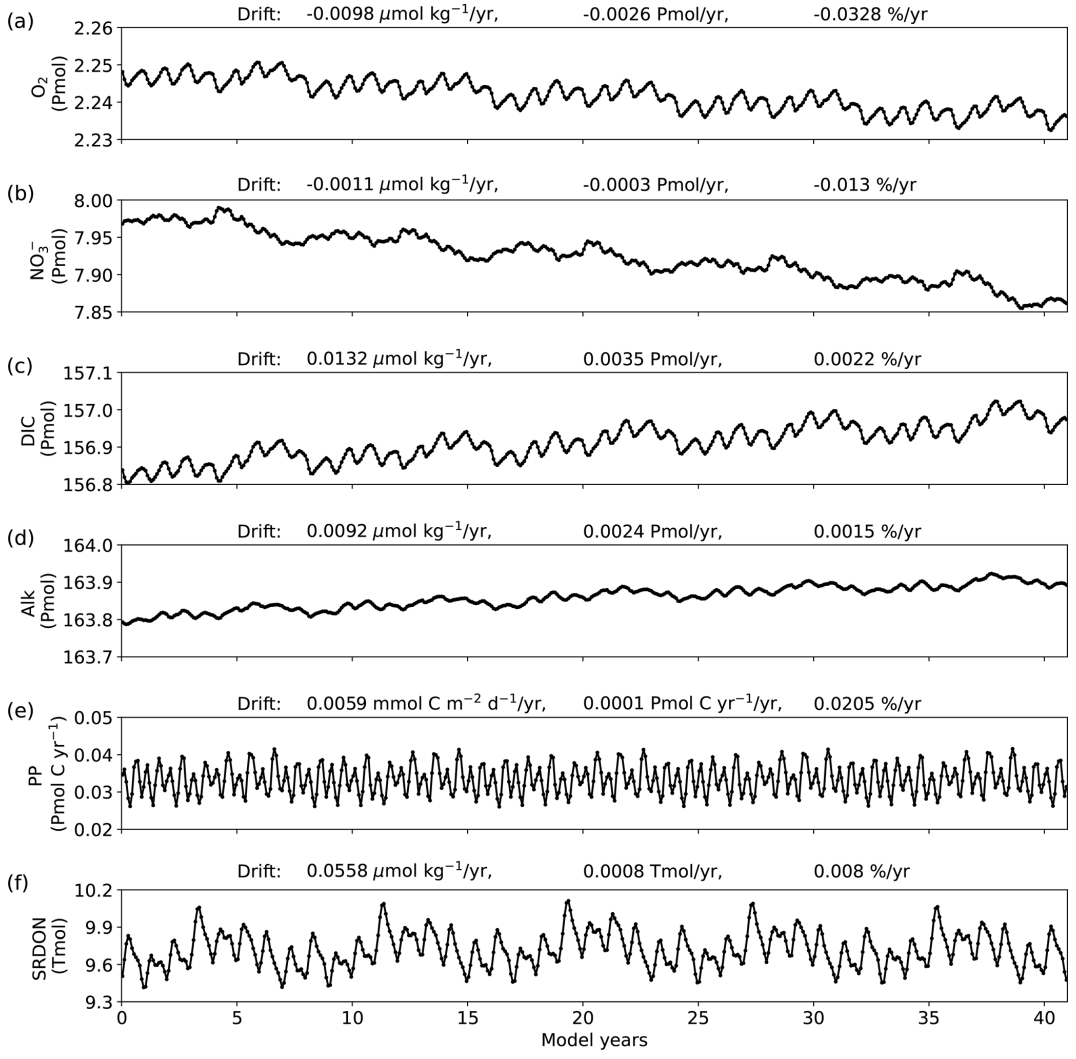

Figure A2. Model time series and drift evaluated as the linear trend after the 32-year spin-up in the control simulation with constant forcing: **(a)** total oxygen (O_2), **(b)** total nitrate (NO_3^-), **(c)** total dissolved inorganic carbon (DIC), **(d)** total alkalinity (Alk), **(e)** total vertically integrated primary productivity (PP) and **(f)** total semi-refractory dissolved organic nitrogen (SRDON). Drifts are indicated above each panel and are all < 0.05 %.

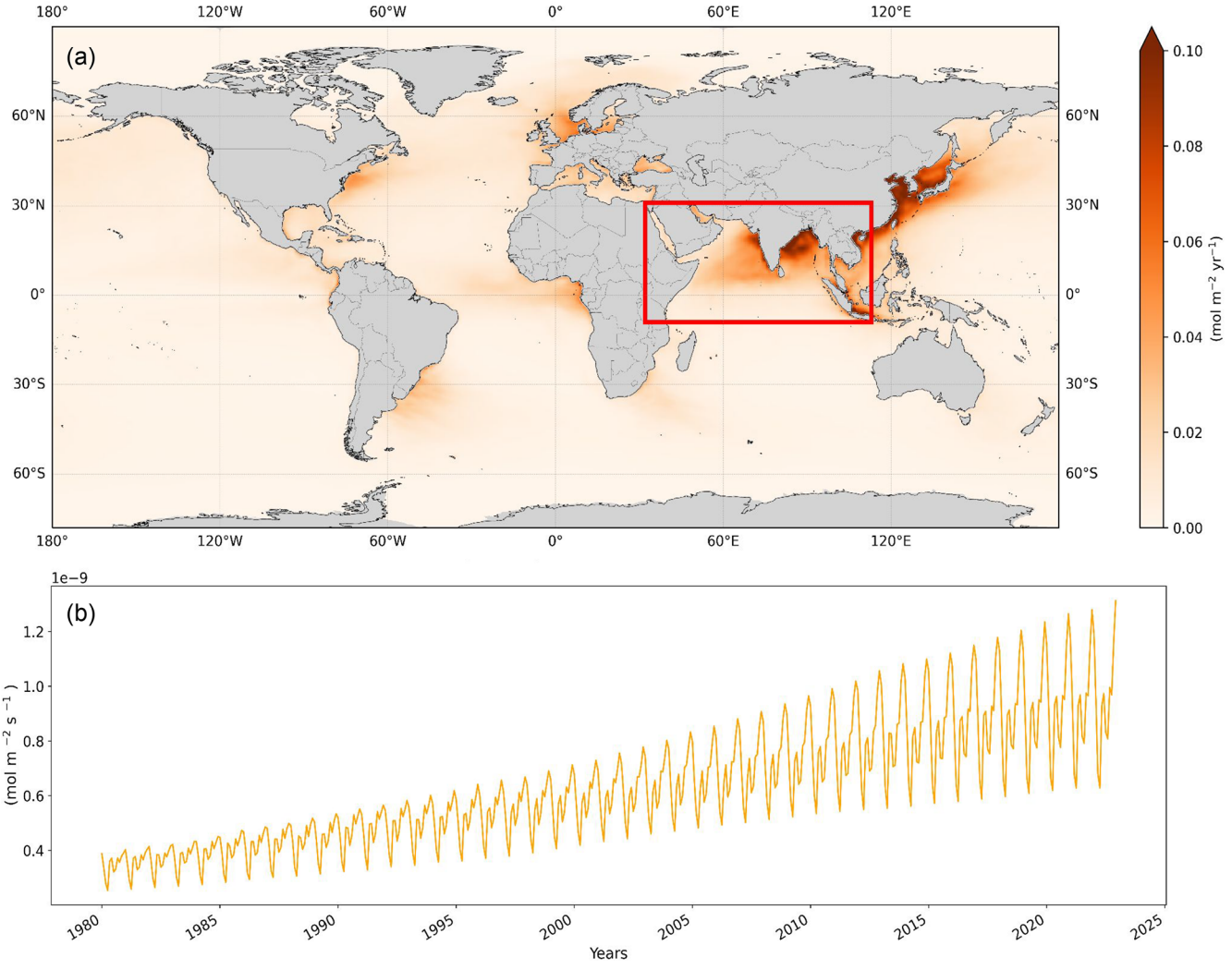

Figure A3. Atmospheric deposition of nitrogen from the earth system model ESM4.1 used to force MOM6-COBALT-IND12: **(a)** spatial distribution in year 2020, and **(b)** temporal evolution averaged over the model domain calculated using a 15-year monthly moving average (see Sect. 2.4.2).

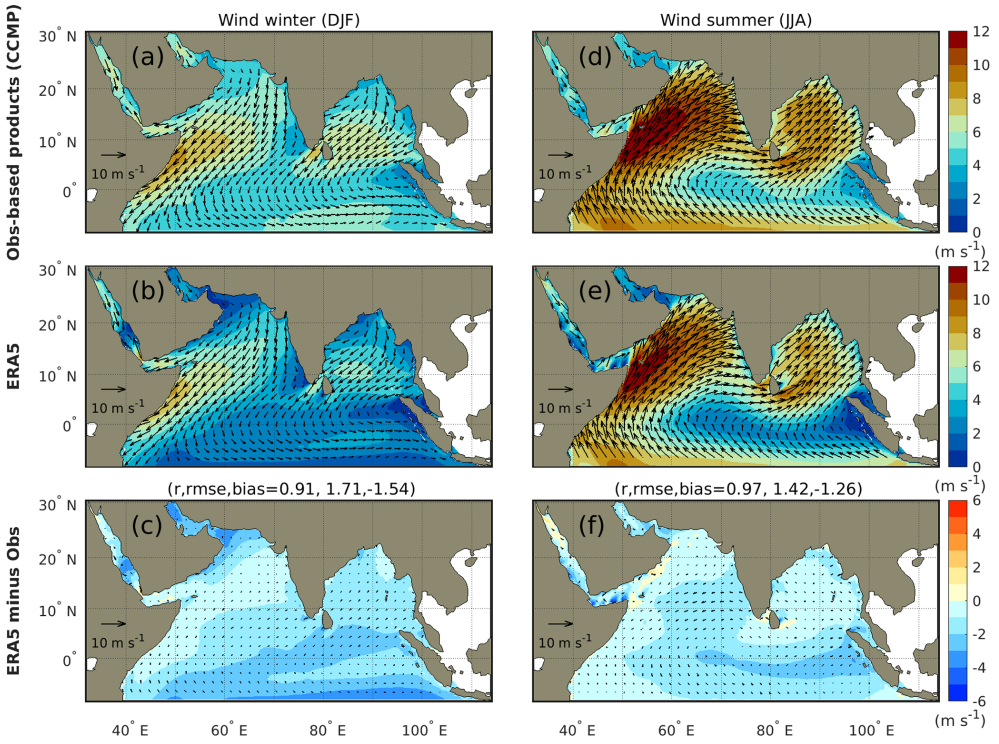

Figure A4. Surface wind (10 m) during **(a–c)** winter (December–February) and **(d–f)** summer (June–August) monsoons. Panels **(a, d)** show Cross-Calibrated Multi-Platform (CCMP) satellite observation-based product, **(b, e)** show ERA5 data product and **(c, f)** show differences between ERA5 and CCMP. Correlation coefficients r, RMSE and bias between the data and model seasonal means are indicated. Wind observational data is from CCMP satellite (see details in Table 2). CCMP and ERA5 results are averaged over the 1993–2020 period.

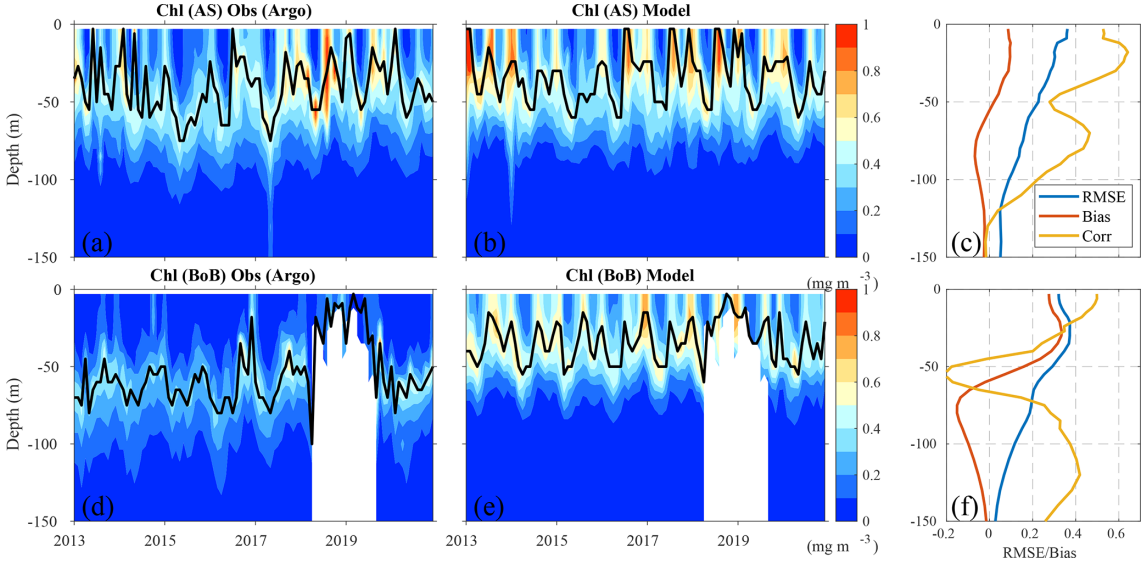

Figure A5. Comparison of observed and modeled vertical chlorophyll profiles in the Arabian Sea **(a–c)** and Bay of Bengal **(d–f)** using Argo float observations and model output. Panels **(a, d)** show Argo-derived chlorophyll concentrations; **(b, e)** show model-simulated chlorophyll concentrations; **(c, f)** show depth profiles of root mean square error (RMSE), bias, and correlation coefficient between model and Argo observations. In panels **(a, b)** and **(d, e)**, the black contour line indicates the depth of the subsurface chlorophyll maximum (SCM). Chlorophyll concentrations are shown in mg m^{-3}.

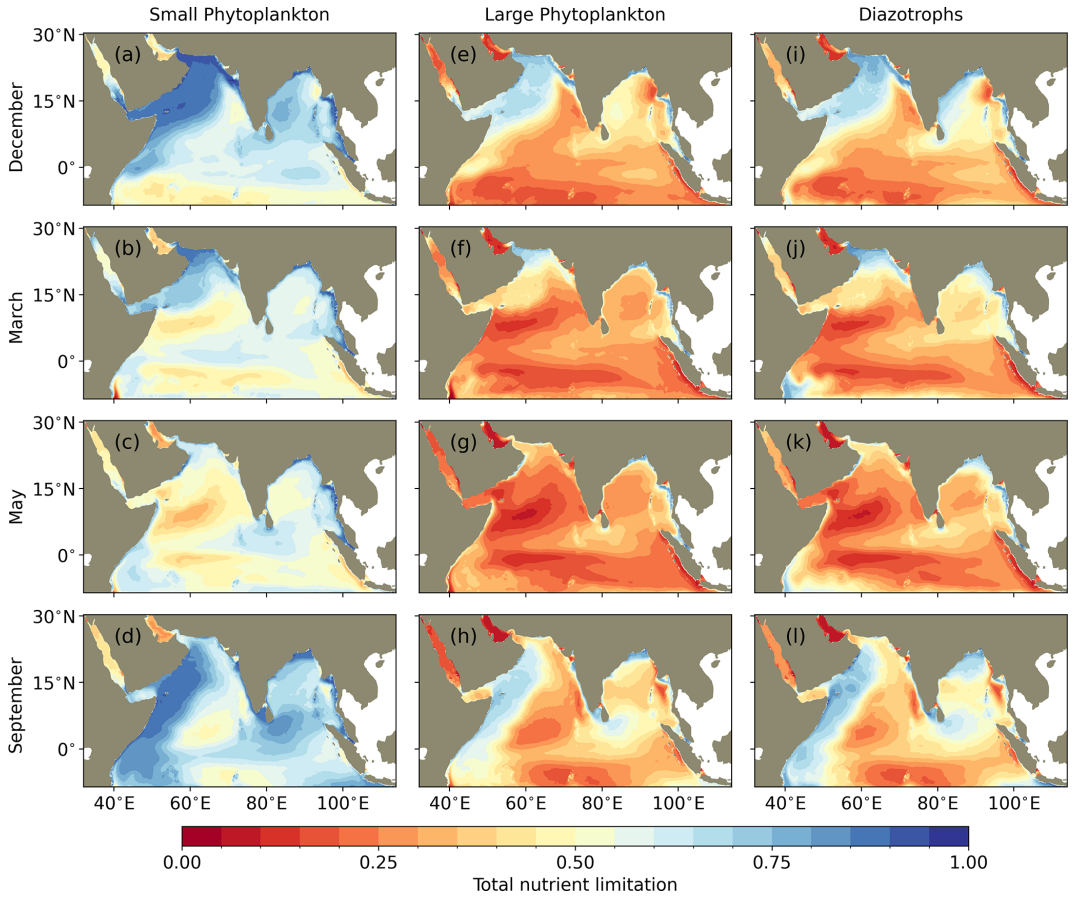

Figure A6. Climatological surface total nutrient limitation (nitrogen N, phosphorus P and iron Fe) following Liebig's Law of the Minimum in MOM6-COBALT-IND12 for small phytoplankton, large phytoplankton and diazotrophs in December, March, May and September. Model climatology is for 1980–2020. A value of 1 indicates no growth limitation by nutrients, whereas a value of 0 indicates complete growth limitation by nutrients.

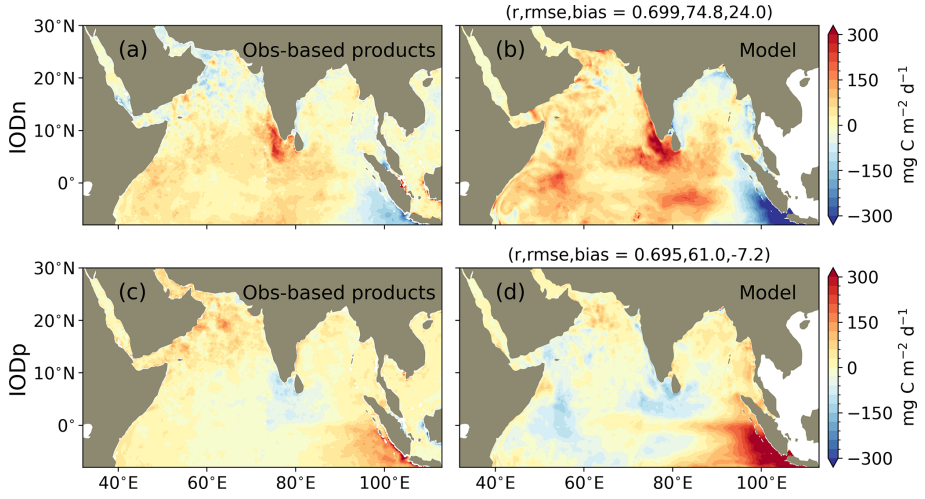

Figure A7. Integrated net primary productivity (PP) anomaly associated with the Indian Ocean Dipole (IOD). September-to-November PP composites during **(a, b)** IOD negative phases and **(c, d)** IOD positive phases in observation-based product and MOM6-COBALT-IND12. Composites are for September-to-November months available in the CAFE satellite product for positive (2002, 2006, 2015, 2018, 2019) and negative (2005, 2010, 2016) IODs (see Table 2 for details on data). Panels **(a)** and **(c)** of this figure showing the CAFE satellite product can be compared to Fig. 21a and c showing the same composites but for the CbPM satellite product.

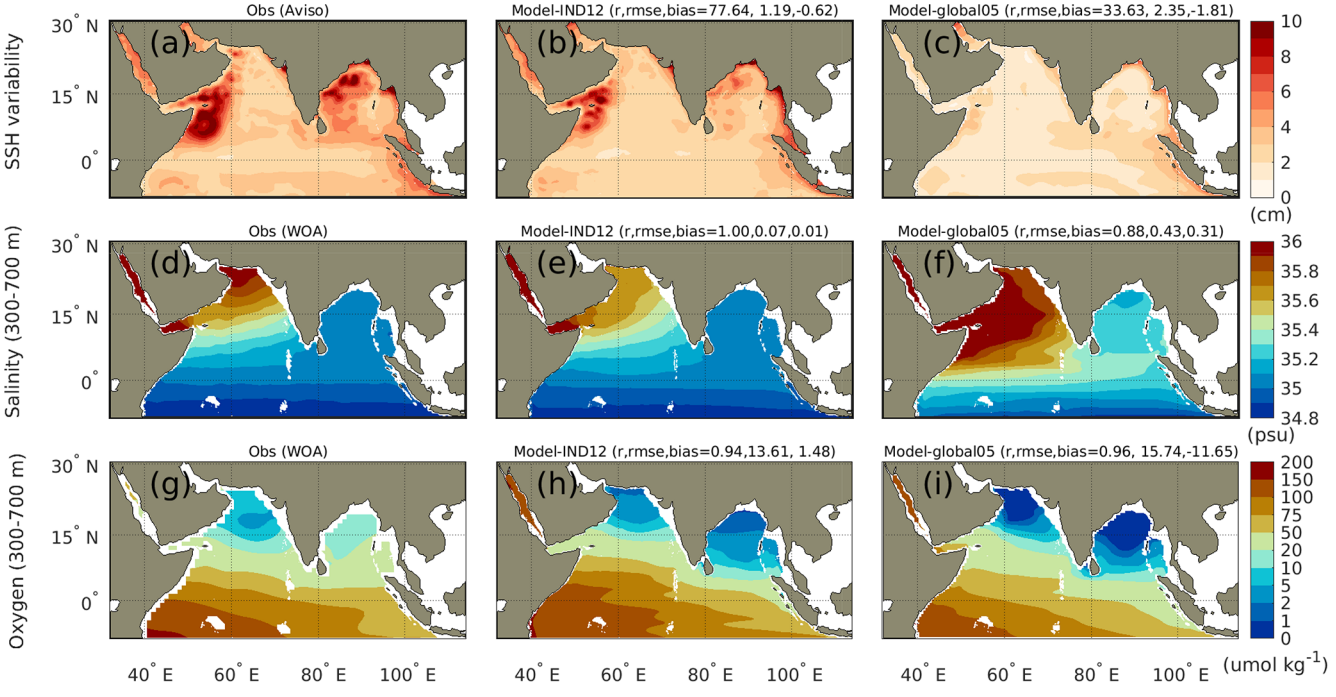

Figure A8. Comparison of sea level anomaly intraseasonal variability, subsurface salinity, and subsurface dissolved oxygen between observational products, the regional MOM6-COBALT-IND12 model (labeled as Model-IND12), and the global MOM6-COBALT configuration at 0.5° resolution (labeled as Model-global05). Panels **(a–c)** show the standard deviation of SLA representing intraseasonal variability (cm); panels **(d–f)** show the mean salinity averaged over 300–700 m depth (psu); and panels **(g–i)** show the mean dissolved oxygen averaged over 300–700 m depth. Comparison statistics – correlation coefficient (r), root mean square error (RMSE), and bias – are shown in parentheses. SLA intraseasonal variability is computed as the standard deviation of linearly detrended SLA, filtered using a 14–120 d band-pass filter.

Code availability. The source code for the model components is available at https://doi.org/10.5281/zenodo.14184011 (Liao et al., 2024a). The model parameter files and preprocessed forcing data used for the Indian Ocean configuration have been archived at https://doi.org/10.5281/zenodo.14171404 (Liao et al., 2024b). MOM6 is developed openly, with its Git repositories hosted at https://github.com/mom-ocean/MOM6 (last access: 1 February 2023) and https://github.com/NOAA-GFDL/MOM6 (last access: 1 February 2023). These platforms enable users to obtain the latest and experimental versions of the source code, report issues, and contribute new features.

Data availability. The model output analyzed in this study is available at https://doi.org/10.5281/zenodo.14183131 (Yang et al., 2024). The datasets used for model validation and comparison are listed as follows: OISSTv2.1 (https://www.ncei.noaa.gov/products/optimum-interpolation-sst, Reynolds et al., 2007), mixed-layer depth (https://mld.ifremer.fr/Surface_Mixed_Layer_Depth.php, De Boyer Montéut et al., 2004), surface currents (https://podaac.jpl.nasa.gov/dataset/OSCAR_L4_OC_INTERIM_V2.0, ESR, 2009), sea level anomaly (https://doi.org/10.24381/CDS.4C328C78, Lopez, 2018), CCMP wind speed (https://podaac.jpl.nasa.gov/MEaSUREs-CCMP, Mears et al., 2022), OC-CCI v5.0 (https://climate.esa.int/en/projects/ocean-colour/data/, Sathyendranath et al., 2019), RAMA temperature and salinity (https://www.pmel.noaa.gov/gtmba/pmel-theme/indian-ocean-rama, McPhaden et al., 2009), net primary productivity (https://orca.science.oregonstate.edu/index.php, Westberry et al., 2008), and World Ocean Atlas 2018 (https://www.ncei.noaa.gov/archive/accession/NCEI-WOA18, Garcia et al., 2019).

The datasets used to create the model forcing are listed as follows: ORAS5 reanalysis (https://cds.climate.copernicus.eu/datasets, Zuo et al., 2019), TPXO9 (https://www.tpxo.net/home, Egbert and Erofeeva, 2002), GloFAS (https://doi.org/10.24381/cds.a4fdd6b9, Zsoter, 2019), and ERA5 (https://cds.climate.copernicus.eu/datasets, Herbert et al., 2018).

Author contributions. Conceptualization: LR. Data curation: EL, FY, YZ. Formal analysis: EL, FY, YZ, SD, MM, LR. Funding acquisition: LR, CS. Investigation: EL, FY, YZ, SD, MM, LR. Methodology: EL, JP, SD, FY, YZ, ACR, RH, CS, LR. Software: EL, JP, SD, FY, YZ, ACR, MM, RH, CS. Supervision: LR, RH, CS. Visualization: EL, FY, YZ, SD, MM. Writing – original draft: LR. Writing – review and editing: LR, SD, FY, YZ, CS, RH.

Competing interests. The contact author has declared that none of the authors has any competing interests.

Disclaimer. Publisher's note: Copernicus Publications remains neutral with regard to jurisdictional claims made in the text, published maps, institutional affiliations, or any other geographical representation in this paper. While Copernicus Publications makes every effort to include appropriate place names, the final responsibility lies with the authors. Also, please note that this paper has not received English language copy-editing. Views expressed in the text are those of the authors and do not necessarily reflect the views of the publisher.

Acknowledgements. The bio-Argo data were collected and made freely available by the International Argo Program and the national programs that contribute to it (https://argo.ucsd.edu, last access: 1 August 2024; https://www.ocean-ops.org, last access: 1 August 2024). The Argo Program is part of the Global Ocean Observing System.

Financial support. This research has been supported by the NOAA Climate Program Office (grant no. NA21OAR4310119), the High Meadows Environmental Institute, Princeton University (Climate, Chemistry and Life in the Indian Ocean Initiative and Grand Challenge), and the NSF Directorate for Geosciences, Division of Ocean Sciences (grant no. 2042672).

Review statement. This paper was edited by Paul Halloran and reviewed by two anonymous referees.

References

Accad, Y. and Pekeris, C. L.: Solution of the tidal equations for the M_2 and S_2 tides in the world oceans from a knowledge of the tidal potential alone, Philos. T. Roy. Soc. Lond. A, 290, 235–266, https://doi.org/10.1098/rsta.1978.0083, 1978.

Adcroft, A., Anderson, W., Balaji, V., Blanton, C., Bushuk, M., Dufour, C. O., Dunne, J. P., Griffies, S. M., Hallberg, R., Harrison, M. J., Held, I. M., Jansen, M. F., John, J. G., Krasting, J. P., Langenhorst, A. R., Legg, S., Liang, Z., McHugh, C., Radhakrishnan, A., Reichl, B. G., Rosati, T., Samuels, B. L., Shao, A., Stouffer, R., Winton, M., Wittenberg, A. T., Xiang, B., Zadeh, N., and Zhang, R.: The GFDL Global Ocean and Sea Ice Model OM4.0: Model Description and Simulation Features, J. Adv. Model. Earth Syst., 11, 3167–3211, https://doi.org/10.1029/2019MS001726, 2019.

Ahmed, A., Gauns, M., Kurian, S., Bardhan, P., Pratihary, A., Naik, H., Shenoy, D. M., and Naqvi, S.: Nitrogen fixation rates in the eastern Arabian Sea, Estuar. Coast. Shelf Sci., 191, 74–83, https://doi.org/10.1016/j.ecss.2017.04.005, 2017.

Al Azhar, M., Lachkar, Z., Lévy, M., and Smith, S.: Oxygen Minimum Zone Contrasts Between the Arabian Sea and the Bay of Bengal Implied by Differences in Remineralization Depth, Geophys. Res. Lett., 44, 2017GL075157, https://doi.org/10.1002/2017GL075157, 2017.

Anjaneyan, P., Kuttippurath, J., Hareesh Kumar, P. V., Ali, S. M., and Raman, M.: Spatio-temporal changes of winter and spring phytoplankton blooms in Arabian sea during the period 1997–2020, J. Environ. Manage., 332, 117435, https://doi.org/10.1016/j.jenvman.2023.117435, 2023.

Aparna, S. G., McCreary, J. P., Shankar, D., and Vinayachandran, P. N.: Signatures of Indian Ocean Dipole and El Niño–Southern Oscillation events in sea level variations in the

Bay of Bengal, J. Geophys. Res.-Oceans, 117, 2012JC008055, https://doi.org/10.1029/2012JC008055, 2012.

Arakawa, A. and Lamb, V. R.: Computational Design of the Basic Dynamical Processes of the UCLA General Circulation Model, in: Methods in Computational Physics: Advances in Research and Applications, vol. 17, Elsevier, 173–265, ISBN 978-0-12-460817-7, https://doi.org/10.1016/B978-0-12-460817-7.50009-4, 1977.

Banse, K., Naqvi, S. W. A., Narvekar, P. V., Postel, J. R., and Jayakumar, D. A.: Oxygen minimum zone of the open Arabian Sea: variability of oxygen and nitrite from daily to decadal timescales, Biogeosciences, 11, 2237–2261, https://doi.org/10.5194/bg-11-2237-2014, 2014.

Banzon, V., Smith, T. M., Chin, T. M., Liu, C., and Hankins, W.: A long-term record of blended satellite and in situ sea-surface temperature for climate monitoring, modeling and environmental studies, Earth Syst. Sci. Data, 8, 165–176, https://doi.org/10.5194/essd-8-165-2016, 2016.

Barber, R. T., Marra, J., Bidigare, R. C., Codispoti, L. A., Halpern, D., Johnson, Z., Latasa, M., Goericke, R., and Smith, S. L.: Primary productivity and its regulation in the Arabian Sea during 1995, Deep-Sea Res. Pt. II, 48, 1127–1172, https://doi.org/10.1016/S0967-0645(00)00134-X, 2001.

Barton, K. N., Pal, N., Brus, S. R., Petersen, M. R., Arbic, B. K., Engwirda, D., Roberts, A. F., Westerink, J. J., Wirasaet, D., and Schindelegger, M.: Global Barotropic Tide Modeling Using Inline Self-Attraction and Loading in MPAS-Ocean, J. Adv. Model. Earth Syst., 14, e2022MS003207, https://doi.org/10.1029/2022MS003207, 2022.

Beal, L. M. and Donohue, K. A.: The Great Whirl: Observations of its seasonal development and interannual variability, J. Geophys. Res.-Oceans, 118, 1–13, https://doi.org/10.1029/2012JC008198, 2013.

Beal, L. M., Hormann, V., Lumpkin, R., and Foltz, G. R.: The Response of the Surface Circulation of the Arabian Sea to Monsoonal Forcing, J. Phys. Oceanogr., 43, 2008–2022, https://doi.org/10.1175/JPO-D-13-033.1, 2013.

Behrenfeld, M. J. and Falkowski, P. G.: Photosynthetic rates derived from satellite-based chlorophyll concentration, Limnol. Oceanogr., 42, 1–20, https://doi.org/10.4319/lo.1997.42.1.0001, 1997.

Bhattathiri, P., Devassy, V., and Radhakrishna, K.: Primary production in the Bay of Bengal during August 1978, Mahasagar-Bulletin of the National Institute of Oceanography, 13, 315–323, 1980.

Bianchi, D., Dunne, J. P., Sarmiento, J. L., and Galbraith, E. D.: Data-based estimates of suboxia, denitrification, and N_2O production in the ocean and their sensitivities to dissolved O_2: data-based suboxia and denitrification, Global Biogeochem. Cy., 26, https://doi.org/10.1029/2011GB004209, 2012.

Bopp, L., Resplandy, L., Orr, J. C., Doney, S. C., Dunne, J. P., Gehlen, M., Halloran, P., Heinze, C., Ilyina, T., Séférian, R., Tjiputra, J., and Vichi, M.: Multiple stressors of ocean ecosystems in the 21st century: projections with CMIP5 models, Biogeosciences, 10, 6225–6245, https://doi.org/10.5194/bg-10-6225-2013, 2013.

Boyer, T. P., Baranova, O. K., Coleman, C., Garcia, H. E., Grodsky, S. A., Locarnini, R. A., Mishonov, A. V., Paver, C., Reagan, J. R., Seidov, D., Smolyar, I. V., and Zweng, M. M.: World Ocean Database 2013, in: NOAA Atlas, vol. 87, NESDIS, Silver Spring, MD, https://doi.org/10.7289/V5NZ85MT, 2018.

Brandt, P., Dengler, M., Rubino, A., Quadfasel, D., and Schott, F.: Intraseasonal variability in the southwestern Arabian Sea and its relation to the seasonal circulation, Deep-Sea Res. Pt. II, 50, 2129–2141, https://doi.org/10.1016/S0967-0645(03)00049-3, 2003.

Breitburg, D., Levin, L. A., Oschlies, A., Gréoire, M., Chavez, F. P., Conley, D. J., Garçon, V., Gilbert, D., Gutiérrez, D., Isensee, K., Jacinto, G. S., Limburg, K. E., Montes, I., Naqvi, S. W. A., Pitcher, G. C., Rabalais, N. N., Roman, M. R., Rose, K. A., Seibel, B. A., Telszewski, M., Yasuhara, M., and Zhang, J.: Declining oxygen in the global ocean and coastal waters, Science, 359, eaam7240, https://doi.org/10.1126/science.aam7240, 2018.

Bristow, L. A., Dalsgaard, T., Tiano, L., Mills, D. B., Bertagnolli, A. D., Wright, J. J., Hallam, S. J., Ulloa, O., Canfield, D. E., Revsbech, N. P., and Thamdrup, B.: Ammonium and nitrite oxidation at nanomolar oxygen concentrations in oxygen minimum zone waters, P. Natla. Acad. Sci. USA, 113, 10601–10606, 2016.

Bristow, L. A., Callbeck, C. M., Larsen, M., Altabet, M. A., Dekaezemacker, J., Forth, M., Gauns, M., Glud, R. N., Kuypers, M. M. M., Lavik, G., Milucka, J., Naqvi, S. W. A., Pratihary, A., Revsbech, N. P., Thamdrup, B., Treusch, A. H., and Canfield, D. E.: N_2 production rates limited by nitrite availability in the Bay of Bengal oxygen minimum zone, Nat. Geosci., 10, 24–29, https://doi.org/10.1038/ngeo2847, 2017.

Bruce, J. G., Johnson, D. R., and Kindle, J. C.: Evidence for eddy formation in the eastern Arabian Sea during the northeast monsoon, J. Geophys. Res.-Oceans, 99, 7651–7664, https://doi.org/10.1029/94JC00035, 1994.

Burek, P., Van der Knijff, J., and De Roo, A.: LISFLOOD, distributed water balance and flood simulation model :revised user manual 2013, JRC78917, Publications Office of the European Union, LU, https://doi.org/10.2788/24982, 2013.

Cai, W., Zheng, X.-T., Weller, E., Collins, M., Cowan, T., Lengaigne, M., Yu, W., and Yamagata, T.: Projected response of the Indian Ocean Dipole to greenhouse warming, Nat. Geosci., 6, 999–1007, https://doi.org/10.1038/ngeo2009, 2013.

Cai, W., Yang, K., Wu, L., Huang, G., Santoso, A., Ng, B., Wang, G., and Yamagata, T.: Opposite response of strong and moderate positive Indian Ocean Dipole to global warming, Nat. Clim. Change, 11, 27–32, https://doi.org/10.1038/s41558-020-00943-1, 2021.

Carter, B. R., Bittig, H. C., Fassbender, A. J., Sharp, J. D., Takeshita, Y., Xu, Y.-Y., Álvarez, M., Wanninkhof, R., Feely, R. A., and Barbero, L.: New and updated global empirical seawater property estimation routines, Limnol. Oceanogr.: Meth., 19, 785–809, https://doi.org/10.1002/lom3.10461, 2021.

Chakraborty, K., Rose, L., Bhattacharya, T., Ghosh, J., Ghoshal, P. K., and Akhand, A.: Primary Productivity Dynamics in the Northern Indian Ocean: An Ecosystem Modeling Perspective, Springer International Publishing, Cham, 169–190, ISBN 978-3-031-34467-1, https://doi.org/10.1007/978-3-031-34467-1_8, 2023.

Chelton, D. B., Deszoeke, R. A., Schlax, M. G., El Naggar, K., and Siwertz, N.: Geographical variability of the first baroclinic Rossby radius of deformation, J. Phys. Oceanogr., 28, 433–460, https://doi.org/10.1175/1520-0485(1998)028<0433:GVOTFB>2.0.CO;2, 1998.

Cheng, X., Xie, S.-P., McCreary, J. P., Qi, Y., and Du, Y.: Intraseasonal variability of sea surface height in the Bay of Bengal, J. Geophys. Res.-Oceans, 118, 816–830, https://doi.org/10.1002/jgrc.20075, 2013.

Cheng, X., McCreary, J. P., Qiu, B., Qi, Y., and Du, Y.: Intraseasonal-to-semiannual variability of sea-surface height in the astern, equatorial Indian Ocean and southern Bay of Bengal, J. Geophys. Res.-Oceans, 122, 4051–4067, https://doi.org/10.1002/2016JC012662, 2017.

Currie, J. C., Lengaigne, M., Vialard, J., Kaplan, D. M., Aumont, O., Naqvi, S. W. A., and Maury, O.: Indian Ocean Dipole and El Niño/Southern Oscillation impacts on regional chlorophyll anomalies in the Indian Ocean, Biogeosciences, 10, 6677–6698, https://doi.org/10.5194/bg-10-6677-2013, 2013.

Dalpadado, P., Arrigo, K. R., Van Dijken, G. L., Gunasekara, S. S., Ostrowski, M., Bianchi, G., and Sperfeld, E.: Warming of the Indian Ocean and its impact on temporal and spatial dynamics of primary production, Prog. Oceanogr., 198, 102688, https://doi.org/10.1016/j.pocean.2021.102688, 2021.

De Boyer Montégut, C., Madec, G., Fischer, A. S., Lazar, A., and Iudicone, D.: Mixed layer depth over the global ocean: An examination of profile data and a profile-based climatology, J. Geophys. Res.-Oceans, 109, 2004JC002378, https://doi.org/10.1029/2004JC002378, 2004.

Deutsch, C., Ferrel, A., Seibel, B., Pörtner, H.-O., and Huey, R. B.: Climate change tightens a metabolic constraint on marine habitats, Science, 348, 1132–1135, https://doi.org/10.1126/science.aaa1605, 2015.

Deutsch, C., Penn, J. L., and Lucey, N.: Climate, Oxygen, and the Future of Marine Biodiversity, Annu. Rev. Mar. Sci., 16, 217–245, https://doi.org/10.1146/annurev-marine-040323-095231, 2024.

Devassy, V., Bhattathiri, P., and Radhakrishna, K.: Primary production in the Bay of Bengal during August 1977, Mahasagar – Bulletin of the National Institute of Oceanography, 16, 443–447, https://drs.nio.res.in/drs/handle/2264/6553 (last access: 10 July 2024), 1983.

Dierssen, H. M.: Perspectives on Empirical Approaches for Ocean Color Remote Sensing of Chlorophyll in a Changing Climate, P. Natl. Acad. Sci. USA, 107, 17073–17078, https://doi.org/10.1073/pnas.0913800107, 2010.

Ditkovsky, S., Resplandy, L., and Busecke, J.: Unique ocean circulation pathways reshape the Indian Ocean oxygen minimum zone with warming, Biogeosciences, 20, 4711–4736, https://doi.org/10.5194/bg-20-4711-2023, 2023.

do Rosário Gomes, H., Goes, J. I., Matondkar, S. P., Parab, S. G., Al-Azri, A. R., and Thoppil, P. G.: Blooms of Noctiluca miliaris in the Arabian Sea – An in situ and satellite study, Deep-Sea Res. Pt. I, 55, 751–765, https://doi.org/10.1016/j.dsr.2008.03.003, 2008.

Dunne, J. P., Sarmiento, J. L., and Gnanadesikan, A.: A synthesis of global particle export from the surface ocean and cycling through the ocean interior and on the seafloor, Global Biogeochem. Cy., 21, GB4006, https://doi.org/10.1029/2006GB002907, 2007.

Egbert, G. D. and Erofeeva, S. Y.: Efficient Inverse Modeling of Barotropic Ocean Tides, J. Atmos. Ocean. Tech., 19, 183–204, https://doi.org/10.1175/1520-0426(2002)019<0183:EIMOBO>2.0.CO;2, 2002.

ESR: OSCAR third degree resolution ocean surface currents, https://doi.org/10.5067/OSCAR-03D01, 2009.

Flather, R.: A Tidal Model of the North-West European Continental Shelf, Memoires de la Societe Royale des Sciences de Liege, 10, 141–164, 1976.

Fox-Kemper, B., Danabasoglu, G., Ferrari, R., Griffies, S., Hallberg, R., Holland, M., Maltrud, M., Peacock, S., and Samuels, B.: Parameterization of mixed layer eddies. III: Implementation and impact in global ocean climate simulations, Ocean Model., 39, 61–78, https://doi.org/10.1016/j.ocemod.2010.09.002, 2011.

Frey, C., Sun, X., Szemberski, L., Casciotti, K. L., Garcia-Robledo, E., Jayakumar, A., Kelly, C. L., Lehmann, M. F., and Ward, B. B.: Kinetics of nitrous oxide production from ammonia oxidation in the Eastern Tropical North Pacific, Limnol. Oceanogr., 68, 424–438, https://doi.org/10.1002/lno.12283, 2023.

Friedlingstein, P., Jones, M. W., O'Sullivan, M., Andrew, R. M., Bakker, D. C. E., Hauck, J., Le Qu eré, C., Peters, G. P., Peters, W., Pongratz, J., Sitch, S., Canadell, J. G., Ciais, P., Jackson, R. B., Alin, S. R., Anthoni, P., Bates, N. R., Becker, M., Bellouin, N., Bopp, L., Chau, T. T. T., Chevallier, F., Chini, L. P., Cronin, M., Currie, K. I., Decharme, B., Djeutchouang, L. M., Dou, X., Evans, W., Feely, R. A., Feng, L., Gasser, T., Gilfillan, D., Gkritzalis, T., Grassi, G., Gregor, L., Gruber, N., Gürses, Ö., Harris, I., Houghton, R. A., Hurtt, G. C., Iida, Y., Ilyina, T., Luijkx, I. T., Jain, A., Jones, S. D., Kato, E., Kennedy, D., Klein Goldewijk, K., Knauer, J., Korsbakken, J. I., Körtzinger, A., Landschützer, P., Lauvset, S. K., Lefèvre, N., Lienert, S., Liu, J., Marland, G., McGuire, P. C., Melton, J. R., Munro, D. R., Nabel, J. E. M. S., Nakaoka, S.-I., Niwa, Y., Ono, T., Pierrot, D., Poulter, B., Rehder, G., Resplandy, L., Robertson, E., Rödenbeck, C., Rosan, T. M., Schwinger, J., Schwingshackl, C., Séférian, R., Sutton, A. J., Sweeney, C., Tanhua, T., Tans, P. P., Tian, H., Tilbrook, B., Tubiello, F., van der Werf, G. R., Vuichard, N., Wada, C., Wanninkhof, R., Watson, A. J., Willis, D., Wiltshire, A. J., Yuan, W., Yue, C., Yue, X., Zaehle, S., and Zeng, J.: Global Carbon Budget 2021, Earth Syst. Sci. Data, 14, 1917–2005, https://doi.org/10.5194/essd-14-1917-2022, 2022.

Gandhi, N., Ramesh, R., Srivastava, R., Sheshshayee, M. S., Dwivedi, R. M., and Raman, M.: Nitrogen Uptake Rates during Spring in the NE Arabian Sea, Int. J. Oceanogr., 2010, 1–10, https://doi.org/10.1155/2010/127493, 2010.

Gandhi, N., Singh, A., Ramesh, R., and Sheshshayee, M. S.: Nitrogen Sources for new production in the northeast Indian Ocean, Int. J. Oceanogr., 55–67, https://doi.org/10.1142/9789814355353_0004, 2011.

Garcia, H., Boyer, T., Baranova, O., Locarnini, R., Mishonov, A., Grodsky, A., Paver, C., Weathers, K., Smolyar, I., Reagan, J., Seidov, D., and Zweng, M.: World Ocean Atlas 2018: Product Documentation, in: NOAA Atlas, Technical Edn., edited by: Mishonov, A., Tech. rep., NOAA, https://data.nodc.noaa.gov/woa/WOA18/DOC/woa18documentation.pdf (last access: 1 August 2024), 2019.

Gauns, M., Madhupratap, M., Ramaiah, N., Jyothibabu, R., Fernandes, V., Paul, J. T., and Prasanna Kumar, S.: Comparative accounts of biological productivity characteristics and estimates of carbon fluxes in the Arabian Sea and the Bay of Bengal, Deep-Sea Res. Pt. II, 52, 2003–2017, https://doi.org/10.1016/j.dsr2.2005.05.009, 2005.

Greaser, S. R., Subrahmanyam, B., Trott, C. B., and Roman-Stork, H. L.: Interactions Between Mesoscale Eddies and Synoptic Oscillations in the Bay of Bengal During the Strong Monsoon of 2019, J. Geophys. Res.-Oceans, 125, e2020JC016772, https://doi.org/10.1029/2020JC016772, 2020.

Gregg, W. W. and Rousseaux, C. S.: Global ocean primary production trends in the modern ocean color satellite record (1998–2015), Environ. Res. Lett., 14, 124011, https://doi.org/10.1088/1748-9326/ab4667, 2019.

Griffies, S. M. and Hallberg, R. W.: Biharmonic friction with a Smagorinsky-like viscosity for use in large-scale eddy-permitting ocean models, Monthly Weather Review, 128, 2935–2946, https://doi.org/10.1175/1520-0493(2000)128<2935:BFWASL>2.0.CO;2, 2000.

Grimaldi, S., Salamon, P., Disperati, J., Zsoter, E., Russo, C., Ramos, A., Carton De Wiart, C., Barnard, C., Hansford, E., Gomes, G., and Prudhomme, C.: River discharge and related historical data from the Global Flood Awareness System, v4.0, CDS, https://doi.org/10.24381/CDS.A4FDD6B9, 2022.

Gutknecht, E., Reffray, G., Gehlen, M., Triyulianti, I., Berlianty, D., and Gaspar, P.: Evaluation of an operational ocean model configuration at $1/12^\circ$ spatial resolution for the Indonesian seas (NEMO2.3/INDO12) – Part 2: Biogeochemistry, Geosci. Model Dev., 9, 1523–1543, https://doi.org/10.5194/gmd-9-1523-2016, 2016.

Hallberg, R.: Using a resolution function to regulate parameterizations of oceanic mesoscale eddy effects, Ocean Model., 72, 92–103, https://doi.org/10.1016/j.ocemod.2013.08.007, 2013.

Hallberg, R. and Adcroft, A.: Reconciling estimates of the free surface height in Lagrangian vertical coordinate ocean models with mode-split time stepping, Ocean Model., 29, 15–26, https://doi.org/10.1016/j.ocemod.2009.02.008, 2009.

Harrigan, S., Zsoter, E., Alfieri, L., Prudhomme, C., Salamon, P., Wetterhall, F., Barnard, C., Cloke, H., and Pappenberger, F.: GloFAS-ERA5 operational global river discharge reanalysis 1979–present, Earth Syst. Sci. Data, 12, 2043–2060, https://doi.org/10.5194/essd-12-2043-2020, 2020.

Harrigan, S., Zsoter, E., Cloke, H., Salamon, P., and Prudhomme, C.: Daily ensemble river discharge reforecasts and real-time forecasts from the operational Global Flood Awareness System, Hydrol. Earth Syst. Sci., 27, 1–19, https://doi.org/10.5194/hess-27-1-2023, 2023.

Helm, K. P., Bindoff, N. L., and Church, J. A.: Observed decreases in oxygen content of the global ocean, Geophys. Res. Lett., 38, L23602, https://doi.org/10.1029/2011GL049513, 2011.

Herbert, R. J., Krom, M. D., Carslaw, K. S., Stockdale, A., Mortimer, R. J. G., Benning, L. G., Pringle, K., and Browse, J.: The Effect of Atmospheric Acid Processing on the Global Deposition of Bioavailable Phosphorus From Dust, Global Biogeochem. Cy., 32, 1367–1385, https://doi.org/10.1029/2018GB005880, 2018.

Hersbach, H., Bell, B., Berrisford, P., Hirahara, S., Horányi, A., Muñoz-Sabater, J., Nicolas, J., Peubey, C., Radu, R., Schepers, D., Simmons, A., Soci, C., Abdalla, S., Abellan, X., Balsamo, G., Bechtold, P., Biavati, G., Bidlot, J., Bonavita, M., De Chiara, G., Dahlgren, P., Dee, D., Diamantakis, M., Dragani, R., Flemming, J., Forbes, R., Fuentes, M., Geer, A., Haimberger, L., Healy, S., Hogan, R. J., Hólm, E., Janisková, M., Keeley, S., Laloyaux, P., Lopez, P., Lupu, C., Radnoti, G., de Rosnay, P., Rozum, I., Vamborg, F., Villaume, S., and Thépaut, J.-N.: The ERA5 global reanalysis, Q. J. Roy. Meteorol. Soc., 146, 1999–2049, https://doi.org/10.1002/qj.3803, 2020.

Hong, C.-C., Li, T., LinHo, and Kug, J.-S.: Asymmetry of the Indian Ocean Dipole. Part I: Observational Analysis, J. Climate, 21, 4834–4848, https://doi.org/10.1175/2008JCLI2222.1, 2008a.

Hong, C.-C., Li, T., and Luo, J.-J.: Asymmetry of the Indian Ocean Dipole. Part II: Model Diagnosis, J. Climate, 21, 4849–4858, https://doi.org/10.1175/2008JCLI2223.1, 2008b.

Horowitz, L. W., Naik, V., Paulot, F., Ginoux, P. A., Dunne, J. P., Mao, J., Schnell, J., Chen, X., He, J., John, J. G., Lin, M., Lin, P., Malyshev, S., Paynter, D., Shevliakova, E., and Zhao, M.: The GFDL Global Atmospheric Chemistry–Climate Model AM4.1: Model Description and Simulation Characteristics, J. Adv. Model. Earth Syst., 12, e2019MS002032, https://doi.org/10.1029/2019MS002032, 2020.

Irazoqui Apecechea, M., Verlaan, M., Zijl, F., Le Coz, C., and Kernkamp, H.: Effects of self-attraction and loading at a regional scale: a test case for the Northwest European Shelf, Ocean Dynam., 67, 729–749, https://doi.org/10.1007/s10236-017-1053-4, 2017.

Ito, T., Minobe, S., Long, M. C., and Deutsch, C.: Upper ocean O_2 trends: 1958–2015, Geophys. Res. Lett., 44, 4214–4223, https://doi.org/10.1002/2017GL073613, 2017.

Jackson, L., Hallberg, R., and Legg, S.: A Parameterization of Shear-Driven Turbulence for Ocean Climate Models, J. Phys. Oceanogr., 38, 1033–1053, https://doi.org/10.1175/2007JPO3779.1, 2008.

Jebri, F., Jacobs, Z. L., Raitsos, D. E., Srokosz, M., Painter, S. C., Kelly, S., Roberts, M. J., Scott, L., Taylor, S. F. W., Palmer, M., Kizenga, H., Shaghude, Y., Wihsgott, J., and Popova, E.: Interannual monsoon wind variability as a key driver of East African small pelagic fisheries, Sci. Rep., 10, 13247, https://doi.org/10.1038/s41598-020-70275-9, 2020.

Jian, J., Webster, P. J., and Hoyos, C. D.: Large-scale controls on Ganges and Brahmaputra river discharge on intraseasonal and seasonal time-scales, Q. J. Roy. Meteorol. Soc., 135, 353–370, https://doi.org/10.1002/qj.384, 2009.

Jiao, X., Zhou, J., Hu, M., Wang, M., Wu, H., Wu, K., and Chen, D.: Evaluation of three prevalent global riverine nutrient transport models, Environ. Sci. Pollut. Res., 30, 122875–122885, https://doi.org/10.1007/s11356-023-31041-2, 2023.

Kalita, R. and Lotliker, A. A.: Assessment of satellite-based Net Primary Productivity models in different biogeochemical provinces over the northern Indian Ocean, Int. J. Remote Sens., 1–20, https://doi.org/10.1080/01431161.2023.2247533, 2023.

Kobayashi, S., Ota, Y., Harada, Y., Ebita, A., Moriya, M., Onoda, H., Onogi, K., Kamahori, H., Kobayashi, C., Endo, H., Miyaoka, K., and Takahashi, K.: The JRA-55 Reanalysis: General Specifications and Basic Characteristics, J. Meteorol. Soc. Jpn. Ser. II, 93, 5–48, https://doi.org/10.2151/jmsj.2015-001, 2015.

Krishna, M., Prasad, M., Rao, D., Viswanadham, R., Sarma, V., and Reddy, N.: Export of dissolved inorganic nutrients to the northern Indian Ocean from the Indian monsoonal rivers during discharge period, Geochim. Cosmochim. Ac., 172, 430–443, https://doi.org/10.1016/j.gca.2015.10.013, 2016.

Kumar, S., Ramesh, R., Sardesai, S., and Sheshshayee, M. S.: High new production in the Bay of Bengal: Possible causes

and implications, Geophys. Res. Lett., 31, 2004GL021005, https://doi.org/10.1029/2004GL021005, 2004.

Kumar, S., Ramesh, R., Dwivedi, R. M., Raman, M., Sheshshayee, M. S., and D'Souza, W.: Nitrogen Uptake in the Northeastern Arabian Sea during Winter Cooling, Int. J. Oceanogr., 2010, 1–11, https://doi.org/10.1155/2010/819029, 2010.

Kwiatkowski, L., Bopp, L., Aumont, O., Ciais, P., Cox, P. M., Laufötter, C., Li, Y., and Séférian, R.: Emergent constraints on projections of declining primary production in the tropical oceans, Nat. Clim. Change, 7, 355–358, https://doi.org/10.1038/nclimate3265, 2017.

Kwiatkowski, L., Torres, O., Bopp, L., Aumont, O., Chamberlain, M., Christian, J. R., Dunne, J. P., Gehlen, M., Ilyina, T., John, J. G., Lenton, A., Li, H., Lovenduski, N. S., Orr, J. C., Palmieri, J., Santana-Falcón, Y., Schwinger, J., Séférian, R., Stock, C. A., Tagliabue, A., Takano, Y., Tjiputra, J., Toyama, K., Tsujino, H., Watanabe, M., Yamamoto, A., Yool, A., and Ziehn, T.: Twenty-first century ocean warming, acidification, deoxygenation, and upper-ocean nutrient and primary production decline from CMIP6 model projections, Biogeosciences, 17, 3439–3470, https://doi.org/10.5194/bg-17-3439-2020, 2020.

Lachkar, Z., Smith, S., Lévy, M., and Pauluis, O.: Eddies reduce denitrification and compress habitats in the Arabian Sea, Geophys.Res. Lett., 43, 9148–9156, https://doi.org/10.1002/2016GL069876, 2016.

Lachkar, Z., Lévy, M., and Smith, S.: Intensification and deepening of the Arabian Sea oxygen minimum zone in response to increase in Indian monsoon wind intensity, Biogeosciences, 15, 159–186, https://doi.org/10.5194/bg-15-159-2018, 2018.

Lachkar, Z., Lévy, M., and Smith, K. S.: Strong Intensification of the Arabian Sea Oxygen Minimum Zone in Response to Arabian Gulf Warming, Geophys. Res. Lett., 46, 5420–5429,https://doi.org/10.1029/2018GL081631, 2019.

Lachkar, Z., Lévy, M., Hailegeorgis, D., and Vallivattathillam, P.: Differences in recent and future trends in the Arabian Sea oxygen minimum zone: processes and uncertainties, Front. Mar. Sci., 10, https://doi.org/10.3389/fmars.2023.1122043, 2023.

Large, W. G. and Yeager, S. G.: Diurnal to Decadal Global Forcing For Ocean and Sea-Ice Models: The Data Sets and Flux Climatologies, Technical report, National Center for Atmospheric Research, https://doi.org/10.5065/D6KK98Q6, a, b, 2004.

LaRowe, D. E., Arndt, S., Bradley, J. A., Burwicz, E., Dale, A. W., and Amend, J. P.: Organic carbon and microbial activity in marine sediments on a global scale throughout the Quaternary, Geochim. Cosmochim. Ac., 286, 227–247, https://doi.org/10.1016/j.gca.2020.07.017, 2020.

Legg, S., Hallberg, R. W., and Girton, J. B.: Comparison of entrainment in overflows simulated by z-coordinate, isopycnal and non-hydrostatic models, Ocean Model., 11, 69–97, https://doi.org/10.1016/j.ocemod.2004.11.006, 2006.

Léy, M., Shankar, D., André, J.-M., Shenoi, S. S. C., Durand, F., and de Boyer Montégut, C.: Basin-wide seasonal evolution of the Indian Ocean's phytoplankton blooms, J. Geophys. Res., 112, https://doi.org/10.1029/2007JC004090, 2007.

Lévy, M., Resplandy, L., Palter, J. B., Couespel, D., and Lachkar, Z.: The crucial contribution of mixing to present and future ocean oxygen distribution, in: Ocean Mixing, Elsevier, 329–344, ISBN 978-0-12-821512-8, https://doi.org/10.1016/B978-0-12-821512-8.00020-7, 2022.

Li, G., Xie, S.-P., and Du, Y.: A Robust but Spurious Pattern of Climate Change in Model Projections over the Tropical Indian Ocean, J. Climate, 29, 5589–5608, https://doi.org/10.1175/JCLI-D-15-0565.1, 2016.

Li, Z., Huang, S., Zhu, X., Sun, Z., Long, Y., and Xie, H.: Short-term offshore extension of Brahmaputra-Ganges and Irrawaddy freshwater plumes to the central northern Bay of Bengal based on in situ and satellite observations, Acta Oceanolog. Sin., 40, 80–93, https://doi.org/10.1007/s13131-021-1729-y, 2021.

Liao, E., Resplandy, L., Liu, J., and Bowman, K. W.: Amplification of the Ocean Carbon Sink During El Niños: Role of Poleward Ekman Transport and Influence on Atmospheric CO_2, Global Biogeochem. Cy., 34, e2020GB006574, https://doi.org/10.1029/2020GB006574, 2020.

Liao, E., Resplandy, L., Yang, F., Zhao, Y., Ditkovsky, S., Malsang, M., Pearson, J., Ross, A. C., Hallberg, R., and Stock, C.: Model source code for "A high-resolution physical-biogeochemical model for marine resource applications in the Northern Indian Ocean (MOM6-COBALT-IND12)", Zenodo [code], https://doi.org/10.5281/ZENODO.14184011, 2024a.

Liao, E., Resplandy, L., Yang, F., Zhao, Y., Ditkovsky, S., Malsang, M., Pearson, J., Ross, A. C., Hallberg, R., and Stock, C.: Model input for "A high-resolution physical-biogeochemical model for marine resource applications in the Northern Indian Ocean (MOM6-COBALT-IND12)", Zenodo [data set], https://doi.org/10.5281/ZENODO.14171404, 2024b.

Locarnini, R. A., Mishonov, A. V., Antonov, J. I., Boyer, T. P., Garcia, H. E., Baranova, O. K., Zweng, M. M., Paver, C., Reagan, J. R., Johnson, D. R., Hamilton, M. A., and Seidov, D.: World Ocean Atlas 2013, in: Volume 1: Temperature, Tech. rep., Technical Edn., NOAA Atlas NESDIS 73, edited by: Levitus, S. and Mishonov,A., NOAA, 40 pp., https://doi.org/10.7289/V55X26VD, 2014.

Lopez, A.: Sea level daily gridded data from satellite observations for the global ocean from 1993 to present, CDS, https://doi.org/10.24381/CDS.4C328C78, 2018.

Löscher, C. R.: Reviews and syntheses: Trends in primary production in the Bay of Bengal – is it at a tipping point?, Biogeosciences, 18, 4953–4963, https://doi.org/10.5194/bg-18-4953-2021, 2021.

Löscher, C. R., Mohr, W., Bange, H. W., and Canfield, D. E.: No nitrogen fixation in the Bay of Bengal?, Biogeosciences, 17, 851–864, https://doi.org/10.5194/bg-17-851-2020, 2020.

Luo, J. Y., Stock, C. A., Dunne, J. P., Saba, G. K., and Cook, L.: Ocean Biogeochemical Fingerprints of Fast-Sinking Tunicate and Fish Detritus, Geophys. Res. Lett., 51, e2023GL107052, https://doi.org/10.1029/2023GL107052, 2024.

Mahadevan, A.: The Impact of Submesoscale Physics on Primary Productivity of Plankton, Annu. Rev. Mar. Sci., 8, 161–184, https://doi.org/10.1146/annurev-marine-010814-015912, 2016.

Malsang, M., Resplandy, L., Bopp, L., Zhao, Y., Ditkovsky, S., Yang, F., Paulot, F., and Lévy, M.: Contemporary decline in northern Indian Ocean primary production weakly offset by rising atmospheric nitrogen deposition, Front. Mar. Sci., 11, https://doi.org/10.3389/fmars.2024.1418634, 2024.

Manizza, M.: Bio-optical feedbacks among phytoplankton, upper ocean physics and sea-ice in a global model, Geophys. Res. Lett., 32, L05603, https://doi.org/10.1029/2004GL020778, 2005.

Marchesiello, P., McWilliams, J. C., and Shchepetkin, A.: Open boundary conditions for long-term integration of regional oceanic models, Ocean Model., 3, 1–20, https://doi.org/10.1016/S1463-5003(00)00013-5, 2001.

Marra, J. F., Barber, R. T., Barber, E., Bidigare, R. R., Chamberlin, W. S., Goericke, R., Hargreaves, B. R., Hiscock, M., Iturriaga, R., Johnson, Z. I., Kiefer, D. A., Kinkade, C., Knudson, C., Lance, V., Langdon, C., Lee, Z., Perry, M. J., Smith, W. O., Vaillancourt, R., and Zoffoli, L.: A database of ocean primary productivity from the ^{14}C method, Limnol. Oceanogr. Lett., 6, 107–111, https://doi.org/10.1002/lol2.10175, 2021.

Mayorga, E., Seitzinger, S. P., Harrison, J. A., Dumont, E., Beusen, A. H., Bouwman, A., Fekete, B. M., Kroeze, C., and Van Drecht, G.: Global Nutrient Export from WaterSheds 2 (NEWS 2): Model development and implementation, Environ. Model. Softw., 25, 837–853, https://doi.org/10.1016/j.envsoft.2010.01.007, 2010.

McCarthy, J. J., Garside, C., and Nevins, J. L.: Nitrogen dynamics during the Arabian Sea Northeast Monsoon, Deep-Sea Res. Pt. II, 46, 1623–1664, https://doi.org/10.1016/S0967-0645(99)00038-7, 1999.

McCreary, J. P., Kundu, P. K., and Molinari, R. L.: A numerical investigation of dynamics, thermodynamics and mixed-layer processes in the Indian Ocean, Prog. Oceanogr., 31, 181–244, https://doi.org/10.1016/0079-6611(93)90002-U, 1993.

McCreary, J. P., Yu, Z., Hood, R. R., Vinaychandran, P., Furue, R., Ishida, A., and Richards, K. J.: Dynamics of the Indian-Ocean oxygen minimum zones, Prog. Oceanogr., 112-113, 15–37, https://doi.org/10.1016/j.pocean.2013.03.002, 2013.

McPhaden, M. J., Meyers, G., Ando, K., Masumoto, Y., Murty, V. S. N., Ravichandran, M., Syamsudin, F., Vialard, J., Yu, L., and Yu, W.: RAMA: The Research Moored Array for African–Asian–Australian Monsoon Analysis and Prediction, B. Am. Meteorol. Soc., 90, 459–480, https://doi.org/10.1175/2008BAMS2608.1, 2009.

Mears, C., Lee, T., Ricciardulli, L., Wang, X., and Wentz, F.: RSS Cross-Calibrated Multi-Platform (CCMP) monthly ocean vector wind analysis on 0.25 deg grid, Version 3.0, Remote Sensing Systems, https://doi.org/10.56236/RSS-uv1m30, 2022.

Measures, C. and Vink, S.: Seasonal variations in the distribution of Fe and Al in the surface waters of the Arabian Sea, Deep-Sea Res. Pt. II, 46, 1597–1622, https://doi.org/10.1016/S0967-0645(99)00037-5, 1999.

Milliman, J. D. and Farnsworth, K. L.: River Discharge to the Coastal Ocean: A Global Synthesis, in: 1st Edn., Cambridge University Press, ISBN 978-0-521-87987-3, https://doi.org/10.1017/CBO9780511781247, 2011.

Moffett, J. W. and Landry, M. R.: Grazing control and iron limitation of primary production in the Arabian Sea: Implications for anticipated shifts in Southwest Monsoon intensity, Deep-Sea Res. Pt. II, 179, 104687, https://doi.org/10.1016/j.dsr2.2019.104687, 2020.

Moffett, J. W., Vedamati, J., Goepfert, T. J., Pratihary, A., Gauns, M., and Naqvi, S. W. A.: Biogeochemistry of iron in the Arabian Sea: Biogeochemistry of iron in the Arabian Sea, Limnol. Oceanogr., 60, 1671–1688, https://doi.org/10.1002/lno.10132, 2015.

Murtugudde, R. and Busalacchi, A. J.: Interannual variability of the dynamics and thermodynamics of the tropical Indian Ocean, J. Climate, 12, 2300–2326, https://doi.org/10.1175/1520-0442(1999)012<2300:IVOTDA>2.0.CO;2, 1999.

Nagura, M. and McPhaden, M. J.: The Shallow Overturning Circulation in the Indian Ocean, J. Phys. Oceanogr., 48, 413–434, https://doi.org/10.1175/JPO-D-17-0127.1, 2018.

Nakazato, M., Kido, S., and Tozuka, T.: Mechanisms of asymmetry in sea surface temperature anomalies associated with the Indian Ocean Dipole revealed by closed heat budget, Sci. Rep., 11, 22546, https://doi.org/10.1038/s41598-021-01619-2, 2021.

Naqvi, S. W.: Anoxia-Related Biogeochemistry of North Indian Ocean, Geochem. Perspect., 169–287, https://doi.org/10.7185/geochempersp.11.2, 2022.

Naqvi, S. W. A.: Evidence for ocean deoxygenation and its patterns: Indian Ocean, in: Ocean deoxygenation: Everyone's problem – Causes, impacts, consequences and solutions, edited by: Laffoley, D. and Baxter, J. M., IUCN, Gland, Switzerland, p. 562, ISBN 978-2-8317-2013-5, 2019.

Naqvi, S. W. A.: Deoxygenation in Marginal Seas of the Indian Ocean, Front. Mar. Sci., 8, 88, https://doi.org/10.3389/fmars.2021.624322, 2021.

Naqvi, S. W. A., Naik, H., Pratihary, A., D'Souza, W., Narvekar, P. V., Jayakumar, D. A., Devol, A. H., Yoshinari, T., and Saino, T.: Coastal versus open-ocean denitrification in the Arabian Sea, Biogeosciences, 3, 621–633, https://doi.org/10.5194/bg-3-621-2006, 2006.

Naqvi, S. W. A., Naik, H., Jayakumar, A., Pratihary, A. K., Narvenkar, G., Kurian, S., Agnihotri, R., Shailaja, M. S., and Narvekar, P. V.: Seasonal Anoxia Over the Western Indian Continental Shelf, in: Indian Ocean Biogeochemical Processes and Ecological Variability, AGU – American Geophysical Union, 333–345, ISBN 978-1-118-66636-4, https://doi.org/10.1029/2008GM000745, 2009.

Naqvi, S. W. A., Moffett, J. W., Gauns, M. U., Narvekar, P. V., Pratihary,A. K., Naik, H., Shenoy, D. M., Jayakumar, D. A., Goepfert, T. J., Patra, P. K., Al-Azri, A., and Ahmed, S. I.: The Arabian Sea as a high-nutrient, low-chlorophyll region during the late Southwest Monsoon, Biogeosciences, 7, 2091–2100, https://doi.org/10.5194/bg-7-2091-2010, 2010.

Nienhaus, M. J., Subrahmanyam, B., and Murty, V. S. N.: Altimetric Observations and Model Simulations of Coastal Kelvin Waves in the Bay of Bengal, Mar. Geod., 35, 190–216, https://doi.org/10.1080/01490419.2012.718607, 2012.

Nuncio, M. and Kumar, S. P.: Life cycle of eddies along the western boundary of the Bay of Bengal and their implications, J. Mar. Syst., 94, 9–17, https://doi.org/10.1016/j.jmarsys.2011.10.002, 2012.

Olsen, A., Key, R. M., van Heuven, S., Lauvset, S. K., Velo, A., Lin, X., Schirnick, C., Kozyr, A., Tanhua, T., Hoppema, M., Jutterström, S., Steinfeldt, R., Jeansson, E., Ishii, M., Pérez, F. F., and Suzuki, T.: The Global Ocean Data Analysis Project version 2 (GLODAPv2) – an internally consistent data product for the world ocean, Earth Syst. Sci. Data, 8, 297–323, https://doi.org/10.5194/essd-8-297-2016, 2016.

Orlanski, I.: A simple boundary condition for unbounded hyperbolic flows, J. Comput. Phys., 21, 251–269, https://doi.org/10.1016/0021-9991(76)90023-1, 1976.

Paulmier, A. and Ruiz-Pino, D.: Oxygen minimum zones (OMZs) in the modern ocean, Prog. Oceanogr., 80, 113–128, https://doi.org/10.1016/j.pocean.2008.08.001, 2009.

Paulot, F., Stock, C., John, J. G., Zadeh, N., and Horowitz, L. W.: Ocean Ammonia Outgassing: Modulation by CO_2 and Anthropogenic Nitrogen Deposition, J. Adv. Model. Earth Syst., 12, e2019MS002026, https://doi.org/10.1029/2019MS002026, 2020.

Pearson, J., Resplandy, L., and Poupon, M.: Coastlines at Risk of Hypoxia From Natural Variability in the Northern Indian Ocean, Global Biogeochem. Cy., 36, https://doi.org/10.1029/2021GB007192, 2022.

Peng, X., Fuchsman, C. A., Jayakumar, A., Warner, M. J., Devol, A. H., and Ward, B. B.: Revisiting nitrification in the Eastern Tropical South Pacific: A focus on controls, J. Geophys. Res.-Oceans, 121, 1667–1684, https://doi.org/10.1002/2015JC011455, 2016.

Phillips, H. E., Tandon, A., Furue, R., Hood, R., Ummenhofer, C. C., Benthuysen, J. A., Menezes, V., Hu, S., Webber, B., Sanchez-Franks, A., Cherian, D., Shroyer, E., Feng, M., Wijesekera, H., Chatterjee, A., Yu, L., Hermes, J., Murtugudde, R., Tozuka, T., Su, D., Singh, A., Centurioni, L., Prakash, S., and Wiggert, J.: Progress in understanding of Indian Ocean circulation, variability, air–sea exchange, and impacts on biogeochemistry, Ocean Sci., 17, 1677–1751, https://doi.org/10.5194/os-17-1677-2021, 2021.

Pinsky, M. L., Worm, B., Fogarty, M. J., Sarmiento, J. L., and Levin, S. A.: Marine Taxa Track Local Climate Velocities, Science, 341, 1239–1242, https://doi.org/10.1126/science.1239352, 2013.

Piontkovski, S. and Al-Oufi, H.: The Omani shelf hypoxia and the warming Arabian Sea, Int. J. Environ. Stud., 72, 256–264, https://doi.org/10.1080/00207233.2015.1012361, 2015.

Polzin, K. L.: An abyssal recipe, Ocean Model., 30, 298–309, https://doi.org/10.1016/j.ocemod.2009.07.006, 2009.

Prakash, S. and Ramesh, R.: Is the Arabian Sea getting more productive?, Current Sci., 92, 667–670, 2007.

Prakash, S., Ramesh, R., Sheshshayee, M. S., Dwivedi, R. M., and Raman, M.: Quantification of new production during a winter *Noctiluca scintillans* bloom in the Arabian Sea, Geophys. Res. Lett., 35, L08604, https://doi.org/10.1029/2008GL033819, 2008.

Prasanna Kumar, S., Nuncio, M., Ramaiah, N., Sardesai, S., Narvekar, J., Fernandes, V., and Paul, J. T.: Eddy-mediated biological productivity in the Bay of Bengal during fall and spring intermonsoons, Deep-Sea Res. Pt. I, 54, 1619–1640, https://doi.org/10.1016/j.dsr.2007.06.002, 2007a.

Prasanna Kumar, S., Sardessai, S., Ramaiah, N., Bhosle, N., Ramaswamy, V., Ramesh, R., Sharada, M., Sarin, M. M., Sarupria, J., and Muraleedharan, U.: Bay of Bengal Process Studies (BOBPS) Final Report, Bay of Bengal process studies, Technical Report, https://drs.nio.res.in/drs/bitstream/2264/535/3/Report_BOBPS_July2006.p.pdf (last access: 1 March 2024), 2007b.

Queste, B. Y., Vic, C., Heywood, K. J., and Piontkovski, S. A.: Physical controls on oxygen distribution and denitrification potential in the north west Arabian Sea, Geophys. Res. Lett., https://doi.org/10.1029/2017GL076666, 2018.

Radhakrishna, K.: Primary productivity of the Bay of Bengal during March–April 1975, Indian J. Mar. Sci., 7, 58–60, 1978.

Rahaman, H., Ravichandran, M., Sengupta, D., Harrison, M. J., and Griffies, S. M.: Development of a regional model for the North Indian Ocean, Ocean Model., 75, 1–19, https://doi.org/10.1016/j.ocemod.2013.12.005, 2014.

Raiswell, R. and Canfield, D. E.: The Iron Biogeochemical Cycle Past and Present, Geochem. Perspect., 1, 1–220, https://doi.org/10.7185/geochempersp.1.1, 2012.

Recknagel, T., Färber, C., Plessow, H., and Looser, U.: The Global Runoff Data Centre: A building block in the chain of reproducible hydrology, EGU General Assembly 2023, Vienna, Austria, 24–28 April 2023, EGU23-15454, https://doi.org/10.5194/egusphere-egu23-15454, 2023.

Reichl, B. G. and Hallberg, R.: A simplified energetics based planetary boundary layer (ePBL) approach for ocean climate simulations, Ocean Model., 132, 112–129, https://doi.org/10.1016/j.ocemod.2018.10.004, 2018.

Reichl, B. G. and Li, Q.: A Parameterization with a Constrained Potential Energy Conversion Rate of Vertical Mixing Due to Langmuir Turbulence, J. Phys. Oceanogr., 49, 2935–2959, https://doi.org/10.1175/JPO-D-18-0258.1, 2019.

Resplandy, L., Lévy, M., Madec, G., Pous, S., Aumont, O., and Kumar, D.: Contribution of mesoscale processes to nutrient budgets in the Arabian Sea, J. Geophys. Res., 116, C11007, https://doi.org/10.1029/2011JC007006, 2011.

Resplandy, L., Lévy, M., Bopp, L., Echevin, V., Pous, S., Sarma, V. V. S. S., and Kumar, D.: Controlling factors of the oxygen balance in the Arabian Sea's OMZ, Biogeosciences, 9, 5095–5109, https://doi.org/10.5194/bg-9-5095-2012, 2012.

Reynolds, R. W., Smith, T. M., Liu, C., Chelton, D. B., Casey, K. S., and Schlax, M. G.: Daily High-Resolution-Blended Analyses for Sea Surface Temperature, J. Climate, 20, 5473–5496, https://doi.org/10.1175/2007JCLI1824.1, 2007.

Rixen, T., Gaye, B., and Emeis, K.-C.: The monsoon, carbon fluxes, and the organic carbon pump in the northern Indian Ocean, Prog. Oceanogr., 175, 24–39, https://doi.org/10.1016/j.pocean.2019.03.001, 2019a.

Rixen, T., Gaye, B., Emeis, K.-C., and Ramaswamy, V.: The ballast effect of lithogenic matter and its influences on the carbon fluxes in the Indian Ocean, Biogeosciences, 16, 485–503, https://doi.org/10.5194/bg-16-485-2019, 2019b.

Rixen, T., Cowie, G., Gaye, B., Goes, J., do Rosário Gomes, H., Hood, R. R., Lachkar, Z., Schmidt, H., Segschneider, J., and Singh, A.: Reviews and syntheses: Present, past, and future of the oxygen minimum zone in the northern Indian Ocean, Biogeosciences, 17, 6051–6080, https://doi.org/10.5194/bg-17-6051-2020, 2020.

Roemmich, D. and Gilson, J.: The 2004–2008 mean and annual cycle of temperature, salinity, and steric height in the global ocean from the Argo Program, Prog. Oceanogr., 82, 81–100, https://doi.org/10.1016/j.pocean.2009.03.004, 2009.

Ross, A. C., Stock, C. A., Adcroft, A., Curchitser, E., Hallberg, R., Harrison, M. J., Hedstrom, K., Zadeh, N., Alexander, M., Chen, W., Drenkard, E. J., Du Pontavice, H., Dussin, R., Gomez, F., John, J. G., Kang, D., Lavoie, D., Resplandy, L., Roobaert, A., Saba, V., Shin, S.-I., Siedlecki, S., and Simkins, J.: A high-resolution physical–biogeochemical model for marine resource applications in the northwest Atlantic (MOM6-COBALT-NWA12 v1.0), Geosci. Model Dev., 16, 6943–6985, https://doi.org/10.5194/gmd-16-6943-2023, 2023.

Roxy, M. K., Gnanaseelan, C., Parekh, A., Chowdary, J. S., Singh, S., Modi, A., Kakatkar, R., Mohapatra, S., Dhara, C., Shenoi, S. C., and Rajeevan, M.: Indian Ocean Warming, in: Assessment of Climate Change over the Indian Region: A Report of

the Ministry of Earth Sciences (MoES), Government of India, edited by: Krishnan, R., Sanjay, J., Gnanaseelan, C., Mujumdar, M., Kulkarni, A., and Chakraborty, S., Springer, Singapore, 191–206, ISBN 9789811543272, https://doi.org/10.1007/978-981-15-4327-2_10, 2020.

Roy, A.: Blue Economy in the Indian Ocean: Governance Perspectives for Sustainable Development in the Region, Occasional Paper No. 181, ORF – Observer Research Foundation, https://www.orfonline.org/public/uploads/posts/pdf/20230726014058.pdf (last access: 1 March 2024), 2019.

Saji, N. H., Goswami, B. N., Vinayachandran, P. N., and Yamagata, T.: A dipole mode in the tropical Indian Ocean, Nature, 401, 360–363, https://doi.org/10.1038/43854, 1999.

Sarma, V. and Aswanikumar, V.: Subsurface chlorophyll maxima in the north-western Bay of Bengal, J. Plankt. Res., 13, 339–352, https://doi.org/10.1093/plankt/13.2.339, 1991.

Sarma, V. and Dalabehera, H.: New and primary production in the western Indian Ocean during fall monsoon, Mar. Chem., 215, 103687, https://doi.org/10.1016/j.marchem.2019.103687, 2019.

Sarma, V., Chopra, M., Rao, D., Priya, M., Rajula, G., Lakshmi, D., and Rao, V.: Role of eddies on controlling total and size-fractionated primary production in the Bay of Bengal, Cont. Shelf Res., 204, 104186, https://doi.org/10.1016/j.csr.2020.104186, 2020.

Sathyendranath, S., Brewin, R., Brockmann, C., Brotas, V., Calton, B., Chuprin, A., Cipollini, P., Couto, A., Dingle, J., Doerffer, R., Donlon, C., Dowell, M., Farman, A., Grant, M., Groom, S., Horseman, A., Jackson, T., Krasemann, H., Lavender, S., Martinez-Vicente, V., Mazeran, C., Mélin, F., Moore, T., Müller, D., Regner, P., Roy, S., Steele, C., Steinmetz, F., Swinton, J., Taberner, M., Thompson, A., Valente, A., Zühlke, M., Brando, V., Feng, H., Feldman, G., Franz, B., Frouin, R., Gould, R., Hooker, S., Kahru, M., Kratzer, S., Mitchell, B., Muller-Karger, F., Sosik, H., Voss, K., Werdell, J., and Platt, T.: An Ocean-Colour Time Series for Use in Climate Studies: The Experience of the Ocean-Colour Climate Change Initiative (OC-CCI), Sensors, 19, 4285, https://doi.org/10.3390/s19194285, 2019.

Savidge, G. and Gilpin, L.: Seasonal influences on size-fractionated chlorophyll a concentrations and primary production in the north-west Indian Ocean, Deep-Sea Res. Pt. II, 46, 701–723, https://doi.org/10.1016/S0967-0645(98)00124-6, 1999.

Saxena, H., Sahoo, D., Nazirahmed, S., Chaudhari, D., Rahi, P., Kumar, S., Benavides, M., Krishna, A. V., Sudheer, A. K., and Singh, A.: The Bay of Bengal: An Enigmatic Diazotrophic Niche, J. Geophys. Res.-Biogeo., 128, e2023JG007687, https://doi.org/10.1029/2023JG007687, 2023.

Schmidt, H., Getzlaff, J., Löptien, U., and Oschlies, A.: Causes of uncertainties in the representation of the Arabian Sea oxygen minimum zone in CMIP5 models, Ocean Sci., 17, 1303–1320, https://doi.org/10.5194/os-17-1303-2021, 2021.

Schmidt, M. and Eggert, A.: Oxygen cycling in the northern Benguela Upwelling System: Modelling oxygen sources and sinks, Prog. Oceanogr., 149, 145–173, https://doi.org/10.1016/j.pocean.2016.09.004, 2016.

Schofield, O., Arnone, R., Bissett, P., Dickey, T., Davis, C., Finkel, Z., Oliver, M., and Moline, M.: Watercolors in the Coastal Zone: What Can We See?, Oceanography, 17, 24–31, https://doi.org/10.5670/oceanog.2004.44, 2004.

Schott, F. A. and McCreary, J. P.: The monsoon circulation of the Indian Ocean, Prog. Oceanogr., 51, 1–123, 2001.

Schott, F. A., Mccreary, J. P., and Johnson, G. C.: Shallow Overturning Circulations of the Tropical-Subtropical Oceans, Geophys. Monogr. Ser., 261–304, https://doi.org/10.1029/147GM15, 2004.

Séférian, R., Berthet, S., Yool, A., Palmiéri, J., Bopp, L., Tagliabue, A., Kwiatkowski, L., Aumont, O., Christian, J., Dunne, J., Gehlen, M., Ilyina, T., John, J. G., Li, H., Long, M. C., Luo, J. Y., Nakano, H., Romanou, A., Schwinger, J., Stock, C., Santana-Falcón, Y., Takano, Y., Tjiputra, J., Tsujino, H., Watanabe, M., Wu, T., Wu, F., and Yamamoto, A.: Tracking Improvement in Simulated Marine Biogeochemistry Between CMIP5 and CMIP6, Curr. Clim. Change Rep., 6, 95–119, https://doi.org/10.1007/s40641-020-00160-0, 2020.

Sengupta, D., Senan, R., and Goswami, B. N.: Origin of intraseasonal variability of circulation in the tropical central Indian Ocean, Geophys. Res. Lett., 28, 1267–1270, https://doi.org/10.1029/2000GL012251, 2001.

Sengupta, D., Senan, R., Goswami, B. N., and Vialard, J.: Intraseasonal Variability of Equatorial Indian Ocean Zonal Currents, J. Climate, 20, 3036–3055, https://doi.org/10.1175/JCLI4166.1, 2007.

Shankar, D. and Shetye, S. R.: On the dynamics of the Lakshadweep high and low in the southeastern Arabian Sea, J. Geophys. Res.-Oceans, 102, 12551–12562, https://doi.org/10.1029/97JC00465, 1997.

Sharma, S., Ha, K.-J., Yamaguchi, R., Rodgers, K. B., Timmermann, A., and Chung, E.-S.: Future Indian Ocean warming patterns, Nat. Commun., 14, 1789, https://doi.org/10.1038/s41467-023-37435-7, 2023.

Shenoi, S. S. C., Shankar, D., and Shetye, S. R.: Differences in heat budgets of the near-surface Arabian Sea and Bay of Bengal: Implications for the summer monsoon, J. Geophys. Res.=Oceans, 107, 5-1–5-14, https://doi.org/10.1029/2000JC000679, 2002.

Shetye, S. R., Shenoi, S. S. C., Gouveia, A. D., Michael, G. S., Sundar, D., and Nampoothiri, G.: Wind-driven coastal upwelling along the western boundary of the Bay of Bengal during the southwest monsoon, Cont. Shelf Res., 11, 1397–1408, https://doi.org/10.1016/0278-4343(91)90042-5, 1991.

Silsbe, G. M., Behrenfeld, M. J., Halsey, K. H., Milligan, A. J., and Westberry, T. K.: The CAFE model: A net production model for global ocean phytoplankton, Global Biogeochem. Cy., 30, 1756–1777, https://doi.org/10.1002/2016GB005521, 2016.

Singh, D., Ghosh, S., Roxy, M. K., and McDermid, S.: Indian summer monsoon: Extreme events, historical changes, and role of anthropogenic forcings, WIREs Clim. Change, 10, e571, https://doi.org/10.1002/wcc.571, 2019.

Siswanto, E., Sarker, M. L. R., Peter, B. N., Takemura, T., Horii, T., Matsumoto, K., Taketani, F., and Honda, M. C.: Variations of phytoplankton chlorophyll in the Bay of Bengal: Impact of climate changes and nutrients from different sources, Front. Mar. Sci., 10, 1052286, https://doi.org/10.3389/fmars.2023.1052286, 2023.

Sofianos, S. S., Johns, W. E., and Murray, S. P.: Heat and freshwater budgets in the Red Sea from direct observations at Bab el Mandeb, Deep-Sea Res. Pt. II, 49, 1323–1340, https://doi.org/10.1016/S0967-0645(01)00164-3, 2002.

Sooraj, K. P., Terray, P., and Mujumdar, M.: Global warming and the weakening of the Asian summer monsoon circulation: as-

sessments from the CMIP5 models, Clim. Dynam., 45, 233–252, https://doi.org/10.1007/s00382-014-2257-7, 2015.

Sprintall, J., Wijffels, S. E., Molcard, R., and Jaya, I.: Direct estimates of the Indonesian Throughflow entering the Indian Ocean: 2004–2006, J. Geophys. Res.-Oceans, 114, https://doi.org/10.1029/2008JC005257, 2009.

Sridevi, B., Sabira, S., and Sarma, V.: Impact of ocean warming on net primary production in the northern Indian Ocean: role of aerosols and freshening of surface ocean, Environ. Sci. Pollut. Res., 30, 53616–53634, https://doi.org/10.1007/s11356-023-26001-9, 2023.

Steele, M., Morley, R., and Ermold, W.: PHC: A Global Ocean Hydrography with a High-Quality Arctic Ocean, J. Climate, 14, 2079–2087, https://doi.org/10.1175/1520-0442(2001)014<2079:PAGOHW>2.0.CO;2, 2001.

Stepanov, V. N. and Hughes, C. W.: Parameterization of ocean self-attraction and loading in numerical models of the ocean circulation, J. Geophys. Res.-Oceans, 109, 2003JC002034, https://doi.org/10.1029/2003JC002034, 2004.

St. Laurent, L. C., Simmons, H. L., and Jayne, S. R.: Estimating tidally driven mixing in the deep ocean: Estimating tidally driven mixing, Geophys. Res. Lett., 29, 21-1–21-4, https://doi.org/10.1029/2002GL015633, 2002.

Stock, C. A., Dunne, J. P., and John, J. G.: Global-scale carbon and energy flows through the marine planktonic food web: An analysis with a coupled physical-biological model, Prog. Oceanogr., 120, 1–28, https://doi.org/10.1016/j.pocean.2013.07.001, 2014.

Stock, C. A., Dunne, J. P., Fan, S., Ginoux, P., John, J., Krasting, J. P., Laufkötter, C., Paulot, F., and Zadeh, N.: Ocean Biogeochemistry in GFDL's Earth System Model 4.1 and Its Response to Increasing Atmospheric CO_2, J. Adv. Model. Earth Syst., 12, e2019MS002043, https://doi.org/10.1029/2019MS002043, 2020.

Stock, C. A., Dunne, J. P., Luo, J. Y., Ross, A. C., Van Oostende, N., Zadeh, N., Cordero, T. J., Liu, X., and Teng, Y.-C.: Photoacclimation and Photoadaptation Sensitivity in a Global Ocean Ecosystem Model, J. Adv. Model. Earth Syst., 17, e2024MS004701, https://doi.org/10.1029/2024MS004701, 2025.

Sunanda, N., Kuttippurath, J., Peter, R., Chakraborty, K., and Chakraborty, A.: Long-Term Trends and Impact of SARS-CoV-2 COVID-19 Lockdown on the Primary Productivity of the North Indian Ocean, Front. Mar. Sci., 8, https://doi.org/10.3389/fmars.2021.669415, 2021.

Sunanda, N., Kuttippurath, J., Chakraborty, A., and Peter, R.: Stressors of primary productivity in the north Indian ocean revealed by satellite, reanalysis and CMIP6 data, Prog. Oceanogr., 219, 103164, https://doi.org/10.1016/j.pocean.2023.103164, 2023.

Sunanda, N., Kuttippurath, J., Peter, R., and Chakraborty, A.: An atmosphere–ocean coupled model for simulating physical and biogeochemical state of north Indian Ocean: Customisation and validation, Ocean Model., 191, 102419, https://doi.org/10.1016/j.ocemod.2024.102419, 2024.

Suresh, I., Vialard, J., Lengaigne, M., Izumo, T., Parvathi, V., and Muraleedharan, P. M.: Sea Level Interannual Variability Along the West Coast of India, Geophys. Res. Lett., 45, https://doi.org/10.1029/2018GL080972, 2018.

Tseng, Y.-h., Bryan, F. O., and Whitney, M. M.: Impacts of the representation of riverine freshwater input in the community earth system model, Ocean Model., 105, 71–86, https://doi.org/10.1016/j.ocemod.2016.08.002, 2016.

Tsujino, H., Urakawa, S., Nakano, H., Small, R. J., Kim, W. M., Yeager, S. G., Danabasoglu, G., Suzuki, T., Bamber, J. L., Bentsen, M., Böning, C. W., Bozec, A., Chassignet, E. P., Curchitser, E., Boeira Dias, F., Durack, P. J., Griffies, S. M., Harada, Y., Ilicak, M., Josey, S. A., Kobayashi, C., Kobayashi, S., Komuro, Y., Large, W. G., Le Sommer, J., Marsland, S. J., Masina, S., Scheinert, M., Tomita, H., Valdivieso, M., and Yamazaki, D.: JRA-55 based surface dataset for driving ocean-sea-ice models (JRA55-do), Ocean Model., 130, 79–139, https://doi.org/10.1016/j.ocemod.2018.07.002, 2018.

Twining, B. S., Rauschenberg, S., Baer, S. E., Lomas, M. W., Martiny, A. C., and Antipova, O.: A nutrient limitation mosaic in the eastern tropical Indian Ocean, Deep-Sea Res. Pt. II, 166, 125–140, https://doi.org/10.1016/j.dsr2.2019.05.001, 2019.

Udaya Bhaskar, T. V. S., Sarma, V. V. S. S., and Pavan Kumar, J.: Potential mechanisms responsible for spatial variability in intensity and thickness of oxygen minimum zone in the Bay of Bengal, J. Geophys. Res.-Biogeo., 126, e2021JG006341, https://doi.org/10.1029/2021JG006341, 2021.

Vallivattathillam, P., Iyyappan, S., Lengaigne, M., Ethé, C., Vialard, J., Levy, M., Suresh, N., Aumont, O., Resplandy, L., Naik, H., and Naqvi, W.: Positive Indian Ocean Dipole events prevent anoxia off the west coast of India, Biogeosciences, 14, 1541–1559, https://doi.org/10.5194/bg-14-1541-2017, 2017.

Veldhuis, M. J., Kraay, G. W., Van Bleijswijk, J. D., and Baars, M. A.: Seasonal and spatial variability in phytoplankton biomass, productivity and growth in the northwestern Indian Ocean: the southwest and northeast monsoon, 1992–1993, Deep-Sea Res. Pt. I, 44, 425–449, https://doi.org/10.1016/S0967-0637(96)00116-1, 1997.

Vialard, J., Shenoi, S. S. C., McCreary, J. P., Shankar, D., Durand, F., Fernando, V., and Shetye, S. R.: Intraseasonal response of the northern Indian Ocean coastal waveguide to the Madden-Julian Oscillation, Geophys. Res. Lett., 36, 2009GL038450, https://doi.org/10.1029/2009GL038450, 2009.

Vic, C., Roullet, G., Carton, X., and Capet, X.: Mesoscale dynamics in the Arabian Sea and a focus on the Great Whirl life cycle: A numerical investigation using ROMS, J. Geophys. Res.-Oceans, 119, 6422–6443, https://doi.org/10.1002/2014JC009857, 2014.

Vinayachandran, P. N. M., Masumoto, Y., Roberts, M. J., Huggett, J. A., Halo, I., Chatterjee, A., Amol, P., Gupta, G. V. M., Singh, A., Mukherjee, A., Prakash, S., Beckley, L. E., Raes, E. J., and Hood, R.: Reviews and syntheses: Physical and biogeochemical processes associated with upwelling in the Indian Ocean, Biogeosciences, 18, 5967–6029, https://doi.org/10.5194/bg-18-5967-2021, 2021.

Wang, H., McClean, J. L., Talley, L. D., and Yeager, S.: Seasonal Cycle and Annual Reversal of the Somali Current in an Eddy-Resolving Global Ocean Model, J. Geophys. Res.-Oceans, 123, 6562–6580, https://doi.org/10.1029/2018JC013975, 2018.

Wang, Y., Zhang, F., Geng, Z., Zhang, Y., Zhu, J., and Dai, X.: Effects of Climate Variability on Two Commercial Tuna Species Abundance in the Indian Ocean, Fishes, 8, 99, https://doi.org/10.3390/fishes8020099, 2023.

Watts, L. and Owens, N.: Nitrogen assimilation and the f-ratio in the northwestern Indian Ocean during an in-

termonsoon period, Deep-Sea Res. Pt. II, 46, 725–743, https://doi.org/10.1016/S0967-0645(98)00125-8, 1999.

Watts, L., Sathyendranath, S., Caverhill, C., Maass, H., Platt, T., and Owens, N.: Modelling new production in the northwest Indian Ocean region, Mar. Ecol.-Prog. Ser., 183, 1–12, https://doi.org/10.3354/meps183001, 1999.

Weatherall, P., Marks, K. M., Jakobsson, M., Schmitt, T., Tani, S., Arndt, J. E., Rovere, M., Chayes, D., Ferrini, V., and Wigley, R.: A new digital bathymetric model of the world's oceans, Earth Space Sci., 2, 331–345, https://doi.org/10.1002/2015EA000107, 2015.

Webster, P. J., Moore, A. M., Loschnigg, J. P., and Leben, R. R.: Coupled ocean–atmosphere dynamics in the Indian Ocean during 1997–98, Nature, 401, 356–360, https://doi.org/10.1038/43848, 1999.

Westberry, T., Behrenfeld, M. J., Siegel, D. A., and Boss, E.: Carbon-based primary productivity modeling with vertically resolved photoacclimation, Global Biogeochem. Cyc., 22, 2007GB003078, https://doi.org/10.1029/2007GB003078, 2008.

Wiegner, T., Seitzinger, S., Glibert, P., and Bronk, D.: Bioavailability of dissolved organic nitrogen and carbon from nine rivers in the eastern United States, Aquat. Microb. Ecol., 43, 277–287, https://doi.org/10.3354/ame043277, 2006.

Wiggert, J. D., Vialard, J., and Behrenfeld, M. J.: Basin-Wide Modification of Dynamical and Biogeochemical Processes by the Positive Phase of the Indian Ocean Dipole During the SeaWiFS Era, in: Indian Ocean Biogeochemical Processes and Ecological Variability, Geophysical Monograph Series, AGU – American Geophysical Union, 385–407, ISBN 978-1-118-66636-4, https://doi.org/10.1029/2008GM000776, 2009.

Wirth, A., Willebrand, J., and Schott, F.: Variability of the Great Whirl from observations and models, Deep-Sea Res. Pt. II, 49, 1279–1295, https://doi.org/10.1016/S0967-0645(01)00165-5, 2002.

Wong, A. P. S., Wijffels, S. E., Riser, S. C., Pouliquen, S., Hosoda, S., Roemmich, D., Gilson, J., Johnson, G. C., Martini, K., Murphy, D. J., Scanderbeg, M., Bhaskar, T. V. S. U., Buck, J. J. H., Merceur, F., Carval, T., Maze, G., Cabanes, C., André, X., Poffa, N., Yashayaev, I., Barker, P. M., Guinehut, S., Belbéoch, M., Ignaszewski, M., Baringer, M. O., Schmid, C., Lyman, J. M., McTaggart, K. E., Purkey, S. G., Zilberman, N., Alkire, M. B., Swift, D., Owens, W. B., Jayne, S. R., Hersh, C., Robbins, P., West-Mack, D., Bahr, F., Yoshida, S., Sutton, P. J. H., Cancouët, R., Coatanoan, C., Dobbler, D., Juan, A. G., Gourrion, J., Kolodziejczyk, N., Bernard, V., Bourlès, B., Claustre, H., D'Ortenzio, F., Le Reste, S., Le Traon, P.-Y., Rannou, J.-P., Saout-Grit, C., Speich, S., Thierry, V., Verbrugge, N., Angel-Benavides, I. M., Klein, B., Notarstefano, G., Poulain, P.-M., Vélez-Belchí, P., Suga, T., Ando, K., Iwasaska, N., Kobayashi, T., Masuda, S., Oka, E., Sato, K., Nakamura, T., Sato, K., Takatsuki, Y., Yoshida, T., Cowley, R., Lovell, J. L., Oke, P. R., van Wijk, E. M., Carse, F., Donnelly, M., Gould, W. J., Gowers, K., King, B. A., Loch, S. G., Mowat, M., Turton, J., Rama Rao, E. P., Ravichandran, M., Freeland, H. J., Gaboury, I., Gilbert, D., Greenan, B. J. W., Ouellet, M., Ross, T., Tran, A., Dong, M., Liu, Z., Xu, J., Kang, K., Jo, H., et al.: Argo Data 1999–2019: Two Million Temperature-Salinity Profiles and Subsurface Velocity Observations From a Global Array of Profiling Floats, Front. Mar. Sci., 7, 700, https://doi.org/10.3389/fmars.2020.00700, 2020.

Yang, F., Resplandy, L., Zhao, Y., Liao, E., Ditkovsky, S., Malsang, M., Pearson, J., Ross, A. C., Hallberg, R., and Stock, C.: Model output for "A high-resolution physical-biogeochemical model for marine resource applications in the Northern Indian Ocean (MOM6-COBALT-IND12)", Zenodo [data set], https://doi.org/10.5281/ZENODO.14183131, 2024.

Yang, J., Yu, L., Koblinsky, C. J., and Adamec, D.: Dynamics of the seasonal variations in the Indian Ocean from TOPEX/POSEIDON sea surface height and an ocean model, Geophys. Res. Lett., 25, 1915–1918, https://doi.org/10.1029/98GL01401, 1998.

You, Y.: Seasonal variations of thermocline circulation and ventilation in the Indian Ocean, J. Geophys. Res.-Oceans, 102, 10391–10422, https://doi.org/10.1029/96JC03600, 1997.

You, Y. and Tomczak, M.: Thermocline circulation and ventilation in the Indian Ocean derived from water mass analysis, Deep-Sea Res. Pt. I, 40, 13–56, https://doi.org/10.1016/0967-0637(93)90052-5, 1993.

Zhou, J., Scherer, L., Van Bodegom, P. M., Beusen, A. H. W., and Mogollán,J. M.: A Comparison Between Global Nutrient Retention Models for Freshwater Systems, Front. Water, 4, 894604, https://doi.org/10.3389/frwa.2022.894604, 2022.

Zsoter, E.: River discharge historical data from the Global Flood Awareness System, CDS, https://doi.org/10.24381/CDS.A4FDD6B9, 2019.

Zuo, H., Balmaseda, M. A., Tietsche, S., Mogensen, K., and Mayer, M.: The ECMWF operational ensemble reanalysis–analysis system for ocean and sea ice: a description of the system and assessment, Ocean Sci., 15, 779–808, https://doi.org/10.5194/os-15-779-2019, 2019.

Zweng, M. M., Reagan, J. R., Antonov, J. I., Locarnini, R. A., Mishonov, A. V., Boyer, T. P., Garcia, H. E., Baranova, O. K., Johnson, D. R., Seidov, D., and Biddle, M.: World Ocean Atlas 2013, in: Volume 2: Salinity, Technical Edn., NOAA Atlas NESDIS 74, Tech. rep., edtied by: Levitus, S. and Mishonov, A., NOAA, 39 pp., https://doi.org/http://doi.org/10.7289/V5251G4D, 2014.